

Flow Boiling of Carbon Dioxide at Different Channel Orientations for the Thermal Management of Future Detector Technologies at the High-Luminosity Large Hadron Collider at CERN

Présentée le 23 juin 2022

Faculté des sciences et techniques de l'ingénieur
Laboratoire de conception mécanique appliquée
Programme doctoral en énergie

pour l'obtention du grade de Docteur ès Sciences

par

David SCHMID

Acceptée sur proposition du jury

Prof. D. Khovalyg, présidente du jury
Prof. J. A. Schiffmann, Prof. R. Revellin, directeurs de thèse
Prof. A. Cioncolini, rapporteur
Prof. A. Hafner, rapporteur
Prof. J. R. Thome, rapporteur

"Always look on the bright side of life."

– Eric IDLE

Abstract

The global warming potential (GWP) of working fluids in thermodynamic cycles and their environmental impact have been gaining considerable attention within the recent years. The global objectives on climate protection are becoming increasingly ambitious, whereas the general demand for refrigeration appliances with enhanced cooling capacities is constantly growing all over the world. One promising approach to reconcile these contradictory expectations is the replacement of synthetic working fluids with natural refrigerants.

The European Organization for Nuclear Research (CERN) supports the development of green technologies within the upgrades of their future accelerator facilities and Carbon Dioxide (CO₂) has been identified as an eco-friendly candidate with excellent heat transfer characteristics that has the potential for replacing detrimental refrigerants in future scientific and industrial cooling applications. Inspired by the positive experiences with several mid-scale refrigeration systems, the ATLAS and CMS experiments decided to use CO₂ as working fluid for the thermal management of their future Particle Tracker detectors requiring cooling capacities in the order of 0.5 MW.

Pressure drop and heat transfer properties are key factors for designing thermodynamic cycles properly. Motivated by the lack of experimental data of flow boiling CO₂ in vertical directions, a comprehensive research program has been launched to investigate the two-phase flow behaviour of CO₂, in particular in vertical up- and downward direction. As a first step, a test facility to study the two-phase flow characteristics has been built. The setup allows measurements of the significant two-phase flow parameters in horizontal, vertical up- and downward direction in macro-scale pipes with inner diameters of 8 mm. The test conditions of the experiments cover saturation temperatures from $-25\text{ }^{\circ}\text{C}$ to $+5\text{ }^{\circ}\text{C}$ and the mass velocity ranges from $100\text{ kg m}^{-2}\text{s}^{-1}$ to $450\text{ kg m}^{-2}\text{s}^{-1}$.

Flow pattern dependent prediction models are generally known to predict the flow boiling phenomena of two-phase flows with enhanced accuracy. Motivated by this aspect, transparent sections have been installed for flow visualization and 431 flow pattern observations of vertical upflow and 123 of vertical downflow have been recorded with a high-speed camera. The flow pattern records have been analyzed with a Frame- and Flow-Regime Classifier and new transition models have been developed for both vertical up- and downflow respectively. The novel transition criteria are finally presented with new flow pattern maps.

The performance of pressure drop models has been analyzed with data sets of 512 measurements in horizontal and 295 data points for each vertical up- and downflow direction respectively. 18 frictional pressure drop models have been compared to the horizontal data set and 21 void fraction correlations have been combined with the frictional pressure drop models accounting for the static head, resulting in 378 factorial combinations to anticipate the pressure losses in vertical directions. The best models have been identified for the entire data sets for all flow directions. Moreover, a subdivided analysis, split up according to the flow patterns, has been carried out to highlight the most accurate prediction methods with regard to the flow regimes.

The heat transfer properties of flow boiling CO₂ have been investigated in vertical upward direction with diabatic measurements of $\sim 5 \text{ kWm}^{-2}$ and $\sim 11 \text{ kWm}^{-2}$ respectively. The dryout phenomena at the inner tube perimeter are observed to be influenced by the heat flux, the mass velocity and the saturation temperature. To avoid operation at reduced heat transfer coefficients, a correlation to predict the dryout inception of the liquid film is suggested. The comparison of the data set to established prediction methods reveals, that the heat transfer coefficients of vertical upflow of two-phase CO₂ are generally underpredicted. As a consequence, an enhancement factor for vertical upflow of flow boiling CO₂ is suggested for two prediction models.

Key words: Carbon Dioxide (CO₂), Two-Phase Flow, Evaporative Detector Cooling, Pressure Drop, Flow Pattern, Heat Transfer, Flow Boiling.

Zusammenfassung

Das Treibhauspotenzial (GWP) von Arbeitsmedien in thermodynamischen Kreisprozessen und deren Einfluss auf die Umwelt haben in den letzten Jahren erheblich an Bedeutung gewonnen. Während die allgemeine Nachfrage nach Kühlgeräten mit stetig steigenden Kühlleistungen weltweit kontinuierlich wächst, werden die globalen Klimaschutzziele zunehmend ehrgeiziger definiert. Ein vielversprechender Ansatz, diese widersprüchlichen Erwartungen in Einklang zu bringen, ist die Ersetzung synthetischer Arbeitsmedien durch natürliche Kältemittel.

Die Europäische Organisation für Kernforschung (CERN) unterstützt die Entwicklung umweltfreundlicher Technologien im Rahmen der Modernisierung ihrer zukünftigen Beschleunigeranlagen und Kohlenstoffdioxid (CO_2) wurde als umweltfreundliche Alternative mit hervorragenden Wärmeübertragungseigenschaften identifiziert, die das Potenzial hat, schädliche Kältemittel in wissenschaftlichen und industriellen Kühlanwendungen zukünftigen zu ersetzen. Angeregt von den positiven Erfahrungen mit mehreren mittelgrossen Kälteanlagen haben die Experimente ATLAS und CMS beschlossen, CO_2 als Arbeitsmedium für den Wärmehaushalt ihrer zukünftigen Particle Tracker Detektoren zu verwenden, welche Kühlleistungen in der Größenordnung von 0,5 kW erfordern.

Druckabfall- und Wärmeübertragungseigenschaften sind Schlüsselfaktoren für die korrekte Auslegung thermodynamischer Kreisläufe. Aufgrund fehlender experimenteller Daten zum Strömungssieden von CO_2 in vertikalen Richtungen wurde ein umfassendes Forschungsprogramm zur Untersuchung des Zweiphasenströmungsverhaltens von CO_2 , insbesondere in vertikaler Auf- und Abwärtsrichtung, eingeleitet. Zunächst wurde eine Versuchsanlage zur Untersuchung der Zweiphasenströmungseigenschaften gebaut. Der Versuchsaufbau ermöglicht Messungen der wesentlichen Zweiphasenströmungsparameter in horizontaler, sowie vertikaler Auf- und Abwärtsrichtung in makroskopischen Rohren mit einem Innendurchmesser von 8 mm. Die Versuchsbedingungen umfassen Sättigungstemperaturen von -25 °C bis $+5\text{ °C}$ und Massenstromdichten von $100\text{ kg m}^{-2}\text{s}^{-1}$ bis $450\text{ kg m}^{-2}\text{s}^{-1}$.

Strömungsmusterabhängige Vorhersagemodelle sind allgemein bekannt, die Phänomene des Strömungssiedens von Zweiphasenströmungen mit erhöhter Genauigkeit vorherzusagen. Angeregt durch diesen Gesichtspunkt wurden transparente Teilstücke zur Veranschaulichung der Strömungsmuster eingebaut. 431 Beobachtungen von Strömungsmustern der vertikalen Aufwärtsströmung und 123 der vertikalen Abwärtsströmung wurden mit einer Hochgeschwin-

digkeitskamera aufgezeichnet. Die Aufzeichnungen der Strömungsmuster wurden mit einem Frame- und Flow-Regime Classifier analysiert und neue Übergangsmodelle für vertikale Auf- und Abwärtsströmungen erarbeitet. Die neuen Übergangskriterien werden schließlich mit neuen Karten für Strömungsmuster vorgestellt.

Die Eignung verschiedener Modelle zur Vorhersage des Druckabfalls von zweiphasigem CO_2 wurde mit Datensätzen von 512 Messungen horizontaler Strömung und je 295 Datenpunkten für vertikale Auf- und Abwärtsströmung analysiert. Der horizontale Datensatz wurde mit 18 Modellen zur Berechnung des Reibungsdruckverlustes verglichen. Zur Abschätzung des vertikalen Druckabfalls wurden 21 Korrelationen für den Dampfvolumenanteil – zur Berücksichtigung des statischen Drucks – mit den Reibungsverlustmodellen faktoriell kombiniert, was in 378 möglichen Kombinationen zur Berechnung des Druckabfalls in vertikale Richtungen resultiert. Für alle Strömungsrichtungen wurden die besten Berechnungsmodelle mit den gesamten Datensätzen ermittelt. Darüber hinaus wurde eine nach Strömungsmustern unterteilte Analyse durchgeführt, um die genauesten Vorhersagemethoden in Bezug auf die jeweiligen Strömungsmuster hervorzuheben.

Die Wärmeübertragungseigenschaften von strömungssiedendem CO_2 in vertikaler Aufwärtsrichtung wurden mit diabatischen Messungen bei Wärmestromdichten von $\sim 5 \text{ kW m}^{-2}$ und $\sim 11 \text{ kW m}^{-2}$ untersucht. Es wird festgestellt, dass die Austrocknungserscheinungen am inneren Rohrumfang durch die Wärmestromdichte, die Massenstromdichte und die Sättigungstemperatur beeinflusst werden. Um Betriebsszenarien mit reduzierten Wärmeübergangskoeffizienten zu vermeiden, wird eine Korrelation zur Vorhersage des Austrocknungsbeginns des Flüssigkeitsfilms vorgetragen. Der Vergleich des Datensatzes mit etablierten Berechnungsmethoden zeigt, dass die Wärmeübertragungskoeffizienten vertikaler Aufwärtsströmungen von zweiphasigem CO_2 im Allgemeinen zu gering eingeschätzt werden. Infolgedessen werden Korrekturfaktoren für zwei Modelle zur Berechnung der Wärmeübertragungskoeffizienten vertikaler Aufwärtsströmung von strömungssiedendem CO_2 vorgeschlagen.

Stichwörter: Kohlenstoffdioxid (CO_2), Zweiphasenströmung, Verdampfungskühlung für Detektoren, Druckabfall, Strömungsmuster, Wärmeübertragung, Strömungssieden.

Résumé

Le potentiel de réchauffement global (PRG) des fluides de travail utilisés dans des cycles thermodynamiques, ainsi que leurs impacts sur l'environnement, est récemment devenu un sujet de grande attention. Les objectifs environnementaux deviennent de plus en plus ambitieux alors que la demande en froid ne fait qu'augmenter dans le monde entier. Une approche permettrait de répondre à ces deux objectifs pourtant contradictoires : développer l'utilisation de frigorigènes naturels.

Le Conseil Européen pour la Recherche Nucléaire (CERN) encourage fortement le développement de technologies écologiques pour les modifications de leurs installations scientifiques actuelles. Le dioxyde de carbone (CO_2) possédant d'excellentes caractéristiques de transfert de chaleur, a été identifié comme un fluide alternatif permettant de remplacer les frigorigènes néfastes pour l'environnement dans les applications industrielles. Inspiré du succès de plusieurs systèmes de réfrigération de taille moyenne, les expériences ATLAS et CMS ont décidé d'appliquer elles aussi le CO_2 comme fluide de travail pour la gestion thermique de leurs futurs détecteurs de particules, exigeant des capacités réfrigérantes de l'ordre de 0,5 MW.

Les chutes de pression et les propriétés de transfert thermiques sont des facteurs clés pour concevoir des cycles thermodynamiques adéquats. Motivé par le manque de données expérimentales concernant les écoulements de CO_2 en ébullition convective dans un canal vertical, un programme de recherche a été lancé pour étudier le comportement des écoulements diphasiques de CO_2 , en particulier les écoulements verticaux ascendant et descendant. Un banc d'essai a été mis en place et a permis de mesurer les paramètres essentiels de l'écoulement horizontal et vertical ascendant et descendant dans des tuyaux de diamètre interne de 8 mm. Les conditions d'essais des expériences couvrent des températures de -25°C à $+5^\circ\text{C}$ et des débits de $100\text{ kg m}^{-2}\text{s}^{-1}$ à $450\text{ kg m}^{-2}\text{s}^{-1}$.

Les modèles de prédiction basés sur les régimes d'écoulement sont réputés pour leur précision. Dans cette optique, des sections transparentes ont été installées pour visualiser l'écoulement et 431 observations en écoulement vertical ascendant et 123 en vertical descendant ont été enregistrées avec une caméra à haute vitesse. Ces enregistrements ont par la suite été analysés avec un classificateur de régime et de nouveaux modèles de transition ont été développés pour les écoulements verticaux ascendants et descendants. Ces nouveaux critères de transition sont finalement représentés dans de nouvelles cartes d'écoulement.

La qualité de prédiction des modèles de chutes de pression a été analysée grâce à 512 mesures dans le sens horizontal et 295 dans le sens vertical (ascendant et descendant). 18 modèles de chutes de pression par frottement ont été comparés à l'ensemble des données horizontales. De plus, 21 corrélations de taux de vide ont été combinées avec les modèles de chute de pression par frottement en tenant compte de la hauteur statique, ce qui a produit 378 combinaisons permettant de calculer les chutes de pression dans les directions verticales. Les meilleurs modèles ont été identifiés pour les différentes configurations d'écoulement. De plus, une analyse menée en fonction du régime d'écoulement a été effectuée pour mettre en valeur les méthodes de prédiction les plus précises pour chaque régime.

Les caractéristiques de transfert de chaleur d'un écoulement vertical ascendant de CO₂ en ébullition ont été étudiées grâce à des mesures effectuées avec apport de chaleur ($\sim 5 \text{ kW m}^{-2}$ et $\sim 11 \text{ kW m}^{-2}$). Le phénomène d'assèchement est influencé par la densité de flux de chaleur, la vitesse massique et la température de saturation. Une corrélation permettant de prédire le début de l'assèchement a également été proposée. La comparaison de l'ensemble des données avec les méthodes de prédiction disponibles dans la littérature démontre que les coefficients de transfert de chaleur en écoulement vertical ascendant sont en général sous-estimés. Par conséquent, un facteur d'accroissement pour l'écoulement vertical ascendant de CO₂ diphasique est suggéré pour deux modèles de prédiction.

Mots clefs : Dioxide de Carbon (CO₂), écoulement diphasique, refroidissement évaporatif de détecteurs, perte de pression, régime d'écoulements, transfert de chaleur, ébullition.

Acknowledgements

You'll never walk alone...

... a song initially coming from the Broadway, performed and interpreted by various artists and well-known in many arenas and stadiums. Even though I knew the song from an early age and having heard it many times, the last $4\frac{1}{2}$ years brought me even closer to the meaning of these words. The present work is by far not the result of a single character. It is the embodiment of an adventure that has been accompanied by many people, contributing in many different ways.

First and foremost, my warmest gratitude goes to my Professors Jürg and Rémi and to my CERN supervisors Bart and Paolo for accompanying me the entire way with their genius support and giving me the possibility to work freely in an unconstrained environment. I feel privileged having had the chance to take advantage of their vast knowledge and expertise. And all of this in a very pleasant and motivating atmosphere.

Furthermore, I want to express my heartfelt thanks to all the other companions throughout this journey, in particular to:

Wojciech and Loïc for setting up the controls of the test facility and supporting me literally 24/7;

Shai, Jarryd and Edward for offering their expertise with regard to machine learning based computer vision techniques and developing a Frame- and Flow-Regime-Classifer;

Natalia, Bartłomiej and Piotr for their CAD support and help in designing the test rig;

Jérôme, Cédric, Hervé, Abdel, Patrick and Franck for their help in the lab and the workshop;

My fellow CERN-PhD "sufferers" Desirée, Viren, Lorenzo and Tiago for their advice and sharing the frustration when getting "stuck in the mud";

Isabelle, Noémie, Daniella, Stuart and Shuvay for their linguistic competences and support;

My colleagues Dina, João, Lukasz, Hans, Michal, Tym, Maciej, Krzysztof, Jérôme and Paola for their advice and the enriching discussions;

All the colleagues from EPFL/LAMD for the support and offering me help when using the laboratory's infrastructure;

Cécile, Veronique and Eszter for the administrative support;

The student crowd for the entertainment and the occasional parties;

My friends and football mates for the occasional distraction from work;

Christoph, Giancarlo and Hansdieter for opening new doors and paving the way for this opportunity;

The ATLAS experiment for sponsoring and making this journey possible;

My sisters and my family for the support and giving me a carefree life. And in particular to my parents for bringing me into existence;

And finally to Aleksandra, for the constant support, her patience and comprehension in sacrificing a lot – vacations, weekend plans and much more – throughout this episode.

My heartfelt thanks to all of you; because of you, I never walked alone.

At the end, I want to address some words to all my fellow research students that are currently "walking in a storm": Have faith in your skills, stay motivated and keep on working hard! Then always remember:

"... at the end of a storm, there's a golden sky!"

Istein, 2022

David

Contents

Abstract (English/Deutsch/Français)	ii
Acknowledgements	vii
List of Figures	xiii
List of Tables	xix
List of Publications	xxi
1 Introduction	1
1.1 The European Organization for Nuclear Research (CERN)	1
1.2 Particle Detectors in High Energy Physics	1
1.3 Silicon Tracker Detectors	3
1.4 High-Luminosity Phase-II Upgrades and Requirements for new Tracker Detectors	5
1.5 Nature of the Issue / Problem Statement	7
1.6 Goal and Objectives	8
1.7 Methodology and Thesis Outline	9
2 The Test Facility	11
2.1 General Description of the Test Facility	11
2.1.1 Refrigeration Unit CORA	11
2.1.2 The experimental Test Rig	12
2.2 Experimental Conditions and Test Matrix	15
2.3 Data Acquisition	17
2.4 Validation of the Test Facility	18
2.4.1 Single-phase Pressure Drop	18
2.4.2 Single-phase Energy Balance	19
2.5 Data Collection and Data Reduction	23
2.5.1 Steady-state Conditions	23
2.5.2 Derived Properties	23
2.5.3 Data Clustering	24
2.5.4 Statistical Evaluation	25
2.5.5 Numerical Calculation	25
2.6 Uncertainties of Measurements and Properties	25
	ix

3	Flow Pattern	27
3.1	Literature Review	27
3.1.1	Flow pattern maps for vertical two-phase flow in macroscale tubes . . .	27
3.1.2	Flow pattern observations and maps for horizontal two-phase flow of CO ₂	28
3.1.3	Nature of the issue and objective of the present chapter	29
3.2	Experimental Methodology and Database	30
3.2.1	Transparent sections and visualization techniques	30
3.2.2	The Database	30
3.3	Flow Pattern Observations and Transitions	32
3.4	Flow Pattern Detection Methods	36
3.5	Flow Pattern Observations compared to existing Transition Lines	37
3.6	Development of a new Flow Pattern Map for vertical two-phase Flow of CO ₂ . .	39
3.7	Conclusion	45
4	Pressure Drop	49
4.1	Literature Review	50
4.1.1	Frictional pressure drop models	50
4.1.2	Void fraction correlations	51
4.1.3	Nature of the issue and objective of the present chapter	52
4.2	The Test Sections and the Database	53
4.3	Pressure Drop Phenomena and Flow Regimes	53
4.4	Pressure Drop Measurements and Influences of Flow Parameters	55
4.5	Pressure Drop Measurements compared to Prediction Models	58
4.5.1	Comparison of horizontal data	60
4.5.2	Comparison of vertical upflow data	62
4.5.3	Comparison of vertical downflow data	66
4.6	Conclusion	70
5	Heat Transfer	73
5.1	Literature Review	73
5.1.1	General heat transfer prediction methods for flow boiling of refrigerants	73
5.1.2	Flow boiling heat transfer of CO ₂	74
5.1.3	Nature of the issue and objective of the present chapter	75
5.2	The Test Sections and the Database	76
5.3	Experimental Results and Influences of Flow Parameters	79
5.4	Prediction of the Critical Vapour Quality	83
5.5	Comparison of the experimental Heat Transfer Data to Prediction Models . . .	84
5.6	Conclusion	89
6	Epilogue	91
6.1	Summary and Conclusion	91
6.2	Outlook and Prospects	93

A: Accuracy and Uncertainties	97
A.1 Error Propagation	97
A.2 Uncertainties of Instrumentation and Measurements	98
A.2.1 Temperature	98
A.2.2 Pressure	101
A.2.3 Mass flow rate	102
A.2.4 Diameter and wall thickness	102
A.2.5 Length of test sections and evaporator	102
A.3 Uncertainties of derived Quantities	103
A.3.1 Mass velocity	103
A.3.2 Enthalpy in single-phase	103
A.3.3 Enthalpy in two-phase before the evaporator	104
A.3.4 Enthalpy in two-phase inside or after the evaporator	105
A.3.5 Vapour quality	105
A.3.6 Heat flux	106
A.3.7 Heat transfer coefficient	106
List of Acronyms	109
List of Symbols	111
Bibliography	115
Curriculum Vitae	129

List of Figures

1.1	The Large Hadron Collider [3].	2
1.2	Accelerator facility and experiments at CERN [4].	3
1.3	The ATLAS experiment [6] installed in the underground facilities of the Large Hadron Collider at ~ 100 m below surface.	4
1.4	Detector components of the Particle Trackers of the ATLAS and CMS experiments: The ATLAS pixel detector [9] (left) and the first half of the CMS inner tracker barrel [10].	4
1.5	Characteristics of CO ₂ . Left: Change of saturation temperature due to pressure changes of 1 bar. The saturation temperature of CO ₂ is less affected than other refrigerants. Right: Global Warming Potential of several refrigerants in comparison to CO ₂ (GWP _{CO2} = 1).	6
1.6	Schematical illustration of the flow distribution between the cooling plants in the service caverns and the detectors facilities inside the experimental caverns.	7
2.1	Refrigeration unit CORA portrayed from different perspectives.	12
2.2	Piping and instrumentation diagram (P&ID) of the test facility.	13
2.3	Arrangement of instrumentation at the pressure taps.	14
2.4	Experimental test rig, portrayed at different sections. a): pre- and post-heater unit with bypass at the in- and outlet of the test rig and the connection to the refrigeration plant; b) horizontal test section (left pipe) and return line (right pipe); c) bottom view of vertical up- and downflow test sections; d) top view of vertical test sections.	15
2.5	Experimental domain and range of stable test conditions of the test facility (illustrated with colours). The test matrix of the data collection is marked by the hatching and the numbers indicate the max. vapour qualities that can be reached in adiabatic conditions.	17
2.6	SCADA control panel of the CORA refrigeration unit (left) and the test rig (right).	17
2.7	Left: Experimental pressure drop measurements recorded by the differential pressure transmitters at the horizontal, the vertical up- and downward test sections compared to the analytical values according to Blasius [35] and Colebrook-White [36]. The dashed lines indicate an error band of ± 10 %. The deviations between the experimental and the analytical values are shown on the right hand side.	18

2.8	Left: Temperature profiles of the single-phase flow, the saturation temperature and the ambient conditions over the entire setup during a single-phase run at $G = 300 \text{ kg m}^{-2} \text{ s}^{-1}$; right: Simplified model of the tube insulation.	21
2.9	Single-phase energy balances of the pre- and post-heater.	21
2.10	Single-phase energy balance of the evaporator.	22
2.11	Experimental Nusselt number of the most accurate (probe TT2A42, left) and the worst (probe TT2A48, right) measurements determined with calibration runs compared to the convective heat transfer models of Dittus-Boelter [39] and Gnielinski [40].	22
3.1	Transparent section for flow visualization; sectional view (left) and during operation (right).	31
3.2	Histograms describing the experimental database.	31
3.3	Typical two-phase flow patterns in vertical upward direction ($\vartheta = +90^\circ$).	32
3.4	Flow pattern observations of CO_2 in vertical upward direction ($\vartheta = +90^\circ$) at $T_{sat} = -25^\circ \text{C}$; $G = 200 \text{ kg m}^{-2} \text{ s}^{-1}$; vapour quality increasing from top left to bottom right: bubbly, bubbly, slug, slug, churn, annular, annular, vapour/mist. The red lines represent the inner tube walls.	34
3.5	Flow pattern observations of CO_2 in vertical downward direction ($\vartheta = -90^\circ$) at $T_{sat} = -25^\circ \text{C}$; $G = 200 \text{ kg m}^{-2} \text{ s}^{-1}$; vapour quality increasing from top left to bottom right: bubbly, slug, slug, churn, churn, annular, annular, vapour/mist. The red lines represent the inner tube walls.	35
3.6	Flow regime observations of CO_2 two-phase flow in vertical upward direction (markers) compared to the flow pattern map of Barnea [51] (lines). Curve B represents the transition from bubbly to slug, curve H the transition from slug to churn and curve J the transition from churn to annular flow. Line G gives the transition to dispersed bubble flow. The transition lines were plotted based on the experimental conditions of the experiments.	37
3.7	CO_2 flow pattern observations at $T_{sat} = +5^\circ \text{C}$ compared to transition lines of Taitel et al. [50], Weisman & Kang [86], McQuillan & Whalley [56], Mukherjee & Brill [87] and Chen & Brill [89]. The coordinates represent the superficial liquid (j_L) and vapour (j_V) velocities.	38
3.8	Identified flow pattern map for vertical upflow of CO_2 in comparison to the test data. The transition zones are determined with data regressions through the first and last data points of the flow regimes.	43
3.9	Identified flow pattern map for vertical downflow of CO_2 in comparison to the test data. The transition zones are determined with data regressions through the first and last data points of the flow regimes.	44
3.10	Detailed view of the bubbly-to-slug flow regime transition in both upward ($\vartheta = +90^\circ$) and downward ($\vartheta = -90^\circ$) direction: transition lines with temperature dependent transition zones.	45

3.11	Influence of mass velocity illustrated with observations of bubbly flow (top row) and slug flow (bottom row) of CO ₂ in vertical upward direction ($\vartheta = +90^\circ$) at $T_{sat} = +5^\circ\text{C}$. Mass velocity increases from left to right, while vapour quality stays (almost) constant. Finely dispersed bubbles that move upward on a vertical trajectory can be observed at low flow rates. At increased mass velocities, the flow gets turbulent and an increasing coalescence of the bubbles can be noticed.	46
3.12	Influence of mass velocity illustrated with observations of CO ₂ in vertical downward direction ($\vartheta = -90^\circ$) at $T_{sat} = -15^\circ\text{C}$. Mass velocity increases from left to right, while vapour quality stays (almost) constant. Bubbly flow (top row) immediately turns into churn flow at low mass velocities (bottom left), whereas bubbly flow converts to slug flow at increased flow rates (bottom right).	47
3.13	Flow pattern maps for vertical upward (top left) and downward (top right) direction of CO ₂ elaborated within this study in combination with the horizontal flow pattern map of Cheng et al. [72] (bottom). The novel transition zones in the vertical up- and downflow maps are applicable for saturation temperatures $-25^\circ\text{C} \leq T_{sat} \leq +5^\circ\text{C}$. B: bubbly, S: slug, C: churn, A: annular, D: dryout, St: stratified, StW: stratified-wavy.	48
4.1	Histograms describing the experimental pressure drop database in terms of mass velocity and saturation temperature.	53
4.2	Flow regimes of the pressure drop database recorded within this study. Left: Direct flow pattern observations (illustrated with dark blue and dark red bars) and flow regimes deduced from the flow pattern maps of Schmid et al. [134] (illustrated with light blue and light red bars) in vertical direction. Right: Flow patterns of horizontal data deduced from the flow pattern map of Cheng et al. [72].	54
4.3	Standard deviation ($6\sigma_{STD}$) of pressure drop oscillations in CO ₂ two-phase flow in a stainless steel tube with an inner diameter of 8 mm measured in various flow directions. The plots show the entire data sets available in the present study at various mass velocities and saturation temperatures.	55
4.4	Pressure drops of CO ₂ two-phase flow measured at the horizontal test section ($\vartheta = 0^\circ$, $l = 8\text{ m}$, $d = 8\text{ mm}$) under varying flow parameters, grouped according to the mass velocity (top) and saturation temperature (bottom).	56
4.5	Two-phase pressure drop measurements of CO ₂ in vertical upward direction ($\vartheta = +90^\circ$, $l = 8\text{ m}$, $d = 8\text{ mm}$) under varying flow parameters, grouped according to the mass velocity (top) and saturation temperature (bottom).	57
4.6	Two-phase pressure drop measurements of CO ₂ in vertical downward direction ($\vartheta = -90^\circ$, $l = 8\text{ m}$, $d = 8\text{ mm}$) under varying flow parameters, grouped according to the mass velocity (top) and saturation temperature (bottom).	57
4.7	Entire experimental data set in horizontal direction is best predicted by the frictional pressure drop model of Müller-Steinhagen & Heck [98].	60
4.8	Best performing frictional pressure drop models compared to experimental data in horizontal direction ($\vartheta = 0^\circ$) grouped according to the flow regimes.	61

- 4.9 Graphical representation of the statistical comparison (MAPE [%] and ξ_{20} [%]) between the compiled experimental data set (295 measurements) for CO₂ two-phase flow in vertical upward direction ($\vartheta = +90^\circ$) and the predicted pressure drops according the 378 possible combinations considered. The frictional pressure drop models are depicted on the abscissae in arabic numbers as listed in Table 4.1, the ordinates represent the void fraction correlations with roman numbers according to Table 4.2. 63
- 4.10 Entire experimental data set in vertical upward direction ($\vartheta = +90^\circ$) compared to the best performing pressure drop models. Left: The combination of the frictional model of Müller-Steinhagen & Heck [98] and the void fraction correlation of Baroczy [116]; Middle: The Friedel [97] model combined with the void fraction correlation of Premoli et al. [124]; Right: The model of Sun & Mishima [101] in combination with the void fraction correlation of Baroczy [116]. 63
- 4.11 Experimental data in vertical upward direction analyzed in regard of the flow regimes. Top left: all data points compared to the homogeneous two-phase viscosity model of Awad & Muzychka II [143] and the void fraction correlation of Baroczy [116]. The pressure drop data grouped according the flow regimes is best predicted by the frictional pressure drop models and the void fraction correlations of: top middle: Jung & Radermacher [99] and the homogeneous void fraction model for bubbly flow; top right: Friedel [97] and Woldesemayat & Ghajar [123] for slug flow; bottom left: homogeneous two-phase viscosity model of Owens [138] and Rouhani & Axelsson [125] for churn flow; bottom middle: Müller-Steinhagen & Heck [98] and Baroczy [116] for annular flow; bottom right: Sun & Mishima [101] and Bhagwat & Ghajar [132] for mist/vapour flow. The statistical comparison is given in Table 4.5. 65
- 4.12 Measured and predicted pressure drops in upward direction ($\vartheta = +90^\circ$) according the frictional model of Müller-Steinhagen & Heck [98] and the static head with the void fraction correlation of Baroczy [116]. The total pressure drop results from the superposition of the static head (red), the frictional (green) and the accelerational component (cyan). 65
- 4.13 Graphical representation of the statistical comparison (MAPE [%] and ξ_{20} [%]) between the compiled experimental data set (295 measurements) in vertical downward direction ($\vartheta = -90^\circ$) and the predicted pressure drops according the 378 possible combinations considered. The frictional pressure drop models are depicted on the abscissa in arabic numbers as listed in Table 4.1, the ordinate represents the void fraction correlations with roman numbers according to Table 4.2. 66
- 4.14 Experimental data in vertical downward direction ($\vartheta = -90^\circ$) compared to the calculated pressure drops according to the combinations of Friedel [97] and the homogeneous void fraction correlation (left), Lombardi & Carsana [148] and Cioncolini & Thome [128] (middle) and Lombardi & Carsana [148] and Woldesemayat & Ghajar [123] (right). 67

4.15	Experimental data in vertical downward direction ($\vartheta = -90^\circ$) analyzed in regard of the flow regimes. Top left: all data points for slug flow compared to the frictional pressure drop model of Lombardi & Carsana [148] and the void fraction correlation of Lockhart & Martinelli [96]; top right: the model of Lombardi & Carsana [148] and the void fraction correlation of Yashar et al. [149] for churn flow; bottom left: the model of Müller-Steinhagen & Heck [98] and the homogeneous void fraction correlation for annular flow; bottom right: the model of Grønnerud [106] and the void fraction correlation of Turner & Wallis [117] for mist flow.	68
4.16	Measured and predicted pressure drops in the vertical downward channel ($\vartheta = -90^\circ$) at $T_{sat} = -25^\circ\text{C}$, $G = 200\text{ kg m}^{-2}\text{ s}^{-1}$. The total pressure drop results from the superposition of the static head (red), the frictional (green) and the accelerational components (cyan). Left: Frictional pressure drop model of Lombardi & Carsana [148] and void fraction correlation of Cioncolini & Thome [128]; middle: Frictional pressure drop model of Friedel [97] and the homogeneous void fraction model; right: Frictional pressure drop model of Lombardi & Carsana [148] and void fraction correlation of Woldeesemayat & Ghajar [123].	69
5.1	Cross-sectional view of the test section.	77
5.2	Histograms describing the experimental heat transfer database for vertical up-flow with regard to mass velocity, saturation temperature, heat flux and flow regimes.	78
5.3	Experimental heat transfer coefficients grouped according to saturation temperature and mass velocity, measured at a heat flux of $q = 5.3\text{ kW m}^{-2}$. The errorbars indicate the uncertainties of the heat transfer measurements.	79
5.4	Experimental heat transfer coefficients grouped according to saturation temperature and mass velocity, measured at a heat flux of $q = 11.4\text{ kW m}^{-2}$. The errorbars indicate the uncertainties of the heat transfer measurements.	80
5.5	Reduced data sets of experimental heat transfer coefficients versus vapour quality grouped according to the saturation temperature and the heat flux. Increasing saturation temperature from left to right, increasing heat flux from top to bottom.	81
5.6	Reduced data sets of experimental heat transfer coefficients versus vapour quality grouped according to the mass velocity and the heat flux. Increasing mass velocity from left to right, increasing heat flux from top to bottom.	82
5.7	Conditions where dryout is encountered within the present data set.	83
5.8	Comparison of the reduced data set, excluding the dryout data, to several heat transfer models.	86
5.9	Comparison of the reduced data set, excluding the dryout data, to several heat transfer models developed with databases including horizontal data of CO_2	87
5.10	Comparison of the reduced data set, excluding the dryout data, to the prediction models corrected by the enhancement factor for vertical upflow.	88

1	T-probe calibration with a temperature-controlled bath (left). The T-probes are placed inside a copper block next to the reference sensor (right).	99
2	Pre- and post-calibration measurements.	100
3	Statistical evaluation of temperature measurements before (left) and after calibration (right). Illustration based on measurements of T-probe TT2A60.	100
4	Calibration of pressure transmitters with a deadweight tester.	102
5	Sanity check to validate the thermal bulk resistance of the insulation used in Eq. 2.8 for determining the heat pickup from ambient.	104

List of Tables

2.1	Comparison of single-phase pressure drops.	19
2.2	Variation by means of the standard deviation (STD) of the flow parameters throughout the entire data set.	24
2.3	Uncertainties of the calibrated instrumentation and the property calculations.	25
3.1	Camera settings for the recording of the high-speed images	30
3.2	Range of non-dimensional numbers of the test campaign	40
3.3	Statistics of the identified transition equations	42
4.1	Frictional pressure drop correlations appropriate for macrochannels considered within this study.	58
4.2	Void Fraction correlations used in this study.	59
4.3	Statistical comparison between frictional pressure drop models and the entire experimental database, as well as flow patten specific comparison, in horizontal direction.	61
4.4	Statistical comparison of the horizontal measurements to the frictional two-phase viscosity models using the vapour-quality-based (Eq. 4.4) and the void-fraction-based (Eq. 4.5) two-phase densities.	62
4.5	Statistical comparison of the 295 experimental data points in vertical upward direction ($\vartheta = +90^\circ$) and the best performing aggregate pressure drop models as a combination of the frictional and the static component.	64
4.6	Statistical comparison of the 295 experimental data points in vertical downward direction ($\vartheta = -90^\circ$) and the best performing aggregate pressure drop models as a combination of the frictional and the static component.	67
5.1	Statistical comparison of the entire and the reduced experimental data set to the predicted heat transfer coefficients in chronological order.	85
5.2	Statistical comparison split up according to the flow patterns in chronological order.	85
1	Specifications of the absolute pressure transmitters installed in the test facility.	101
2	Specifications of the differential pressure transmitters installed at the test sections.	101
3	Single-phase enthalpies according to the uncertainties of the pressure and temperature measurements at 5.2 °C and 40 bar.	103

4	Uncertainties of the heat transfer coefficient [%].	107
---	---	-----

List of Publications

The following manuscripts have been submitted for publishing and are either accepted or currently under review. The content and results of the publications I participated as first author are presented verbatim and/or in substance within the present work.

Journal articles as first author

- D. Schmid, B. Verlaat, P. Petagna, R. Revellin and J. Schiffmann. "Flow pattern observations and flow pattern map for adiabatic two-phase flow of carbon dioxide in vertical upward and downward direction", *Experimental Thermal and Fluid Science*, 2022.
doi.org/10.1016/j.expthermflusci.2021.110526
- D. Schmid, B. Verlaat, P. Petagna, J. Schiffmann and R. Revellin. "Adiabatic two-phase pressure drop of carbon dioxide in different channel orientations", *International Journal of Heat and Fluid Flow*, 2022.
doi.org/10.1016/j.ijheatfluidflow.2022.108966
- D. Schmid, B. Verlaat, P. Petagna, R. Revellin and J. Schiffmann. "Heat transfer of flow boiling carbon dioxide in vertical upward direction", *International Journal of Heat and Mass Transfer*, under review, submitted: Dec 09, 2021.

Journal articles as co-author

- S. Kadish, D. Schmid, J. Son and E. Boje. "Computer Vision based classification of flow regimes and vapor quality in vertical two-phase flow", *Sensors*, 2022.
doi.org/10.3390/s22030996
- P. Tropea, J. Daguin, D. Giakoumi, N. Koss, P. Petagna, H. Postema, D. Schmid, B. Verlaat and L. Zwalinski. "Advancements and plans for the LHC upgrade detector thermal management with CO₂ evaporative cooling", *Nuclear Instruments and Methods in Physics Research Section A: Accelerators, Spectrometers, Detectors and Associated Equipment*, 2019.
doi.org/10.1016/j.nima.2018.10.083

1 Introduction

1.1 The European Organization for Nuclear Research (CERN)

The idea of a European research facility was brought up by some visionary scientists at the end of the 1940s when the prospects for cutting-edge research in Europe were poor and many institutions were in bad conditions. In 1954 this vision became true and the convention for the European Organization for Nuclear Research (CERN) was established by 12 founder states^I. Nowadays, CERN is the largest laboratory of its kind and the collaboration with hundreds of institutes and renowned universities from all over the world forms a truly unique excellence cluster. The initial studies at the laboratory were focused on the atomic nucleus, then continuously shifted to High Energy Physics (HEP) and probing the fundamental questions of our universe with particle interactions.

The Large Hadron Collider (LHC) at CERN is currently the largest and most powerful particle accelerator in the world. Installed in a circular tunnel of ~ 27 km circumference at a depth of 50 - 175 m below surface, the LHC accelerates particles close to the speed of light and provides proton-proton collisions at a centre-of-mass energy of 14 TeV [1],[2]. The two particle beams travel inside the beam pipes in a ultrahigh vacuum that is comparable to the atmosphere in outer space and magnetic fields, maintained by superconducting magnets, guide the beams on circular trajectories in opposite direction through the machine. Figure 1.1 shows a section of the LHC in the underground facility of CERN.

1.2 Particle Detectors in High Energy Physics

Today, CERN hosts the most complex accelerator facility in the world and provides a unique infrastructure for fundamental research and various physics experiments. The LHC provides particle collisions at four interaction points that are recorded by complex instrumentation, the particle detectors ALICE, ATLAS, CMS and LHCb. However, besides the four aforementioned LHC detectors, CERN comprises a variety of experiments that are embedded in its infras-

^IIn 2021, CERN comprises 23 member states.

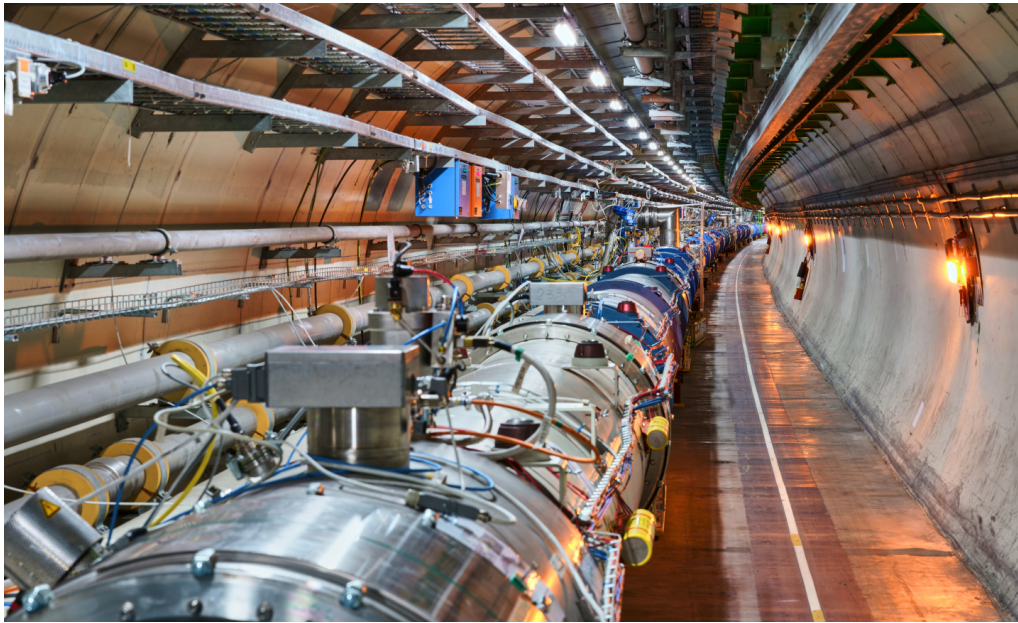


Figure 1.1 – The Large Hadron Collider [3].

structure. Figure 1.2 provides an overview of the entire accelerator facility and the adjacent experiments.

The two biggest LHC experiments, ATLAS and CMS, are both general-purpose detectors designed for studying the fundamental nature of matter and the basic forces that shape our universe. The capabilities of both detectors are comparable and the differences are more of technical nature. Both consist of the same subsystems, that are:

- the **Inner Detector**, also called **Particle Tracker**, to measure the trajectories, momenta and charges of particles;
- the **Electromagnetic and Hadronic Calorimeters**, to measure the energies of the particles;
- the **Magnet System**, to bend the particle tracks such that momentum and charge can be derived from the curved trajectories and
- the **Muon Spectrometer**, to measure the tracks and momenta of muons, whose trajectories are moderately affected and bent by the magnetic field, thus requiring larger distances for precise measurements.

The subsystems of the cylindrical-shaped ATLAS and CMS detectors are arranged in different layers around the interaction points, where particle are made to collide. Figure 1.3 illustrates a cross-sectional view of the ATLAS detector, that has a length of 46 m, a diameter of 25 m and a mass of 7000 t. Besides being physically the largest particle physics detector in terms of volumetric size, the ATLAS experiment – with its 181 institutes participating from all over the world – also forms the largest collaborative endeavor ever attempted in science [5].

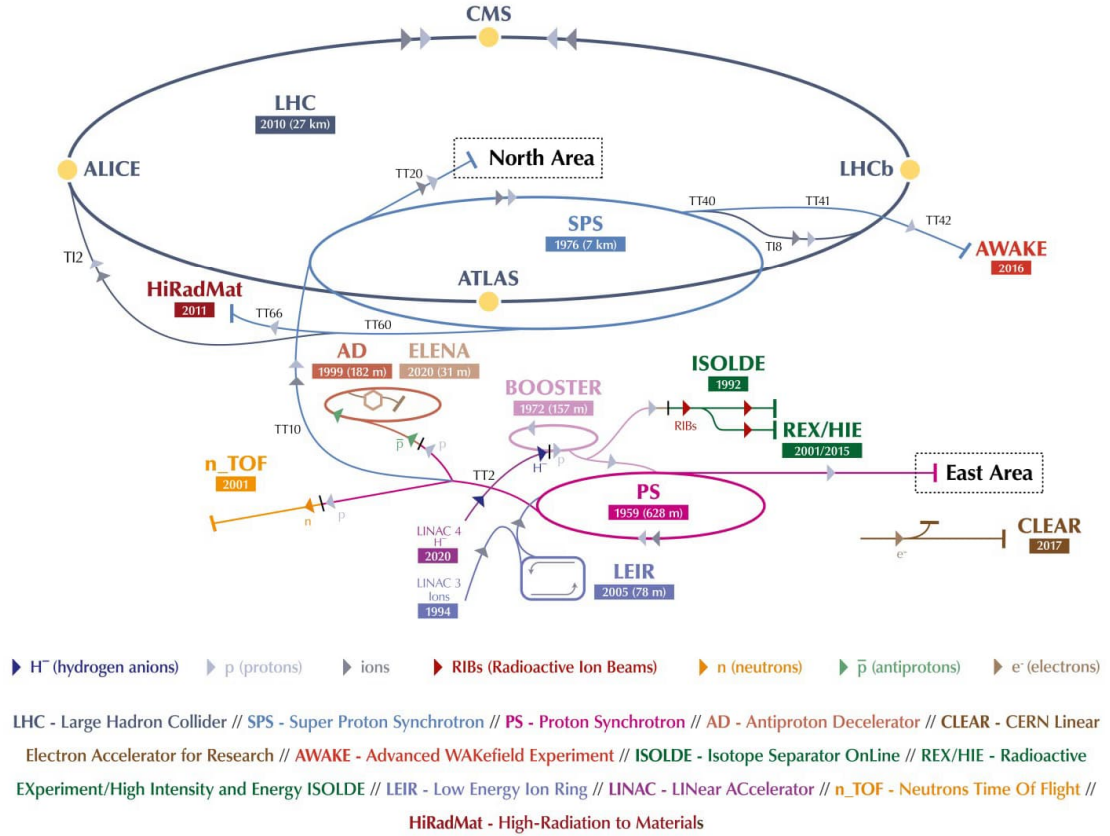


Figure 1.2 – Accelerator facility and experiments at CERN [4].

1.3 Silicon Tracker Detectors

The Particle Tracker is the innermost detector sequence directly located around the interaction point to measure the direction, momentum and charge of the collisions' decay products. The cylindrical-shaped detector consists of several layers of semiconductor instrumentation that allow the spatial reconstruction of the particle trajectories with an extremely high precision. A Tracker detector itself consists of several subsystems that are organized as coaxial cylinders around the beam pipe, named "barrels", and disk-shaped "end-caps" arranged perpendicularly to the beam. Both barrel and end-cap layers consist of silicon detector modules that are mounted on lightweight and stiff support structures forming an enclosed surface around the interaction point to capture the particle tracks in all directions. This gives an extremely compact and dense multi-shell volume [7]. Figure 1.4 portrays details of the current Particle Trackers installed in the ATLAS and CMS experiments.

Particle Trackers are typically composed of different semiconductor detector technologies. Strip modules consist of elongated semiconductor arrays that are arranged alongside each other. Particles penetrating the strips trigger electrical charges that are recorded by the read-out electronics at the periphery of the modules. A perpendicular arrangement of Strip modules

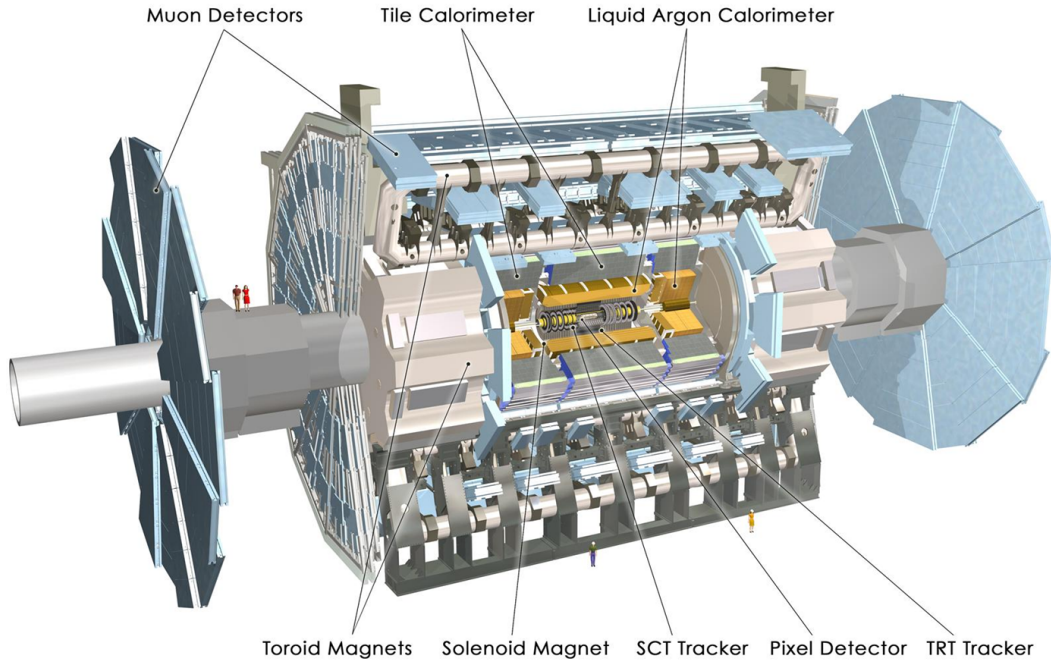


Figure 1.3 – The ATLAS experiment [6] installed in the underground facilities of the Large Hadron Collider at ~ 100 m below surface.

allows to reconstruct the spatial trajectories of the particles with an accuracy depending on the pitch of the strips, generally in the order of $80 - 200 \mu\text{m}$ [7]. Strip modules are commonly used in the outer layers of Particle Trackers. Pixel modules, on the other hand, are sensing elements that are arranged as a two-dimensional matrix where the pre-amplifier chips are placed directly below the sensors [8]. Pixel modules allow to reconstruct the spatial particle trajectories with a high precision – typically with a resolution in the order of $20 \mu\text{m}$. The Pixel technology is commonly used in the innermost detector layers of a Particle Tracker where determining the trajectories with high precision is of prime importance [7].

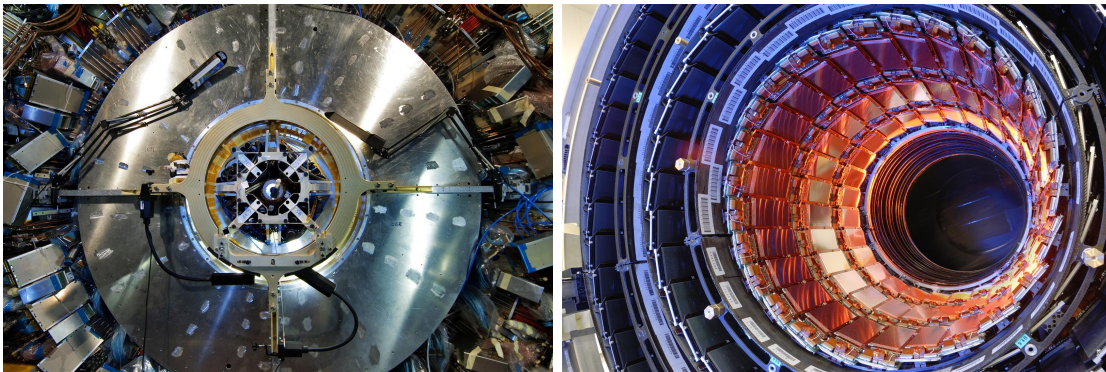


Figure 1.4 – Detector components of the Particle Trackers of the ATLAS and CMS experiments: The ATLAS pixel detector [9] (left) and the first half of the CMS inner tracker barrel [10].

1.4 High-Luminosity Phase-II Upgrades and Requirements for new Tracker Detectors

The main mid-term objective of CERN's scientific community is to increase the amount of collision data provided by the LHC and hence the potential for new discoveries. To meet the requirements of the future particle physics research programs, CERN's accelerator and detector facilities will undergo further developments within the next long shutdown scheduled for the years 2025-2027 [11]. The major activities during the Phase-II upgrade will concentrate on actions to increase the luminosity – defined as the particle flux or rather the amount of particles crossing a surface area per time – of the LHC by a factor of ten. The enhanced collision rate will greatly affect the detector systems, since the High-Luminosity Large Hadron Collider (HL-LHC) will present an extremely challenging environment to the LHC experiments, well beyond the parameters the current systems were designed for. The anticipated increase in luminosity, along with the associated data rate and accumulated radiation damage, make the current Particle Tracker detectors of ATLAS and CMS no longer suitable for long term operations. For that reason, both the ATLAS and CMS experiments decided to replace their current detectors with new silicon Particle Trackers [11],[12].

The estimated power dissipation of the future ATLAS Inner Tracker (ATLAS ITk) and the CMS Inner Detector are 0.3 MW and 0.5 MW respectively, while the level of radiation will increase by a factor of ten. Radiation-induced defects in the semiconductor lattice due to the high intensity of radiation – generally described as radiation damage – are a function of temperature and are strongly reduced in cold environments. To avoid premature aging and a deterioration of the detector performance before its designed lifetime, temperatures well below 0 °C are suggested. The higher the radiation exposure to the detector modules, in particular at the innermost layers of the Particle Tracker close to the interaction point, the lower the required temperatures [13]. Moreover, the temperature gradients at full detector power are rather high as a result of the moderate thermal conductance between the silicon detector modules and the evaporator lines inside the carbon-fiber support structures. Therefore, to cope with the increased radiation levels present at the LHC and to keep the sensors away from thermal runaway, both detectors will be operated at temperatures of –40 °C [14].

The semiconductor detector elements of the Particle Trackers are supported by carbon-fibre support structures – so-called "staves" in the barrel-, and "disks" in the end-cap regions – with integrated cooling lines. The specifications for the mechanical support structures imply that the particle interactions with the material, hence the energy losses, are minimized. This material characteristic is described by the radiation length^{II}. The design concepts for the future Trackers are based on the proven state-of-the-art staves currently installed in several experiments, e.g. the ATLAS IBL-Pixel detector. The carbon-fibre structures are designed such that the key requirements of (i) a minimized material budget of the support structures well

^{II}The target value to be minimized for detector components is the "material budget", X/X_0 , that is defined as the ratio of the material thickness and its radiation length.

below the target value ($X/X_0 < 0.67\%$), (ii) an enhanced thermal conductivity to maintain the sensors cold enough to avoid thermal runaway and (iii) a minimal deflection of the support structures of less than $150\ \mu\text{m}$ in the temperature range from room temperature down to $-40\ ^\circ\text{C}$, are met [15],[16],[17],[18]. Furthermore, to ensure the best accuracy possible during data collection of the experiments within the LHC runs, misalignment of the detector modules, e.g. due to structural misplacement as a consequence of thermal expansions, have to be avoided. Thus, it is of crucial importance to provide stable thermal conditions and reduce temperature fluctuations as much as possible.

Carbon dioxide (CO_2) has been identified as an environmentally friendly working fluid with very beneficial thermophysical properties that has the potential to replace synthetic refrigerants in scientific and industrial cooling applications [19],[20],[21],[22]. As illustrated in Figure 1.5, the saturation temperature of flow boiling CO_2 is less affected by pressure changes than commonly used refrigerants, what makes it a particularly well suited candidate for cooling applications in Particle Trackers, where the evaporator lines are long and the reduction of material is one of the key requirements. Combined with enhanced heat transfer properties, CO_2 is a promising solution to ensure homogeneous thermal conditions along the detector modules with reduced temperature gradients. Moreover, its high latent heat, dielectricity and radiation hardness make it an excellent candidate to replace Perfluorocarbons (PFC) currently used in HEP experiments. In addition, its non-toxicity and non-flammability are additional properties that are well appreciated in underground facilities. Cooling concepts based on Two-Phase Accumulator Controlled Loops (2PACL) refrigeration cycles using CO_2 as working fluid have already proven to be highly reliable and to achieve good performance in several HEP cooling applications, like the LHCb Velo [23], the CMS Tracker [24], the ATLAS IBL [25], and even in space applications like the AMS experiment on the International Space Station (ISS) [26]. Influenced by these arguments and experiences both the ATLAS and CMS collaborations have decided to use CO_2 for the thermal management of their next generation of Particle Tracker detectors installed within the high luminosity upgrades of the LHC.

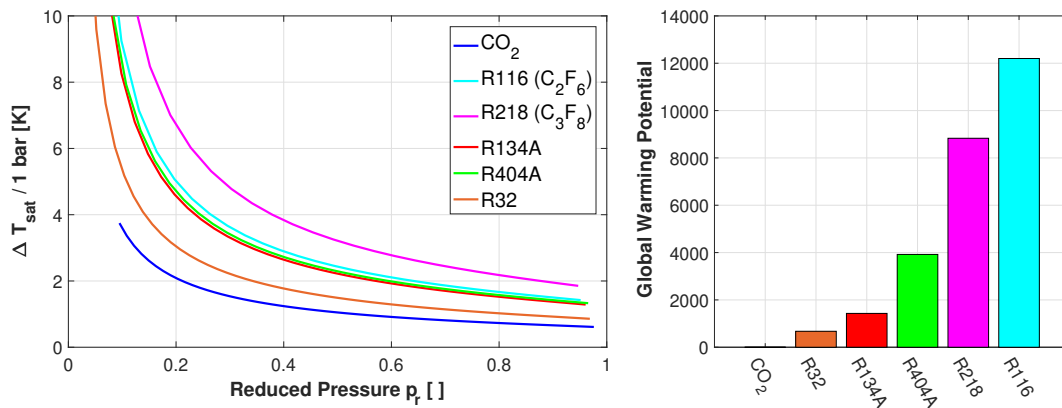


Figure 1.5 – Characteristics of CO_2 . Left: Change of saturation temperature due to pressure changes of 1 bar. The saturation temperature of CO_2 is less affected than other refrigerants. Right: Global Warming Potential of several refrigerants in comparison to CO_2 ($\text{GWP}_{\text{CO}_2} = 1$).

1.5 Nature of the Issue / Problem Statement

The detector systems of the LHC experiments are exposed to high intensities of radiation in the vicinity of the interaction points. To protect the environment from the high levels of radiation, HEP experiments are arranged in enclosed and isolated sectors. The ancillary service systems are typically deployed in shielded areas far from the harsh environment of the experimental setups. Both the ATLAS and CMS experiments have distinct caverns for their detector facility and the supply systems. The experimental- and the service caverns are separated by concrete walls and rock stratum of several meters of thickness. As a consequence, connecting the Particle Tracker detectors to the cooling plants requires long transfer lines and the routing of the piping needs to be thoroughly coordinated with plenty of other services, like signal and power cables, for example. The distribution of the working fluid, in particular to the CMS Inner Detector schematically illustrated in Figure 1.6, requires transfer lines with a total length in the order of ~ 100 m, consisting of horizontal and vertical segments of more than 20 m.

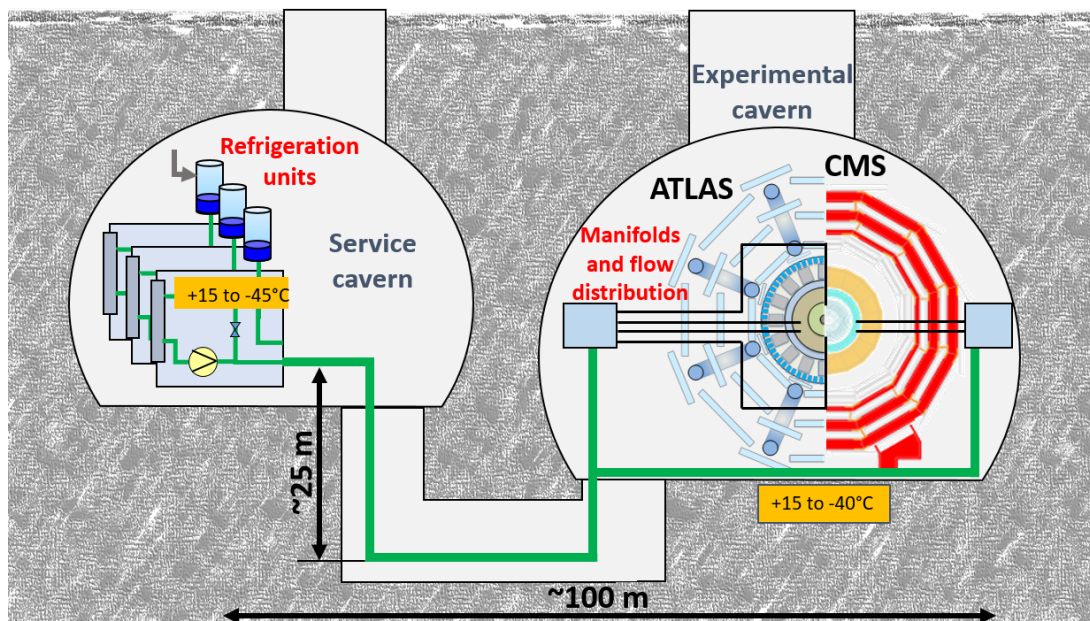


Figure 1.6 – Schematical illustration of the flow distribution between the cooling plants in the service caverns and the detectors facilities inside the experimental caverns.

The transfer lines are designed as a concentric arrangement of tubes, where the inner pipe supplies the manifold boxes on the detector level with single-phase liquid and the two-phase flow returning to the plant is traveling in opposite direction in the outer annulus. An outer vacuum jacket provides adiabatic conditions. The concentric concept allows heat exchange between the two streams and the transfer lines are acting like a countercurrent heat exchanger, bringing the liquid feed close to saturated conditions and triggering condensation in the two-phase return flow. In combination with the 2PACL concept, the temperature of the entire cooling loop is controlled via the saturation pressure inside the accumulator, that is connected to the return line, and the pressure builds up due to pressure drop in upstream direction.

Besides the off-detector flow distribution and the routing of the concentric transfer lines, the layout of the new Trackers will require long evaporator lines to evacuate the heat dissipated inside the detector. Whereas the evaporator lines in the barrel region are exclusively horizontal, the cooling lines of the disk-shaped end-caps – that are arranged radially to the beam pipe – have any orientation.

The concepts for the general thermal management of the future ATLAS and CMS Particle Trackers reveal, that the design of the cooling systems will be significantly influenced by the two-phase flow phenomena of CO₂. The temperature gradients of the evaporative flow are directly affected by the pressure losses in both the long evaporator- and the transfer lines and the temperatures of the detector elements are significantly influenced by the heat transfer mechanisms. Therefore, it is of crucial importance to have reliable prediction methods available to design the evaporative cooling systems properly. Miscalculation may lead to severe consequences, like a reduced performance, premature aging, or at worst, a thermal runaway of the detector.

Several experimental studies on horizontal flow boiling of CO₂ have been carried out and a considerable amount of data is made available. The flow boiling behaviour of CO₂ in vertical and inclined orientation, however, has not been investigated so far and there are no hints that such data sets are existing in the literature. As a consequence, more knowledge is required on flow patterns, pressure drop and heat transfer for CO₂ in both horizontal and vertical flow directions for accurately designing the new cooling schemes of the particle trackers.

1.6 Goal and Objectives

The objective of the present work is to address the lack of knowledge about the vertical two-phase flow behaviour of CO₂ and to provide engineering guidelines for the designers of the future Particle Tracker detectors installed within the High-Luminosity upgrades at the ATLAS and CMS experiments at CERN. The research goals can be divided into the following milestones and stages:

- Compilation of a database with measurements of the significant two-phase flow parameters of flow boiling CO₂ in different flow directions;
- Investigation of differences in flow behaviour and phenomena due to change of orientation;
- Validation of existing prediction models;
- Development of new prediction methods.

The research objectives of the present work are embedded into the project planning of the engineering activities ongoing in the "Detector Technology" group of the "Experimental Physics Department" at CERN (EP-DT-FS).

1.7 Methodology and Thesis Outline

The methodology to reach the research goals and aspirations of the present work are described by the following steps that likewise form the main body of the present thesis:

- **Data Collection with a dedicated Test Facility:** A test facility to investigate the flow boiling behaviour of CO₂ in horizontal, vertical up- and downward flow orientation has been built at the European Organization for Nuclear Research (CERN) and data sets of more than 3500 measurements of relevant two-phase flow parameters have been compiled. The details of the test rig – containing information with regard to the data recording and reduction, the experimental test conditions, the data acquisition and instrumentation, the commissioning and validation of the test rig – are summarized in Chapter II.
- **Flow Pattern Observations and Flow Pattern Maps:** Flow pattern observations in vertical upward (431) and downward (123) orientation have been recorded with a high-speed camera and analyzed with machine learning techniques. New transition criteria for the bubbly-to-slug, slug-to-churn and churn-to-annular transitions are suggested for both vertical upflow and downflow respectively and are presented with new flow pattern maps in Chapter III.
- **Pressure Drop:** Pressure drop measurements have been conducted in different pipe orientations and a database of 512 measurements in horizontal and 295 data points for each vertical up- and downflow respectively, has been compiled in Chapter IV. A subdivided analysis according to the flow patterns has been carried out and the best performing models are highlighted.
- **Heat Transfer Coefficient:** Heat transfer measurements have been carried out in vertical upward direction and a data set of more than 1940 data points has been compiled in Chapter V. The comparison of the measurements to the leading heat transfer prediction methods reveals that the majority of correlations underpredicts the experimental data. As a solution, an enhancement factor for flow boiling of CO₂ in vertical upward direction is suggested.

This manuscript is presented as a cumulative work of several articles that have already been published in journals or are currently under review. The content and the results of the articles appear verbatim and/or in substance within the present work.

2 The Test Facility

This chapter gives an overview of the experimental test facility built for the present study for investigating the two-phase flow phenomena of CO₂. At first, the layout and concept of the test facility is described, followed by its data acquisition and control system. Moreover, the methodologies of the data collection and reduction are elaborated and an overview of the uncertainties of the measurements is provided.

2.1 General Description of the Test Facility

The test facility can be subdivided into two parts, the refrigeration unit and the experimental test rig, where the measurements are conducted. Both are described in detail in the following sections.

2.1.1 Refrigeration Unit CORA

The refrigeration unit, named CO₂ Research Apparatus (CORA) [27], is a two stage cooling plant. The primary cooling system consists of a conventional chiller cycle using R404A as the primary working fluid, the secondary cooling system is based on the concept of a Two-Phase Accumulator Controlled Loop (2PACL) [28],[7] that uses CO₂ as working fluid. The saturation conditions of the entire system are controlled by condensing the vapour- and evaporating the liquid-phase inside a 27 l accumulator vessel, by means of a cooling loop, branched from the main chiller circuit, and a 1 kW electrical thermosyphon heater, both installed inside the accumulator. The heat exchange between the primary and secondary stage is happening in a copper-brazed heat exchanger (Alpha Laval, type AXP-14) designed for high pressure differences typically occurring in heat exchanging processes of CO₂ and low pressure refrigerants. The subcooled CO₂ is sent to the test rig via a membrane pump. The mass flow rate is measured with a *KROHNE OPTIMASS 3300C S03* Coriolis flowmeter and the measurements in steady-state conditions are within a standard deviation of 0.07 g s⁻¹ throughout all set points. For increasing the range of operating conditions, the initial pump

has been replaced with a LEWA membrane pump (type LDC1) within the scope of the present work, allowing increased mass flow rates up to ~ 24 g/s. The cooling capacity of the CORA refrigeration unit depends on the operating saturation temperature and is in the order of 2 - 4 kW. The entire plant – shown in Figure 2.1 – is described in detail by Bhanot et al. [27].



Figure 2.1 – Refrigeration unit CORA portrayed from different perspectives.

2.1.2 The experimental Test Rig

The test rig consists of three consecutive test sections to investigate the two-phase flow characteristics of CO_2 in horizontal ($\vartheta = 0^\circ$), vertical upward ($\vartheta = +90^\circ$) and vertical downward ($\vartheta = -90^\circ$) direction. Figure 2.2 shows the piping and instrumentation diagram (P&ID) of the test rig. The entire setup is built with smooth stainless steel tubes (EN 1.4404 / 316L) with inner and outer diameters of 8 and 10 mm respectively and the majority of the tube segments are joint together with seamless welding to minimize flow disturbances. The deviation of the inner tube diameter from the nominal value has been determined with micrometer measurements for several tube samples. A distance of $100 \cdot d_i$ is kept between the test sections and flow restrictions, like pipe fittings or bends, to ensure the flow is fully developed at the test section inlets. According to several studies, like Kew and Cornwell [29], Kandlikar [30] and Ong and Thome [31], the tube sizes of the present test facility for investigating the flow behaviour of CO_2 can be clearly assigned to macrochannels. The test sections are equipped with delicate instrumentation and features, like fragile glass tubes for flow visualization, for example, that

are designed to withstand pressures up to 45 bar. The test sections can be disconnected from the refrigeration plant by means of two shut off valves and a bypass allows to branch off the flow and short-cut the test sections. The pressure in the system is particularly high during the start-up procedure, where the fluid in the refrigeration unit is liquified by increasing the system pressure above saturated liquid conditions, and after the shut down of the refrigeration unit, when the system yields thermal equilibrium with the environment and the saturation temperature goes to ambient lab conditions. Hence, diverting the flow and running in bypass mode is essential in the start-up procedure to protect the delicate components at the test sections from being exposed to high pressure. As another safety measure, a pressure relief valve is installed at the test sections that has been calibrated to open at 42 bar. The test sections are described in more detail in chapters 3 – 5.

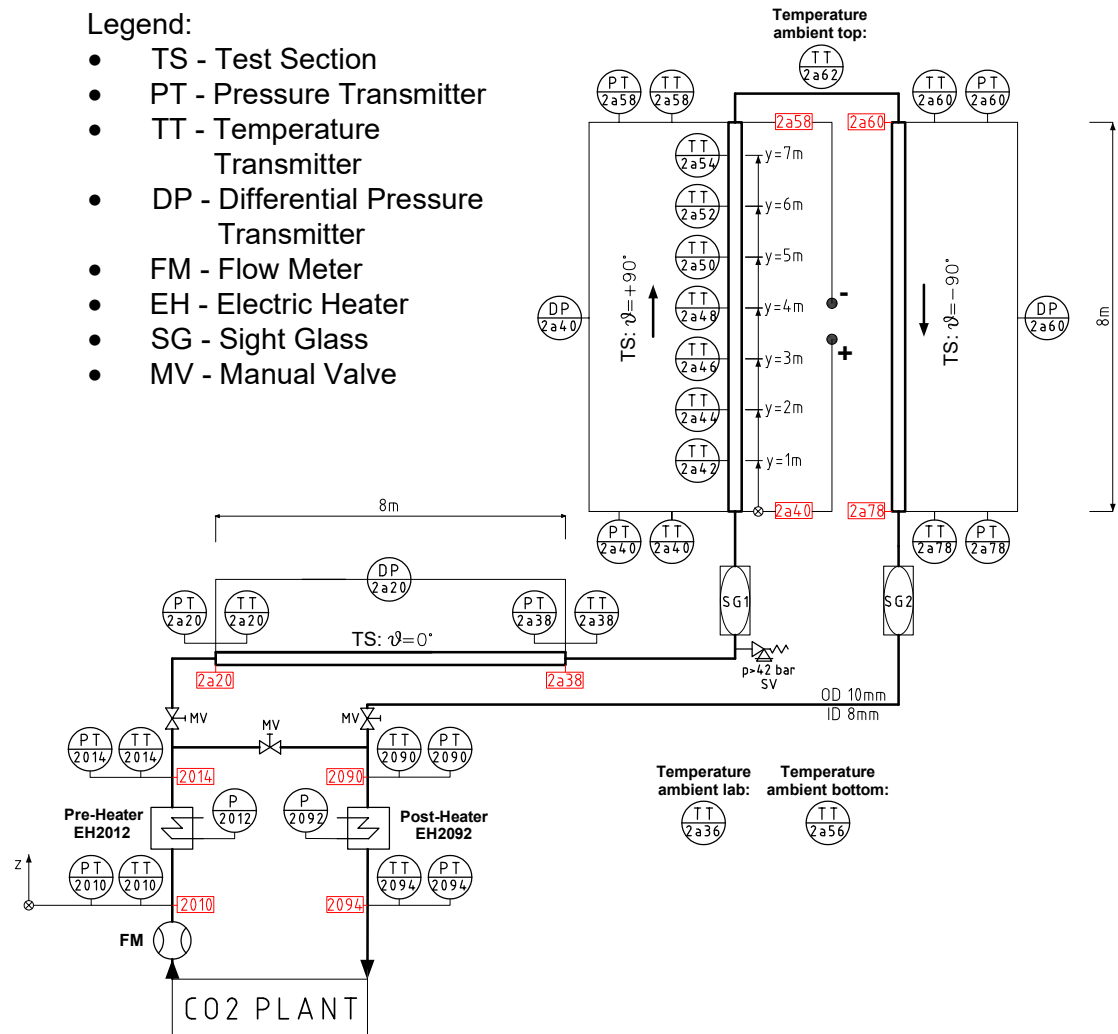


Figure 2.2 – Piping and instrumentation diagram (P&ID) of the test facility.

The temperature and pressure of the fluid are monitored at several locations along the test rig with absolute pressure transmitters and tailor-made RTD temperature probes (PT100). For

increasing the accuracy, the temperature sensors are soldered in 4-wire-configuration and the sensor tips, as well as the leads, are embedded in an epoxy resin that has high electrical and thermal insulation properties. This prevents measurement errors due to short circuits and severe heat fluxes from the stainless steel shaft – that is partly exposed to ambient – to the sensor tip. The temperature probes are inserted into the pipe at the pressure taps and the sensor tips are in direct contact with the flow. However, they are installed such that the flow is only minimally perturbed. The entire arrangement of instrumentation at the pressure taps is illustrated in the cross-sectional view in Figure 2.3.

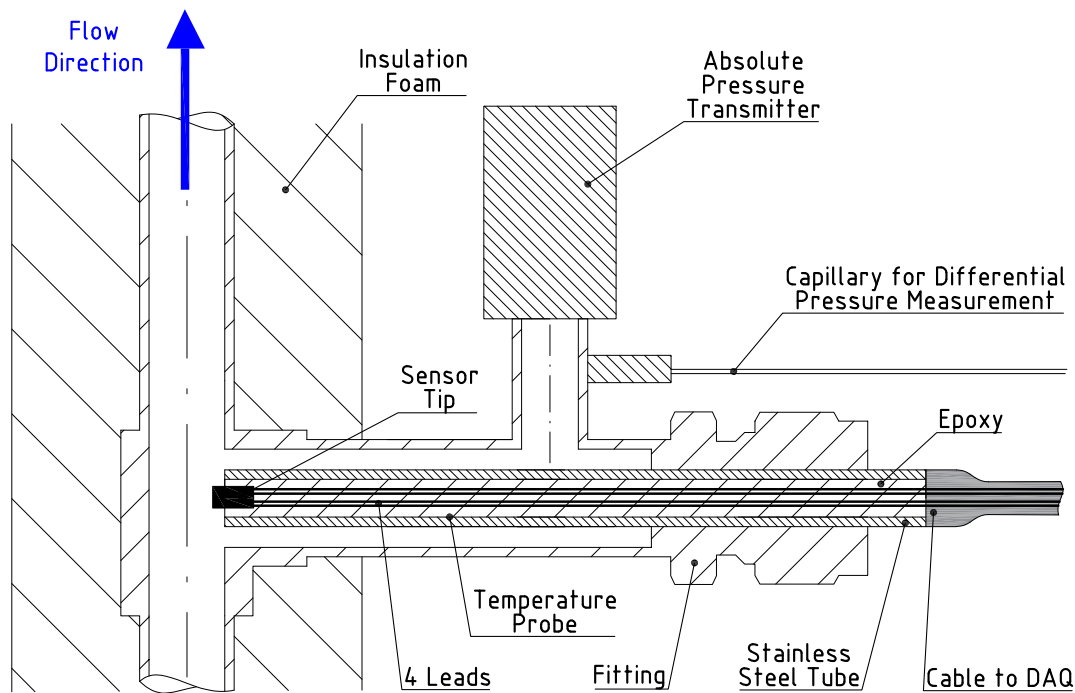


Figure 2.3 – Arrangement of instrumentation at the pressure taps.

The test rig is equipped with two 3 kW electrical heaters that are inserted into the flow at the in- and outlet of the setup. The pre-heater allows to set and control the enthalpy – and hence the vapour quality – at the inlet of the test rig at location 2014. The heater power is controlled with pulse-width modulation and is set according to the enthalpy of the subcooled flow at the inlet of the heater – determined at location 2010 – and the specified target value. The post-heater, installed at the outlet of the test rig, allows an assessment of the heat pickup from ambient over the entire setup by fully evaporating the remaining two-phase flow to the single-vapour phase. However, the post-processing analysis reveals that the assessment of the heat pickup based on the single phase energy balances, described in the following section 2.4, is more accurate than the one determined with the post-heater. Nevertheless, the information provided by the post-heater are useful for evaluating the order of magnitude of the heat pickup during operation of the system and for validating the results determined in the data analysis.

Figure 2.4 shows several segments of the experimental test rig.

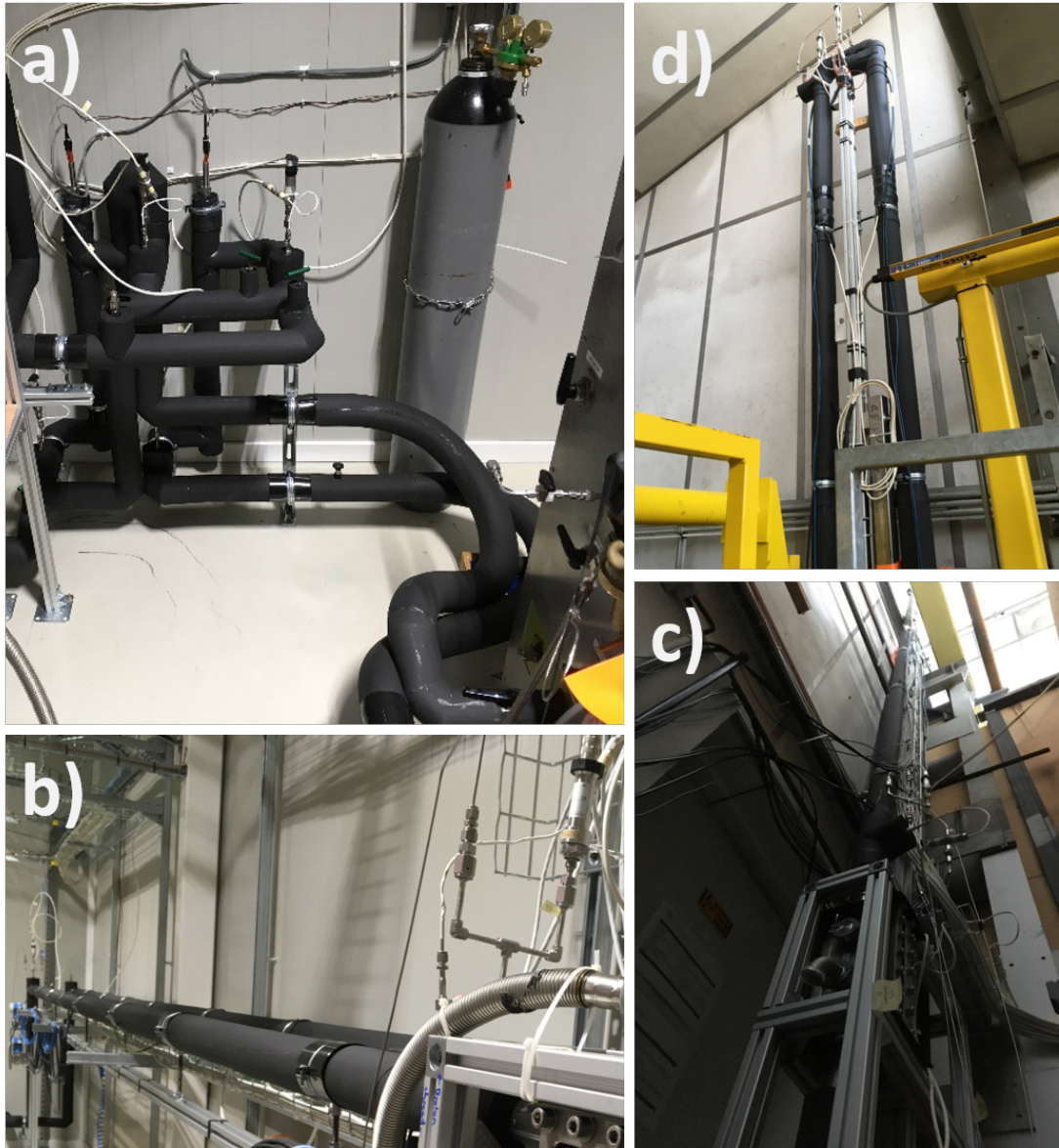


Figure 2.4 – Experimental test rig, portrayed at different sections. a): pre- and post-heater unit with bypass at the in- and outlet of the test rig and the connection to the refrigeration plant; b) horizontal test section (left pipe) and return line (right pipe); c) bottom view of vertical up- and downflow test sections; d) top view of vertical test sections.

2.2 Experimental Conditions and Test Matrix

The experimental domain of the present work is mainly defined by the limitations of the test facility and the test matrix has been designed according to the requirements of the new ATLAS ITk and CMS Inner Detector.

Saturation Temperature: The range of saturation temperature is limited by the chiller capacity of the refrigeration unit that defines the lower boundary. The upper limit is set by the maximum pressure the glass tubes of the transparent sections, that are installed for flow visualization, are able to withstand. Thus, the range of saturation pressure and temperature results in

$$16 \text{ bar} \leq p_{\text{sat}} \leq 40 \text{ bar} ; -26.5^\circ\text{C} \leq T_{\text{sat}} \leq +5.3^\circ\text{C}.$$

Mass Velocity: The upper limit of the mass velocity is defined by the maximum pump capacity. On the other hand, the lower boundary of the experimental range is determined by the mass flow rate where subcooled conditions at the test sections can be sustained. Due to the rather long transfer lines to the vertical test sections of the rig and the resulting heat pickup from ambient, the range of mass velocity is influenced by the difference between the ambient and the saturation temperature of the flow. In general, the mass velocity can be varied in the range of

$$100 \text{ kg m}^{-2} \text{ s}^{-1} \leq G \leq 450 \text{ kg m}^{-2} \text{ s}^{-1}.$$

Heat Flux: The heat flux provided by the evaporator due to ohmic heating is limited by the specifications of the power supply *DELTA ELEKTRONIKA SM 60-100*. The maximum current possible of 100 A results in a heat flux of

$$q = 11.4 \text{ kW m}^{-2}.$$

Vapour Quality: The range of vapour quality depends on the flow conditions and is influenced by the saturation temperature, the mass flow rate and the heating power applied to the entire system.

The experimental domain of the test facility has been determined during the commissioning procedure. The setup is not able to provide stable flow conditions with artificial heat load at temperatures below -25°C and/or mass velocities below $100 \text{ kg m}^{-2} \text{ s}^{-1}$. Furthermore, the max. heat load of the evaporator that the system is able to deal with, is a function of the saturation temperature and the mass flow rate. The range of parameters, where the setup is able to operate in stable conditions, is illustrated by the colour scale in Figure 2.5. The set points of the data collection are marked by the hatching and the numbers indicate the max. vapour qualities that can be reached in adiabatic conditions. In general, the data collection at the hatched set points has been carried out under adiabatic conditions ($q = 0 \text{ kW m}^{-2}$) and a heat flux of $q = 5 \text{ kW m}^{-2}$. The set points within the green zone allow additional measurements at a heat flux of $q = 11 \text{ kW m}^{-2}$. The vapour quality at each set point has been varied starting from $x = 0$ in steps of usually 5 % up to the maximum vapour quality the pre-heater is able to deliver, by keeping the system in stable conditions.

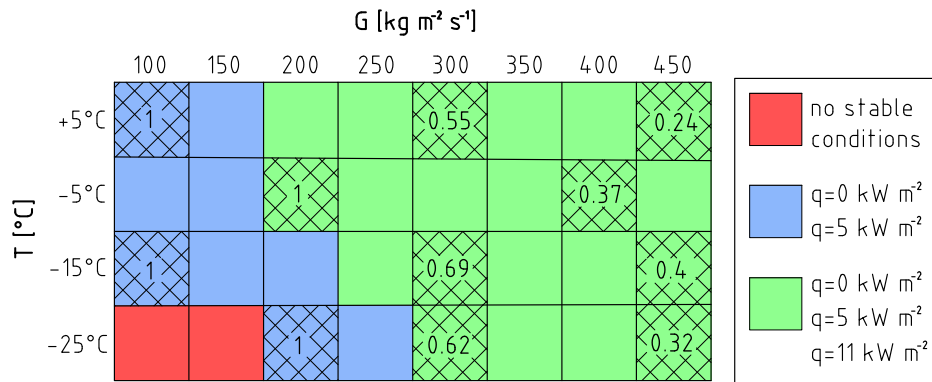


Figure 2.5 – Experimental domain and range of stable test conditions of the test facility (illustrated with colours). The test matrix of the data collection is marked by the hatching and the numbers indicate the max. vapour qualities that can be reached in adiabatic conditions.

2.3 Data Acquisition

The data acquisition of the instrumentation is integrated in the PLC based process control of the test facility. The calibration measures – explained in detail in the appendix – are implemented into the control logic and both the raw data as well as the calibrated measurements are archived. The properties derived from the direct measurements are calculated within the control logic. However, the properties calculated by the PLC are used for controlling and monitoring the system during operation only and are recalculated with a higher accuracy in the post-processing data analysis. The entire process control logic is embedded in CERN's UNICOS environment [32] and all measurements and process parameters are archived by the CERN Accelerator Data Logging Service [33]. The test facility is operated and monitored with CERN's Supervisory Control and Data Acquisition (SCADA) system and Figure 2.6 shows the control panel of the entire setup. The details of the control logic are summarized in its functional analysis [34].

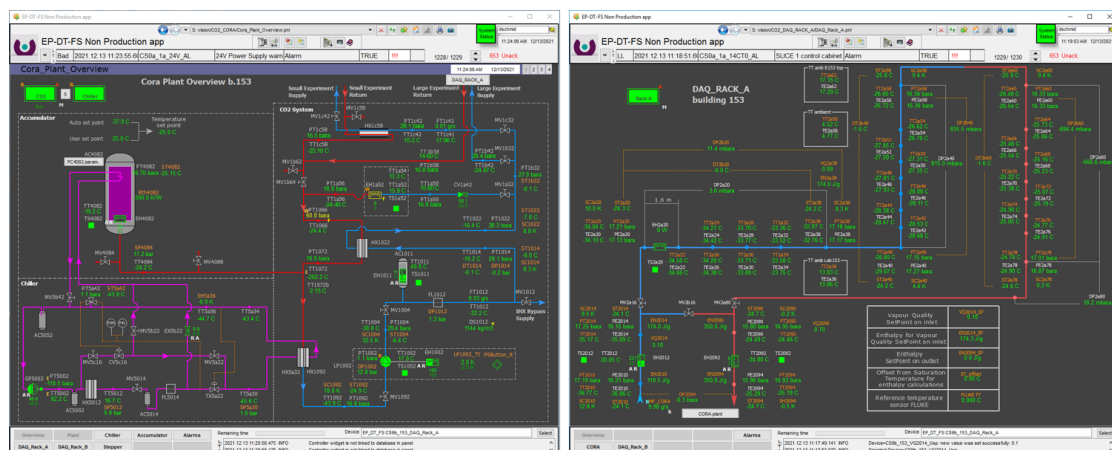


Figure 2.6 – SCADA control panel of the CORA refrigeration unit (left) and the test rig (right).

2.4 Validation of the Test Facility

The test facility has been verified with single-phase tests and calibration runs. This section gives an overview of the measures carried out to evaluate the performance and accuracy of the test rig.

2.4.1 Single-phase Pressure Drop

The accuracy of the differential pressure transmitters has been verified with single-phase pressure drop tests and the comparison of the single-phase measurements to the theoretical values according to Blasius [35] for $Re < 4000$ and Colebrook-White [36] for $Re \geq 4000$ are illustrated in Figure 2.7. The small deviations between the measured and the theoretical single-phase pressure drop values confirm the reliability of the instrumentation. Due to the high accuracy of the differential pressure transmitters, the uncertainty of the pressure measurements is neglected in the further analysis of the data.

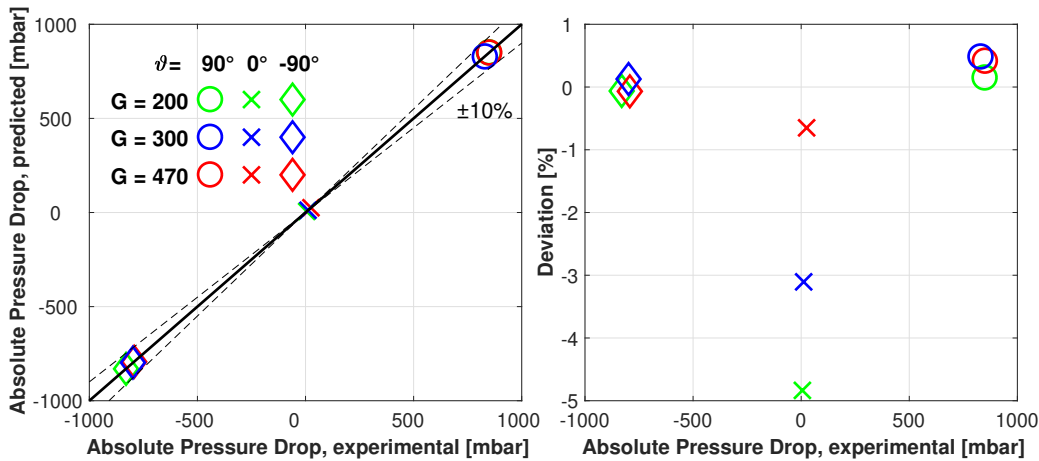


Figure 2.7 – Left: Experimental pressure drop measurements recorded by the differential pressure transmitters at the horizontal, the vertical up- and downward test sections compared to the analytical values according to Blasius [35] and Colebrook-White [36]. The dashed lines indicate an error band of $\pm 10\%$. The deviations between the experimental and the analytical values are shown on the right hand side.

In addition to the direct measurements of the differential pressure transmitters, the pressure losses are calculated as the differences between the absolute pressure measurements at the inlet and outlet of each test section, e.g. PT2a20 – PT2a38 at the horizontal test section. This redundancy allows to constantly validate the measurements and identifying emerging measurement drifts. Table 2.1 shows the pressure drop measurements during single-phase calibration runs directly recorded by the differential pressure transmitters, as well as the calculated pressure drops based on the differences between the absolute pressure measurements at the in- and outlets. For the sake of comparison, Table 2.1 also lists the theoretical pressure drop values derived from the analytical calculations [35],[36].

Table 2.1 – Comparison of single-phase pressure drops.

\dot{m} [kg s ⁻¹]	G [kg m ⁻² s ⁻¹]	mean average pressure drop [mbar]								
		analytical calculation			direct: dp-transmitter			indirect: inlet-outlet		
		0°	+90°	-90°	0°	+90°	-90°	0°	+90°	-90°
0.0153	303.62	11.96	827.24	-797.41	11.59	836.23	-803.43	14.51	820.65	-813.83
0.0234	465.48	25.32	848.07	-793.11	25.15	857.4	-798.38	24.83	841.56	-818.19

2.4.2 Single-phase Energy Balance

Energy balances are important measurements to assess the heat flow rates across the boundaries of a thermodynamic system. The heat pickup or losses of a system are particularly useful within the analysis of measurements, the evaluation of accuracies and the validation of insulation. The energy balance is defined as the difference between the energy applied to the system and the energy absorbed by the system.

$$\dot{Q}_{in/abs} = \dot{Q}_{in} - \dot{Q}_{abs} \quad (2.1)$$

This chapter exclusively deals with energy balances of the test facility, regardless of the detailed heat transfer mechanisms across its boundaries. For validating the results, some analytical calculations are carried out for comparison.

2.4.2.1 Energy absorbed by the Fluid

The first law of thermodynamics for an open system with a single-stream flow that is in steady-state conditions is defined according to

$$\frac{dE_{t,CV}}{dt} = \dot{Q} + \dot{W} + \dot{m} \left((h_1 - h_2) + \frac{c_1^2 - c_2^2}{2} + g(z_1 - z_2) \right) = 0. \quad (2.2)$$

In the present application, Eq. 2.2 is reduced to

$$\dot{Q} = \dot{m} (h_2 - h_1). \quad (2.3)$$

A thermodynamic system of a homogeneous single-phase fluid is entirely defined by the caloric equations of state $h = h(p, T)$ and $u = u(v, T)$ [37], where the specific enthalpy is defined as

$$dh = \left(\frac{\partial h}{\partial T} \right)_p dT + \left(\frac{\partial h}{\partial p} \right)_T dp. \quad (2.4)$$

The specific heat at a constant pressure is defined according to

$$c_p = \left(\frac{\partial h}{\partial T} \right)_p \quad (2.5)$$

and is – except for ideal, monatomic gases – a function of temperature $c_p(T)$. The energy absorbed by a single-phase flow, that does not undergo a change of phase and is kept at a constant pressure, can thus be derived from the first law of thermodynamics

$$\dot{Q}_{abs} = \dot{m} \Delta h = \dot{m} c_p \Delta T. \quad (2.6)$$

The increase of enthalpy of the liquid phase is directly determined with REFPROP from NIST [38] according to $\Delta h(\Delta p, \Delta T)$.

2.4.2.2 Energy Balance of the unheated Setup

The mean thermal bulk resistances of the insulated pipe sections are determined according to

$$\bar{R}_{m,i} = \frac{\Delta T_{fa,i} \cdot l}{\dot{m} \cdot \Delta h_i} \quad (2.7)$$

Figure 2.8 illustrates the temperature profile over the entire test setup during a single-phase run with pure liquid. As an approximation, the increase of the fluid's temperature can be described as a linear behaviour along the coordinate z . This concludes that the insulation is uniform and there are no severe differences over the entire test setup. On the other hand, it can be noticed that the ambient temperature profile varies along the piping. This can be explained by the size of the setup and the routing of the pipes through various labs with different scenarios of air-conditioning, as well as the change of altitude by about 10 m in a large room.

The thermal bulk resistance of the pipe insulation determined with the energy balances are validated with analytical calculations. The pipes are insulated with two layers of tube insulation foam with wall thicknesses of 9 and 32 mm respectively. The results of the analytical calculations, according to the simplified model shown on the right hand side of Figure 2.8, deviate by about $\pm 20\%$ and are hence in agreement with the experimental results.

2.4.2.3 Energy Balance of the Pre- and Post-Heater

The energy balances of the pre- and post-heaters, carried out with subcooled liquid, are illustrated in Figure 2.9. The errorbars represent the uncertainties determined in the appendix. The deviations are decreasing with increasing heater powers. Negative deviations, observed at low heater powers, indicate a heat pickup from ambient. At nominal heater powers above

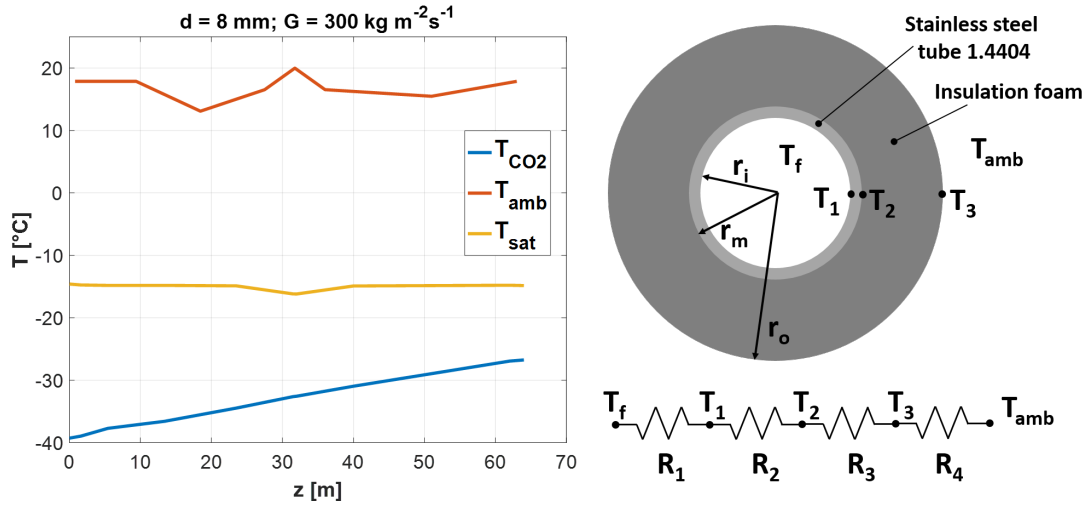


Figure 2.8 – Left: Temperature profiles of the single-phase flow, the saturation temperature and the ambient conditions over the entire setup during a single-phase run at $G = 300 \text{ kg m}^{-2} \text{ s}^{-1}$; right: Simplified model of the tube insulation.

400 W, what is the given case throughout all set points of the data collection, the energy balances of the pre- and post-heaters deviate in the order of $\pm 3 \%$ and $\pm 5 \%$ respectively.

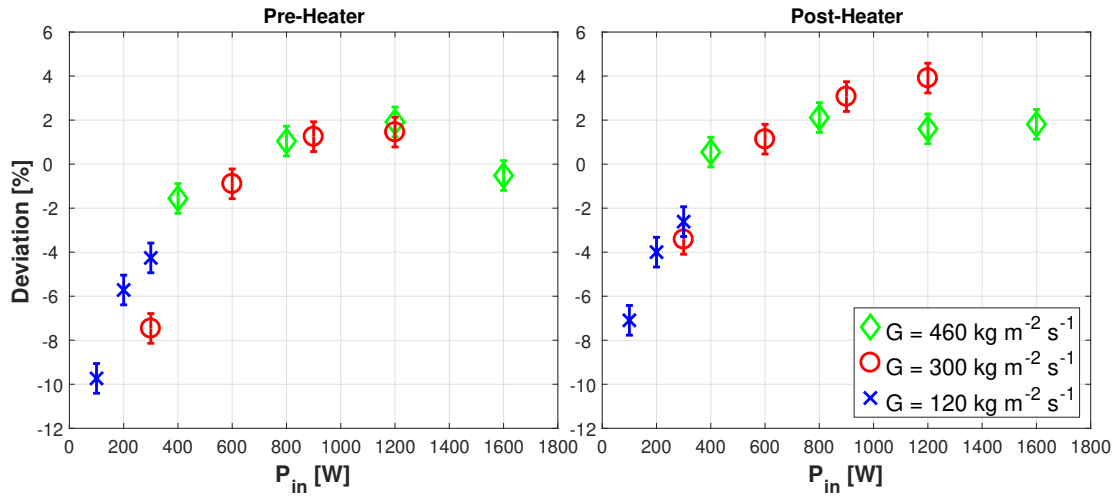


Figure 2.9 – Single-phase energy balances of the pre- and post-heater.

2.4.2.4 Energy Balance of the Evaporator

The energy balances and uncertainties of the evaporator are illustrated in Figure 2.10. At currents of 60 A, corresponding to heat fluxes in the order of 5 kW m^{-2} , the deviation is about $\pm 2 \%$. In general, the deviations show an asymptotic behaviour and yield towards zero with increasing evaporator power. The maximum current of 100 A provided by the DC power supply results in heat fluxes in the order of 11.4 kW m^{-2} .

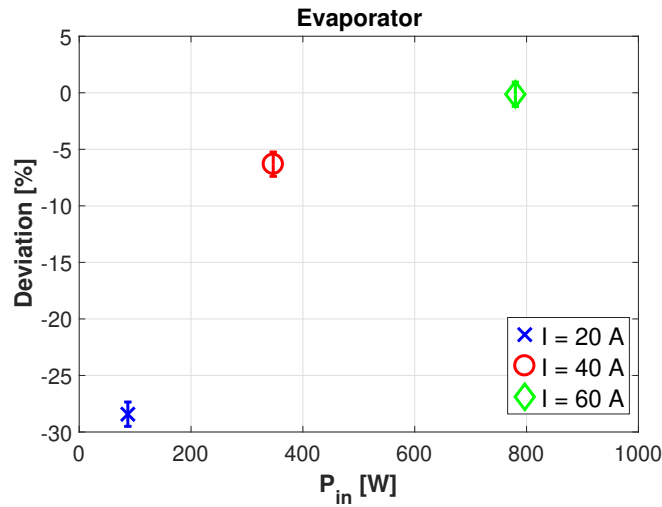


Figure 2.10 – Single-phase energy balance of the evaporator.

2.4.2.5 Diabatic single-phase Heat Transfer Tests at the Evaporator

The heat transfer measurements along the evaporator have been validated with diabatic single-phase calibration measurements. The comparison to the convective heat transfer models of Dittus-Boelter [39] and Gnielinski [40] shows a Mean Absolute Percentage Error of $\sim 14\%$ and $\sim 12.2\%$ respectively. The single-phase Nusselt numbers of the most accurate (TT2A42) and the worst measurements (TT2A48) are illustrated in Figure 2.11. The accuracy of the temperature probes has been verified with post-calibration sanity checks (see Figure 2 in the Appendix).

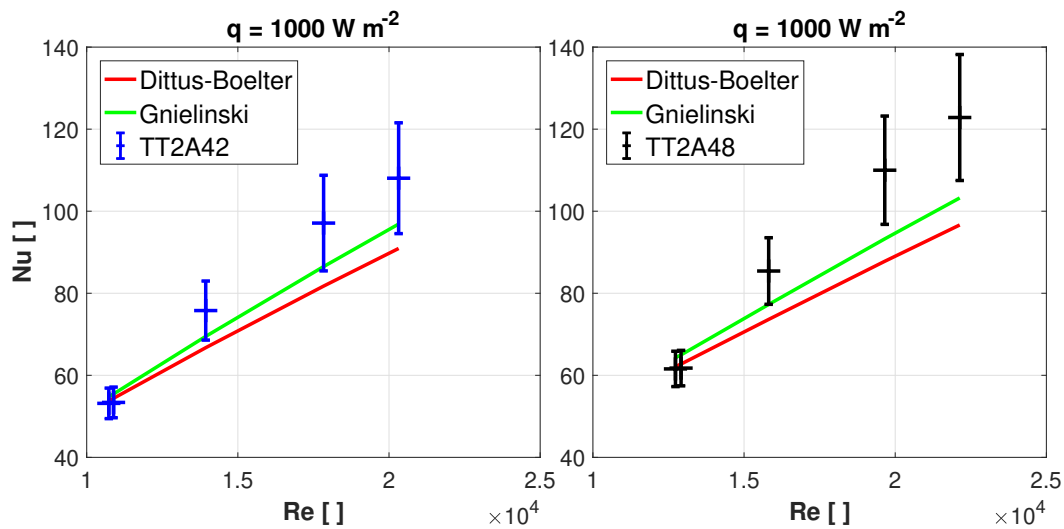


Figure 2.11 – Experimental Nusselt number of the most accurate (probe TT2A42, left) and the worst (probe TT2A48, right) measurements determined with calibration runs compared to the convective heat transfer models of Dittus-Boelter [39] and Gnielinski [40].

2.5 Data Collection and Data Reduction

2.5.1 Steady-state Conditions

The relevant measurements are carried out over a span of several minutes when the system is considered being in steady-state conditions. In order to obtain the final data points, the signals are averaged over the time of recording to moderate small fluctuations. The system is considered to be stable when the recorded signals of the following flow parameters do not exceed the maximum deviations specified as follows:

- mass flow rate: $\Delta \dot{m} < \pm 0.2 \text{ g s}^{-1}$
- saturation pressure of the accumulator: $\Delta p_{accu} < \pm 0.05 \text{ bar}$
- evaporator current and voltage: $\Delta I_{eva} < 0.01 \text{ A}$; $\Delta U_{eva} < 0.01 \text{ V}$

2.5.2 Derived Properties

Besides the direct measurements, the caloric state functions are essential to analyze the thermodynamic system. The single-phase enthalpy $h_{1p} = f(T, p)$ is determined according to section 2.4.2.1 based on the state variables pressure and temperature. The two-phase enthalpy at any location z of the setup before the evaporator is derived according to

$$\begin{aligned} h_{2p}(z) &= h_{1p,2010} + \frac{\dot{Q}_{EH1} + \dot{Q}_{amb}}{\dot{m}} \\ &= h_{1p,2010} + \frac{1}{\dot{m}} \left(\dot{Q}_{EH1} + \int \frac{\Delta T_{fa}}{\bar{R}_m} dz \right) \end{aligned} \quad (2.8)$$

where $h_{1p,2010}$ is the single-phase enthalpy of the subcooled liquid phase provided by the refrigeration plant at location 2010 in Figure 2.2. $\dot{Q}_{EH,1}$ denotes the heater power of the pre-heater, while \dot{Q}_{amb} represents the heat pickup from ambient across the insulation based on the thermal bulk resistance of the insulation \bar{R}_m – determined in section 2.4.2.2 – and the temperature difference ΔT_{fa} between the flow and ambient. The two-phase enthalpy at any location inside or after the evaporator is determined according to

$$\begin{aligned} h_{2p,eva}(z, y) &= h_{1p,2010} + \frac{\dot{Q}_{EH1} + \dot{Q}_{amb} + \dot{Q}_{eva}}{\dot{m}} \\ &= h_{1p,2010} + \frac{1}{\dot{m}} \left(\dot{Q}_{EH1} + \int \frac{\Delta T_{fa}}{\bar{R}_m} dz + \int_0^{L_{eva}} \frac{\dot{Q}_{eva}}{l_{eva}} dy \right) \end{aligned} \quad (2.9)$$

where \dot{Q}_{eva} denotes the entire evaporator power applied to the fluid at the evaporator coordinate y . Radial losses are neglected and it is assumed that all the heat dissipated by the

evaporator, the pre- and the post heater is applied to the flow. The calibration runs described in section 2.4.2 make this an appropriate assumption. The corresponding vapour quality at any location of the setup is derived from the enthalpy $h(z, y)$ and the local liquid- and vapour-phase enthalpies (h_l, h_v).

$$x(z, y) = \frac{h(z, y) - h_l}{h_v - h_l} \quad (2.10)$$

The heat fluxes encountered by to the flow are generally defined as the heat flow rates applied via the internal surface of the tube.

$$q = \frac{\dot{Q}}{\pi d_i l_{ts}} \quad (2.11)$$

The fluid properties are obtained using REFPROP of NIST [38] and all calculations are carried out with MATLAB [41].

2.5.3 Data Clustering

The architecture of the control system is designed such that the saturation pressure of the entire system can be controlled according to any pressure measurement of the test facility. This allows to control the saturation conditions right at the location where the experiments are carried out and the influences of the system's characteristics, in particular the influence of pressure drop, are diminished. However, to increase the efficiency of the data collection and to increase the size of the data sets, some experiments are carried out in parallel and measurements at different test sections are recorded at the same time. Hence, the local saturation conditions between the test sections vary due to pressure drop. Furthermore, the flow parameters show some correlation. Even though their impacts are not severe, it can be observed that the factors show a co-dependency and deviate from their nominal value due to set point changes. The variations of the flow parameters throughout the entire data set are listed in Table 2.2.

Table 2.2 – Variation by means of the standard deviation (STD) of the flow parameters throughout the entire data set.

	T [K]			\dot{m}	q
Position/Unit	2A20	2A40	2A78	[g s ⁻¹]	[W m ⁻²]
STD (σ_{STD})	0.275	0.212	0.279	0.07	0.045

2.5.4 Statistical Evaluation

The statistical evaluation of the experimental data is performed by means of the Mean Percentage Error (MPE), the Mean Absolute Percentage Error (MAPE) and the number of data points that fall into an error band of a defined percentage deviation (ξ_{xx}).

$$\text{MPE} = \frac{100}{N} \sum_{i=1}^N \frac{\Delta y_{exp,i} - \Delta y_{pred,i}}{\Delta y_{exp,i}} \quad (2.12)$$

$$\text{MAPE} = \frac{100}{N} \sum_{i=1}^N \left| \frac{\Delta y_{exp,i} - \Delta y_{pred,i}}{\Delta y_{exp,i}} \right| \quad (2.13)$$

2.5.5 Numerical Calculation

The numerical calculations are conducted with a resolution of 1,000 segments per test section. Increasing the resolution beyond 1,000 segments does not show a significant improvement in accuracy. As an example, the results of the pressure drop and heat transfer analysis varied by $< 0.01\%$ when increasing the resolution from 1,000 to 10,000 increments. Moreover, a resolution of $n = 1,000$ increments per test section, each with a length of 8 m, results in tube segments that are in the order of the inner tube diameter $\Delta l = d$. All calculations are carried out with MATLAB [41].

2.6 Uncertainties of Measurements and Properties

The uncertainties of the measurements and the derived properties are listed in Table 2.3. The calibration procedures, the accuracy of instrumentation, as well as the detailed derivation of the errors and uncertainties can be found in the appendix.

Table 2.3 – Uncertainties of the calibrated instrumentation and the property calculations.

Parameter	Brand / Type	Uncertainty of	
Pressure, p	KELLER PAA-33X	$\pm 0.07\%$	measur.
Temperature, T	PT100	$\pm 55 \text{ mK}$	measur.
Differential Pressure, Δp	E+H Deltabar S PMD75	$\pm 0.05\%$	abs. range
Mass Flow Rate, \dot{m}	KROHNE Optimass 3300C S03	$\pm 0.15\%$	measur.
Diameter, d	-	$\pm 1.1\%$	value
Mass Velocity, G	-	$\pm 1.56\%$	value
Enthalpy, single-phase, h_{1p}	-	$\pm 0.075\%$	value
Enthalpy, two-phase pre EVA, h_{2p}	-	$\pm 0.675\%$	value
Enthalpy, two-phase post EVA, $h_{2p,eva}$	-	$\pm 1.075\%$	value
Vapour Quality, pre EVA, x	-	$\pm 0.3\%$	value
Vapour Quality, post EVA, x_{eva}	-	$\pm 0.5\%$	value
Heat Flux, EVA, q	-	$\pm 1.5\%$	value
Heat Transfer Coefficient, α	-	$\pm 2.5 \dots 14.5\%$	value

3 Flow Pattern

The content and the results presented in this chapter have been published in:

- D. Schmid, B. Verlaet, P. Petagna, R. Revellin and J. Schifmann. "Flow pattern observations and flow pattern map for adiabatic two-phase flow of carbon dioxide in vertical upward and downward direction", *Experimental Thermal and Fluid Science*, 2021.
doi.org/10.1016/j.expthermflusci.2021.110526

Knowledge about the appearance and the spatial distribution of the co-current vapour and liquid phases is essential for designing evaporative cooling systems. Geometric structures of two-phase flows in ducts are characterized by a number of possible interface configurations that can be described and clustered to "patterns" (or "regimes"). Flow pattern maps are useful tools to describe the physical phenomena of two-phase flows and several studies, e.g. Kattan et al. [42],[43], Wojtan et al. [44],[45], El Hajal et al. [46] and Thome et al. [47], suggest that flow pattern maps have the potential to enhance the accuracy of prediction methods in channels. In this chapter, new flow pattern maps for two-phase flow of CO₂ in vertical upward and downward direction are presented.

3.1 Literature Review

3.1.1 Flow pattern maps for vertical two-phase flow in macroscale tubes

Existing flow pattern maps can be classified according to the approaches and strategies followed for their development. Many studies are of experimental nature, where flow pattern data are used to analyse and determine the flow pattern transitions, like the early works by Hewitt and Roberts [48] and Bennett et al. [49], for example. Contrary to this, theoretical approaches derive criteria for concluding on flow pattern transitions by analysing the physical mechanisms that govern the flow pattern transitions. Like this, Taitel et al. [50] elaborated transition models in a theoretical way and verified their theories with experimental data of water-air mixtures in retrospect. In a similar manner, Barnea [51] presented a unified flow

pattern map for gas-liquid flows for all kind of pipe inclinations. It combines studies on horizontal and slightly inclined tubes [52],[53],[54], studies on vertical upward [50],[55],[56], vertical downward [57] and on inclined up- and downward flows [58],[59],[60].

Rouhani and Sohal [61] conducted a comprehensive literature review with regards to two-phase flow regimes, detection methods, transition criteria, effects of boundaries and external conditions and on existing flow pattern maps. In a similar manner Cheng et al. [62] carried out a comprehensive review focusing on gas-liquid two-phase flow patterns and flow pattern maps at adiabatic and diabatic conditions, including natural working fluids, like ammonia and CO₂. However, vertical two-phase flow of CO₂ has not been treated in both studies.

Many studies, in particular in the 20th century, were initiated by the petrochemical industry and the energy sector, where energy conversion was mainly based on thermodynamic cycles in fossil and nuclear power plants. Hence, most studies at that time were conducted with mixtures of petrochemicals as well as water-steam or, due to simplicity, more often with water-air mixtures. The fluid properties – especially those of petrochemical products – differ significantly from CO₂.

3.1.2 Flow pattern observations and maps for horizontal two-phase flow of CO₂

Investigations on flow patterns of CO₂ started with the increasing significance of natural refrigerants at the beginning of the 21st century and were mainly focused on horizontal microchannel-cooling for the HVAC, the power production and the microelectronics industries. The first studies, like the ones from Pettersen [63],[64] carried out flow pattern studies in a horizontal glass tube with a bore diameter of 0.98 mm at temperatures of 0 °C and 20 °C and for mass velocities ranging from 100 to 580 kg m⁻² s⁻¹. Yun and Kim [65] visualized the flow boiling process of CO₂ in a horizontal rectangular channel (16x2 mm) at various test conditions and developed a flow pattern map for horizontal narrow rectangular channels. Schael and Kind [66] presented flow pattern observations and measurements of the heat transfer in a helical grooved micro fin tube and compared those to the results of a smooth tube. They concluded that there is a co-dependence between the transition vapour quality and mass velocity. Gasche [67] conducted studies on CO₂ evaporation inside a horizontal 0.8 mm hydraulic diameter single-microchannel. The flow patterns were visually observed at a saturation temperature of 23.3 °C, a heat flux of 1800 W m⁻², vapour qualities from 0.005 to 0.88 and mass velocities ranged from 58 to 235 kg m⁻² s⁻¹. Three flow regimes had been identified within that study: plug flow at low vapour qualities ($x < 0.25$), slug flow ($0.25 < x < 0.5$) and annular flow ($x > 0.5$).

Thome and Ribatski [68] summarized two-phase flow pattern observations of CO₂ available at that time in a "state-of-the-art" review. Within that work, data of some of the previously mentioned studies were compared to the horizontal flow pattern map for CO₂ of Yun and Kim [65] and the universally applicable maps of Thome-El Hajal [69] and Steiner [36]. None of the

maps was able to predict the flow pattern transitions of the CO₂ data properly.

Cheng et al. [70],[71] published an updated flow pattern map, based on the work of Wojtan et al. [44], for horizontal two-phase flow of CO₂ that is intrinsically related to the corresponding heat transfer mechanisms. Later, this work has been updated by Cheng et al. [72] and a map with an extended range of validity has been presented.

Mastrullo et al. [73] carried out flow visualizations during flow boiling of CO₂ in a horizontal smooth tube of 6 mm inner diameter and identified flow regime transitions from slug-to-intermittent, intermittent-to-annular and at the dryout inception. They varied the mass velocity from 150 to 500 kg m⁻² s⁻¹ and the reduced pressures from 0.57 to 0.64 during their experiments. This corresponds to saturation temperatures of 7.3 °C and 12 °C and is therefore far from the low temperature operation in HEP detectors.

In their most recent review, Cheng et al. [74] summarized flow pattern visualizations of CO₂ two-phase flow conducted after 2007 and compared them to the generalized flow pattern map [72]. Good agreement between the new flow pattern observations and the generalized flow pattern map has been found. However, vertical flow pattern observations are not mentioned in this study.

3.1.3 Nature of the issue and objective of the present chapter

Literature offers a large number of flow pattern maps for any kind of pipe orientation for liquid-gas mixtures, water and synthetic refrigerants, while several flow regime observations are available for horizontal CO₂ two-phase flow, mainly for microchannel applications. However, there are no flow pattern observations available for vertical two-phase flow of CO₂ and as a consequence, there is no validated flow pattern map available for vertical orientations. The objectives of the present chapter are new flow pattern maps that describe the flow pattern transitions of vertical two-phase flows of CO₂.

3.2 Experimental Methodology and Database

3.2.1 Transparent sections and visualization techniques

The vertical test sections of the test facility are equipped with transparent sections for flow visualization at ground level, i.e. at the inlet in vertical upward and at the outlet in vertical downward direction, as illustrated in the P&ID in Figure 2.2. The transparent sections are designed modular, such that their positions can be changed within the setup. The main components of the transparent sections are thick-walled glass tubes with the same inner diameter as the stainless steel tubes (8 mm) and an outer diameter of 34 mm to withstand the high pressures of CO₂. For safety reasons, the glass tubes are surrounded by a stainless steel box with flat sight glasses at front- and back side respectively and a vacuum is applied inside the stainless steel box to reduce heat fluxes to the glass tube. The saturation pressure and temperature are monitored right at the transparent sections. The installed instrumentation has been calibrated and the uncertainties are summarized in Table 2.3. A digital high-speed camera PHOTRON FASTCAM Mini AX is installed on a mechanical support frame, that can be switched to face any of the transparent sections. High-speed frames and videos were recorded at two different camera settings that are listed in Table 3.1. The refraction due to the thick-walled glass tubes are taken into account according to the approach by Fu et al. [75]. For calibrating the refraction effect, a calibrated checkerboard pattern was inserted into the glass tubes and images were recorded with the high-speed camera prior to data collection. Figure 3.1 illustrates a cross-sectional view of the transparent section and the camera setup during operation.

Table 3.1 – Camera settings for the recording of the high-speed images

Parameter	Settings 1	Settings 2
Resolution	512 x 512	384 x 384
Frame rate	13600 fps	
Shutter speed	1/300000 s	
Period of time recorded	1.61 s	2.86 s
No. of frames recorded	21850	38840
Percentage of data archived	10 %	

3.2.2 The Database

Flow pattern observations in vertical upward and downward direction have been carried out one after another, starting with the vertical upward direction configuration, and then swapping the camera to the transparent section of the vertical downflow and repeating some of the experiments. A total of 431 data points have been collected for vertical upflow and 123 data points for the vertical downflow configuration. Figure 5.2 gives an overview of the histograms of the test data, that further describe the flow pattern observations used for the flow pattern analysis.

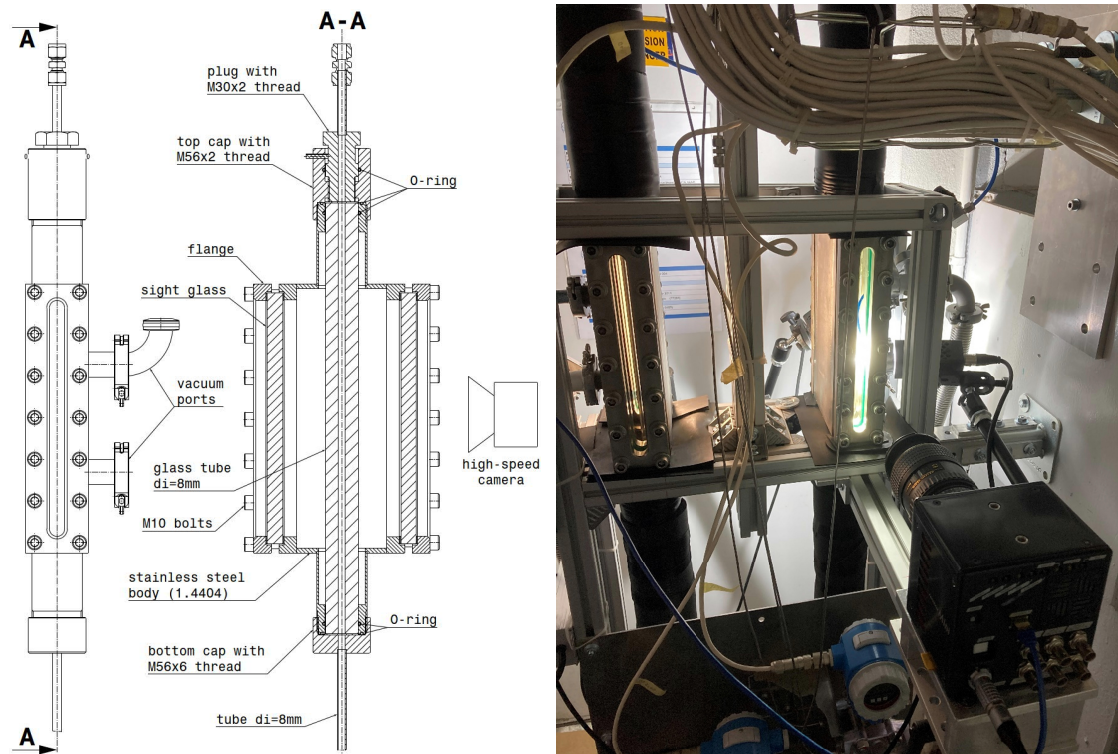


Figure 3.1 – Transparent section for flow visualization; sectional view (left) and during operation (right).

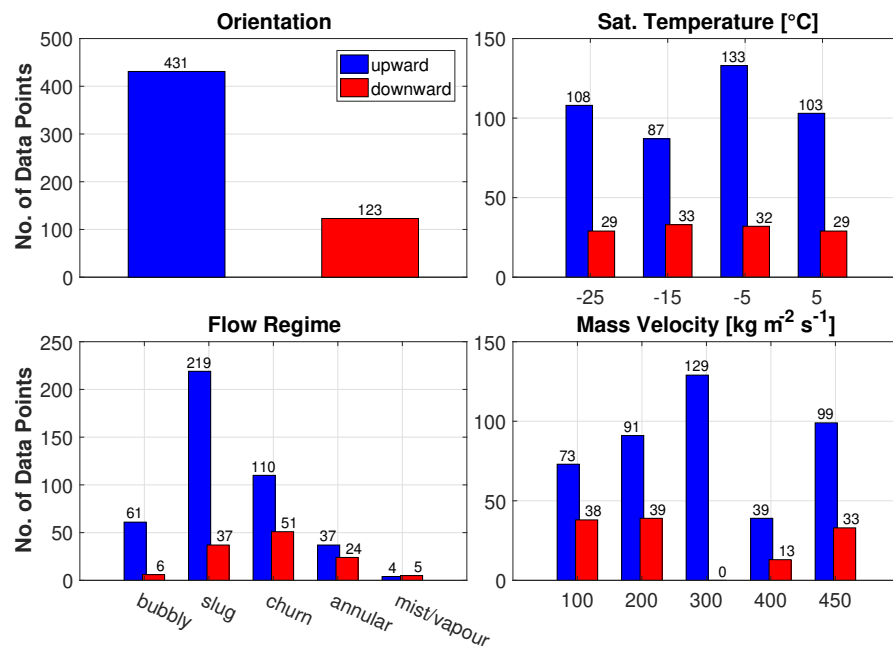


Figure 3.2 – Histograms describing the experimental database.

3.3 Flow Pattern Observations and Transitions

The variety of flow pattern classifications appearing in literature is diverse and only few are commonly accepted, like the ones in Figure 3.3. The main flow regimes observed in vertical upflow ($\theta = +90^\circ$) during operation of this test facility and their transition criteria are described and discussed in the following.

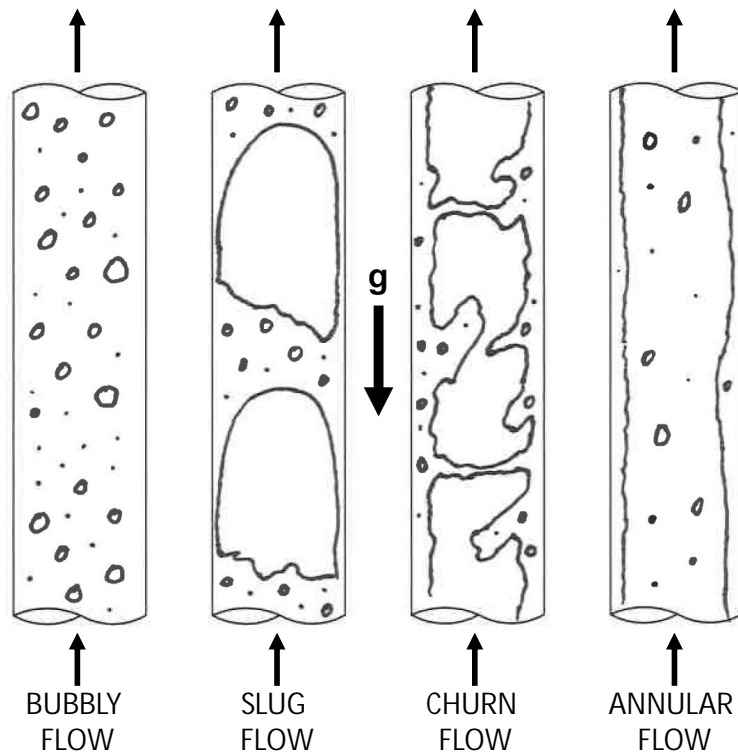


Figure 3.3 – Typical two-phase flow patterns in vertical upward direction ($\theta = +90^\circ$).

Bubbly Flow: The vapour phase is uniformly dispersed in the continuous liquid phase as bubbles that may vary in size and shape. However, they are significantly smaller than the tube diameter and generally tend to be spherical [76]. In the bubbly regime, except for very low mass velocities, where buoyancy effects become noticeable, the ratio of the phase velocities is close to unity and no severe slippage can be observed. This flow pattern develops at vapour qualities around zero and is likely to appear even before the fluid reaches saturated conditions, where subcooled boiling occurs.

Slug Flow: With increasing vapour fractions, the bubbles start to coalesce forming larger bubbles nearly in the size of the inner tube diameter. These bubbles typically appear similar to the shape of a bullet with a characteristic hemispherical front and a fluctuating tail in flow direction. They are commonly denoted as “Taylor-Bubbles” [76]. The tube perimeter is

typically wetted by a liquid film that – in upward direction – may flow in opposite direction due to gravity [77]. Liquid slugs carrying small bubbles are bridging the pipe perimeters and separate the Taylor-Bubbles from one another. Buoyancy affects the velocity of the phases and in upward direction the net average velocity of the vapour phase is typically higher than the one of the liquid. The Taylor-Bubbles are getting longer as vapour quality increases and as a consequence the liquid slugs appear at lower frequencies.

Churn Flow: This flow regime is characterized by a chaotic mix of the phases. It starts developing when the liquid slugs are getting instable and begin to collapse. The local flow direction of the liquid may oscillate between up- and downflow, yet with a net flow in upward direction [76]. In the transition from slug to churn, the vapour concentration (void fraction) in the liquid slugs reaches its maximum and the turbulent wake behind the preceding Taylor-Bubble starts affecting the nose of the following. The transition criteria to churn flow is defined by liquid slugs that are not sustained. Hence, their frequency drops to zero.

Annular Flow: Annular flow is characterized by the continuity of the vapour phase in the pipe core with the liquid phase expelled from the centre to the tube perimeter. The main fraction of the liquid phase flows as an annulus - giving the name of the flow regime - at the inner pipe surface and partly as droplets entrained in the vapour core. The velocity of the vapour phase is typically much higher than the one of the liquid annulus. In vertical upflow the liquid film is lifted by the shear forces of the vapour core. However, at low mass velocities, the gravitational forces might exceed the shear and the liquid film flows in opposite direction [78],[79]. In the transition from churn to annular flow, the liquid phase is not able to bridge the tube perimeters anymore and the vapour in the pipe core is able to travel freely without being interrupted by the liquid. However, there are no discrete criteria to determine the transition from churn to annular. Hence, it is more a continuous change from a chaotic and turbulent state to a rather steady flow. Furthermore, oscillations between both flow regimes can be observed in the transition phase, where sequences of one regime are followed by sequences of the other.

Mist and Vapour Flow: This flow pattern can be seen as the inverse of pure liquid at the onset of bubbly flow where the vapour phase is continuous and liquid is present only as small entrained droplets. The tube surface is in direct contact with the vapour phase and the annular liquid film has dried out, which defines the characteristic transition criteria from annular to mist and vapour flow. In contrast to horizontal flows, the dryout in vertical direction is happening symmetrically and no partial break up of the liquid film due to gravity can be observed. Hence, mist or vapour flow only occurs when the mass fraction of the liquid phase is nearly zero. In turn, the mass fraction of the vapour phase is close to one and the droplets sometimes persist even beyond that point in the superheated vapour phase.

The flow pattern observations at the vertical upflow test section reveal that both the liquid- and vapour-phases are streaming in upward direction as a co-current two-phase flow throughout the entire range of flow parameters. Moreover, the analytical evaluation based on several flooding methods summarized in [80] confirms that flow reversal is not an issue within the flow regimes of the present test campaign. Figure 3.4 shows an example of flow pattern observations of CO₂ in vertical upward direction recorded at the CERN test facility at a saturation temperature of $-25\text{ }^{\circ}\text{C}$ and a mass velocity of $200\text{ kg m}^{-2}\text{ s}^{-1}$. Throughout all experiments, running from low to high vapour qualities, the sequential passing through the previously described flow regimes can be observed.

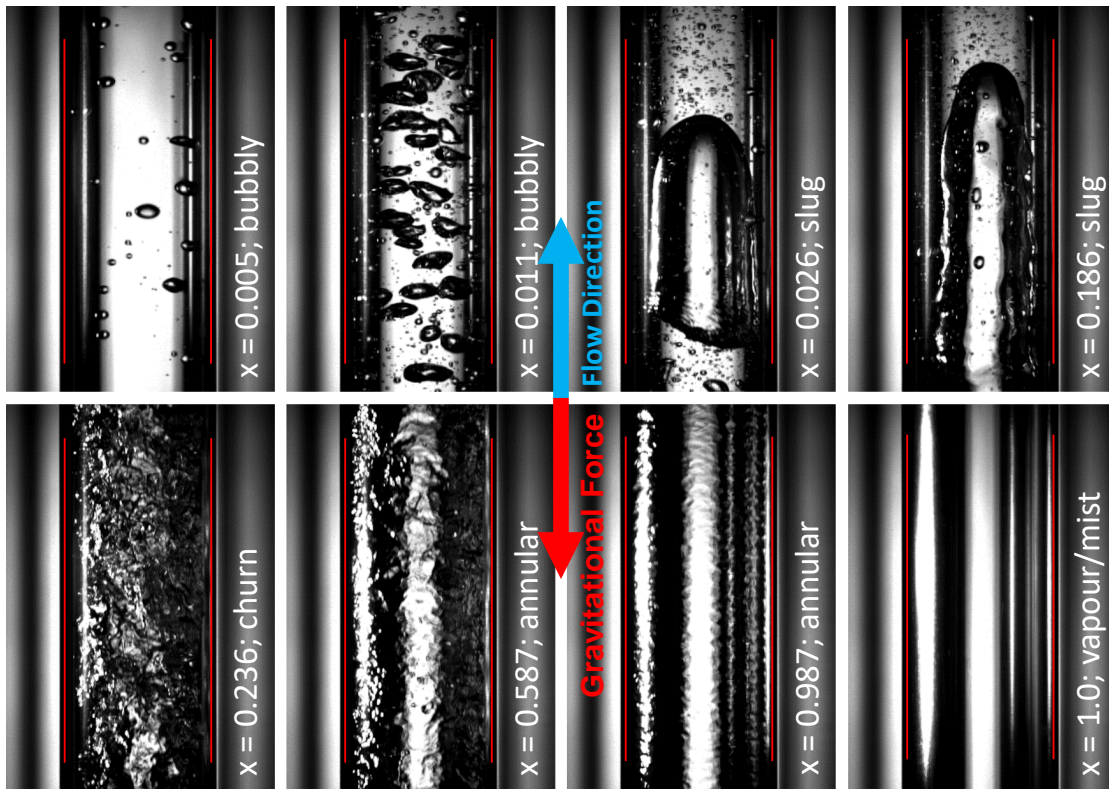


Figure 3.4 – Flow pattern observations of CO₂ in vertical upward direction ($\vartheta = +90^{\circ}$) at $T_{sat} = -25\text{ }^{\circ}\text{C}$; $G = 200\text{ kg m}^{-2}\text{ s}^{-1}$; vapour quality increasing from top left to bottom right: bubbly, bubbly, slug, slug, churn, annular, annular, vapour/mist. The red lines represent the inner tube walls.

Flow patterns in vertical downflow ($\vartheta = -90^{\circ}$) are observed to be similar to those of vertical upflow. However, there are some differences, mainly due to the buoyancy force that is opposed to the flow direction. In bubbly flow, in particular at low mass velocities, the flow directions of the vapour and liquid phases might be counter-current. Tiny bubbles are hardly affected by buoyancy and are therefore travelling downward at a velocity that is in the same order as the liquid phase. With increasing bubble sizes, buoyancy is increasing and the bubbles are slowed down, stagnant or even rising in counter-current direction. However, big Taylor-Bubbles

similar in size to the tube diameter are pushed downwards by the inertia of the liquid flow. In slug flow the nose of the Taylor Bubbles might appear flattened and the tail rounded. In some flow conditions it can be observed that the nose as well as the tail are constantly interacting and coalescing with bubbles and hence both do not show well defined boundaries as it is usually the case in upward direction. Besides the different flow direction, annular and mist downflow do not show significant differences to upflow. Figure 3.5 shows an example of flow regimes observed in vertical downflow at a saturation temperature of $-25\text{ }^{\circ}\text{C}$ and a mass velocity of $200\text{ kg m}^{-2}\text{ s}^{-1}$.

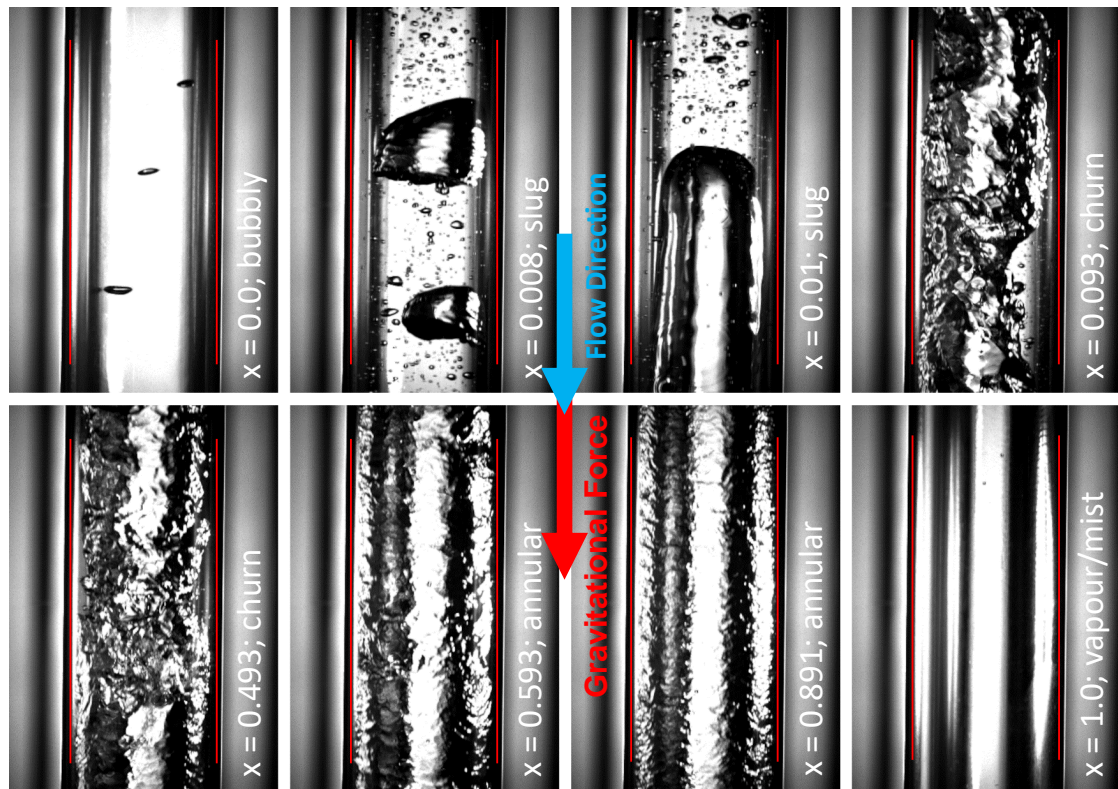


Figure 3.5 – Flow pattern observations of CO_2 in vertical downward direction ($\theta = -90^\circ$) at $T_{\text{sat}} = -25\text{ }^{\circ}\text{C}$; $G = 200\text{ kg m}^{-2}\text{ s}^{-1}$; vapour quality increasing from top left to bottom right: bubbly, slug, slug, churn, churn, annular, annular, vapour/mist. The red lines represent the inner tube walls.

3.4 Flow Pattern Detection Methods

Identifying and distinguishing flow patterns properly with the naked eye is challenging in two-phase flows, in particular at high flow velocities. Therefore, the majority of data reported in the literature has been acquired by taking advantage of high-speed imaging and by identifying the flow pattern transitions by visual evaluation of the records. However, some flow regime changes, e.g. from churn to annular, are a rather continuous transition with no distinct criteria – like the frequent appearance of liquid slugs – clearly defining the transition to neighbouring flow regimes. As a consequence, the flow pattern classification based on visual observation remains a subjective appraisal of the observer.

In order to obtain unbiased results, Rouhani and Sohal [61] summarized several methods of flow regime classification, like the direct observation methods of high-speed photography, X-ray attenuation, electrical contact probes, or indirect determination methods like static pressure oscillation analysis. At a later point, improved optical measurement and signal processing techniques were implemented for the characterization of flow patterns. Revellin et al. [81] made use of laser- and photodiodes for the characterization of flow patterns in microtubes, whereas Wu and Duan [82] investigated means to classify flow regimes and void fraction measurements by using collimated infrared laser light.

In the present study, the recorded high-speed videos are analysed using machine learning based computer vision techniques, which consider information found within an image frame that is unobservable to a human, due to the information's subtlety and complexity. A Convolutional Neural Network (CNN), based on the ResNet architecture [83], has been trained on a balanced dataset of 39,261 input frames that can be clearly assigned to any of the typical two-phase flow classes specified in the previous section 3.3. The CNN is used for frame classification and image feature extraction. For the flow regime classification, a deep long short-term memory (LSTM) network [84] is used to capture temporal information present in a sequence of image sets, since the definition of flow regimes is not only characterized by the spatial distribution of the gas and liquid phases but also by the way in which it changes over time. As a result, a Frame- and Flow-Regime-Classifer [85] has been built, that allows to analyse high-speed videos and outputs the percentage of the video's constituent frame- and flow regime classes. In addition to the commonly accepted flow patterns specified in 3.3, classes that represent transitional zones between the classical flow regimes are introduced to achieve a higher resolution and better performances in the regime classification. The definition of the thresholds, where the transitions are taking place, are still the decision of the observer. However, this tool provides objective numbers based on which the decisions can be made. By validating the Frame- and Flow-Regime-Classifer with 26,200 "unseen" data points, an accuracy of 95.4 % for the flow regime classification has been identified. The Frame- and Flow-Regime-Classifer is explained more in detail by Kadish et al. [85].

3.5 Flow Pattern Observations compared to existing Transition Lines

A fundamental question in further analysing the flow pattern observations of CO₂ is whether the flow regime transitions can be properly described by generalized flow pattern maps available in literature. Figure 3.6 compares all data in upward direction to the work by Barnea [51], that is one of the most widely used flow pattern charts and which has been drawn based on results of air-water mixtures. The transition lines from bubbly to slug (line B) and from churn to annular (J) qualitatively capture the trend of the transitions, however, they significantly offset along the superficial vapour velocity j_v on the abscissa. The transition line from slug to churn flow (H) does not represent the transition of the CO₂ data at all.

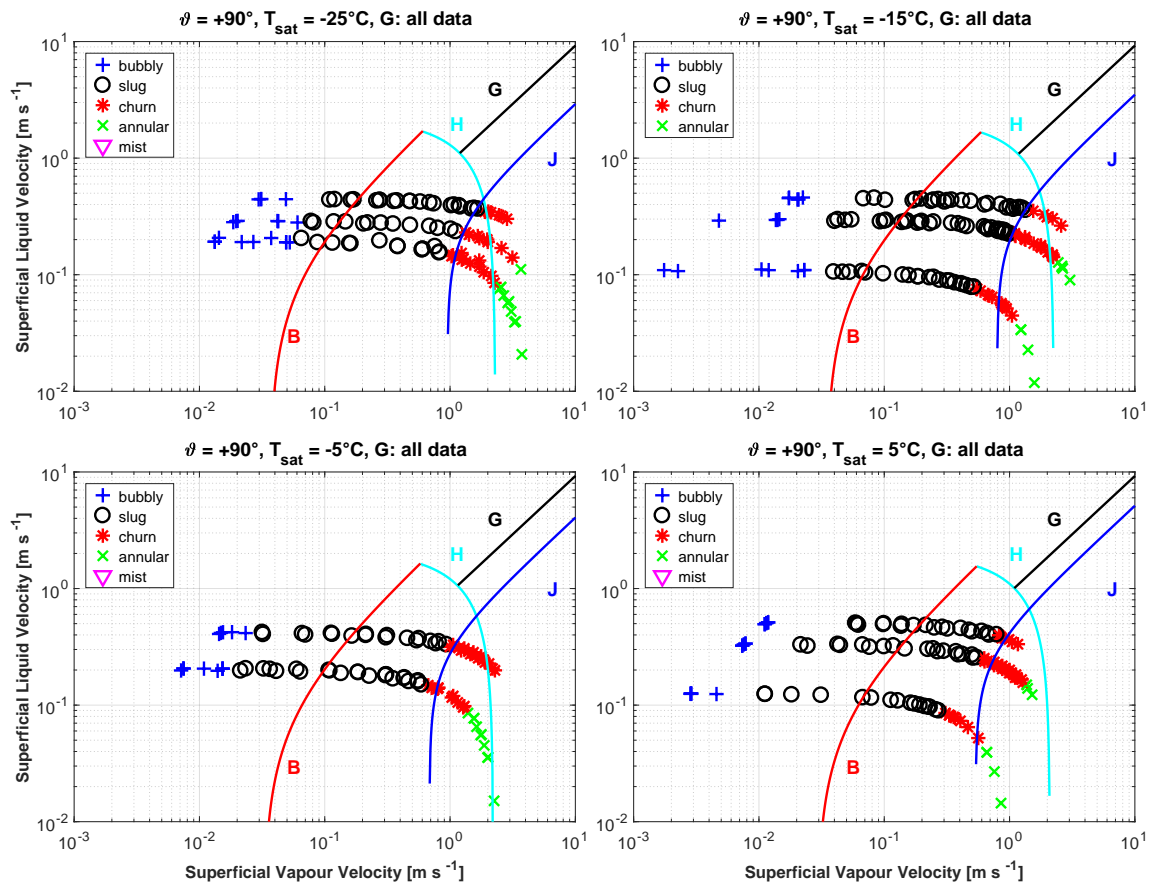


Figure 3.6 – Flow regime observations of CO₂ two-phase flow in vertical upward direction (markers) compared to the flow pattern map of Barnea [51] (lines). Curve B represents the transition from bubbly to slug, curve H the transition from slug to churn and curve J the transition from churn to annular flow. Line G gives the transition to dispersed bubble flow. The transition lines were plotted based on the experimental conditions of the experiments.

Some more studies are compared to the present CO₂ data in Figure 3.7. The bubbly-to-slug transition lines of Taitel et al. [50], Weisman and Kang [86] and Mukherjee and Brill [87] show similar trends to curve B of the Barnea [51] chart in Figure 3.6 and are off the CO₂

data. The slug-to-churn transition boundaries from Taitel et al. [50] and McQuillan and Whalley [56],[88] are not applicable for CO₂ at all. Only the theoretically derived slug-to-churn transition line from Chen and Brill [89] qualitatively represents the trend, however, not in a satisfactory manner. For the churn-to-annular transition, none of these studies describes the change in flow regime properly. In general, as illustrated in Figure 3.7, neither the theoretical studies of Taitel et al. [50] (validated with water-air mixtures), McQuillan and Whalley [56] (air-water, steam-water, R11, R12, R113) and Chen and Brill [89] (air-water), nor the empirical approaches by Weisman and Kang [86] (air-water, air-glycerol, R113) and Mukherjee and Brill [87] (kerosene-air, oil-air) are able to predict the transitions of the present CO₂ data properly.

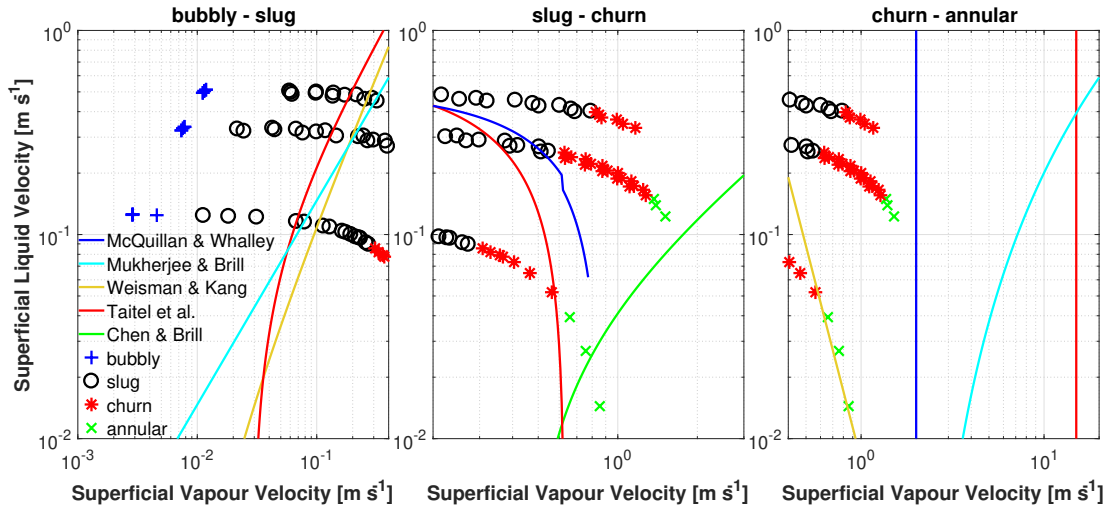


Figure 3.7 – CO₂ flow pattern observations at $T_{sat} = +5\text{ }^{\circ}\text{C}$ compared to transition lines of Taitel et al. [50], Weisman & Kang [86], McQuillan & Whalley [56], Mukherjee & Brill [87] and Chen & Brill [89]. The coordinates represent the superficial liquid (j_L) and vapour (j_V) velocities.

Many of the previously mentioned studies on flow pattern transitions in vertical direction represent their charts using the superficial phase velocities as coordinates. The superficial phase velocities are defined as the volumetric flow rates of the phases in respect to the cross-sectional area of the channel. In mixtures, the volumetric flow rates of the respective gas and liquid phases are independent and can be measured and varied individually just before blending. Contrary to this, the volumetric flow rates of the phases in saturated single-component flows are co-dependent and the superficial velocities of a boiling fluid are functions of the phase densities. Apart from some exceptions, the vast majority of vertical flow pattern maps mentioned in literature have been validated with flow pattern data of two-component mixtures only. For that reason it is not surprising that none of the known correlations predicts the flow pattern data of pure CO₂ boiling flows properly. An alternative approach for illustrating flow regime transitions are charts using vapour quality and mass velocities as coordinates. Such flow pattern maps can be mainly found in studies of horizontal two-phase flows [46],[44],[70],[72] and are useful in particular for designing evaporators. The abscissa usually represents the vapour quality, therefore the flow patterns at different locations inside an evaporator can be deduced easily from this kind of diagram.

3.6 Development of a new Flow Pattern Map for vertical two-phase Flow of CO₂

Flow patterns arise as a consequence of a force balance acting on the co-current phases and are influenced by the fluid properties (saturation temperature/pressure), the flow inertia (mass velocity), vapour quality and the geometry of the duct (angle of inclination, diameter, etc...) [90]. To incorporate the forces acting on the vapour and liquid phases, the transition lines for vertical up- and downflow can be expressed as functions of non-dimensional numbers

$$x_{tr} = f(G, T_{sat}, d) = f(Re, We, Fr) \quad (3.1)$$

where x_{tr} represents the vapour quality where the flow regime transition is happening.

The relative influence of inertia and buoyancy are described by the Froude number. In particular at low mass velocities, the inclination of the pipe affects the two-phase flow when the influence of gravitational forces becomes remarkable. This results in low Froude numbers. At high Froude numbers, the inertia is dominant over the gravitational forces and the tube inclination has less influence on the flow patterns [91]. The effects of inertia are incorporated by the Reynolds- and Weber numbers representing the ratios of inertia to viscosity (μ) and surface tension (σ) respectively. The Reynolds number determines whether the flow is laminar or turbulent. Small Reynolds numbers indicate laminar flow, where the inertia forces are irrelevant compared to the viscous forces and disturbances are dissipated [92]. The Weber number provides information about the formation of the liquid/vapour interface. At small Weber numbers the surface tension dominates over inertia what results in smooth interfaces. On the other hand, high Weber numbers indicate high flow inertia and the turbulence perturbs the interface. Furthermore, the density ratio ρ_r is taken into account as well. To simplify the equations, the non-dimensional numbers are considered for all-liquid and all-vapour flow respectively. Equations 3.2-3.8 represent the non-dimensional numbers considered for the development of the transition correlations and Table 3.2 shows their minimum, maximum and mean values of the experimental domain of this study.

$$Fr_{lo} = \frac{G}{\rho_l \sqrt{gd}} \quad (3.2)$$

$$Fr_{vo} = \frac{G}{\rho_v \sqrt{gd}} \quad (3.3)$$

$$Re_{lo} = \frac{G \cdot d}{\mu_l} \quad (3.4)$$

$$Re_{vo} = \frac{G \cdot d}{\mu_v} \quad (3.5)$$

$$We_{lo} = \frac{G^2 \cdot d}{\rho_l \cdot \sigma} \quad (3.6)$$

$$We_{vo} = \frac{G^2 \cdot d}{\rho_v \cdot \sigma} \quad (3.7)$$

$$\rho_r = \frac{\rho_v}{\rho_l} \quad (3.8)$$

Table 3.2 – Range of non-dimensional numbers of the test campaign

non-dim. No.	min value	mean value	max value
Fr_{lo}	0.3386	1.0038	1.7927
Fr_{vo}	3.11	14.38	36.61
Re_{lo}	5289	18900	39640
Re_{vo}	52082	158344	281674
We_{lo}	8.06	120.26	502.85
We_{vo}	176	1567	3931
ρ_r	0.0416	0.0767	0.1279

The equations describing the flow regime transitions are modelled as a product of non-dimensional numbers, taking the following form:

$$x_{tr} = a_0 \prod_{i=1}^N D_i^{a_i} \quad (3.9)$$

where D_i represents the non-dimensional number, a_0 is a constant, $a_1 \dots a_N$ are the corresponding exponents and N corresponds to the amount of non-dimensional numbers used in the respective equation. In order to find the combination and hence the forces that describe the flow regime transition best, all possible combinations of the non-dimensional numbers mentioned in Eq. 3.2-3.8 are investigated for each flow regime transition. For $n = 7$, what corresponds to the amount of non-dimensional numbers considered (Eq. 3.2-3.8), this results in 127 factorial combinations possible.

The constant a_0 and the exponents $a_1 \dots a_N$ of Eq. 3.9 are determined with an optimization algorithm, based on an unconstrained multidimensional nonlinear minimization method,

carried out in MATLAB. The root mean square error (RMSE) according to

$$RMSE = \sqrt{\frac{1}{k} \sum_{j=1}^k (x_{j,exp} - x_{j,pred})^2} \quad (3.10)$$

is chosen as the target value to be minimized, where x_{exp} is the experimental vapour quality at which the change in flow regime is detected, x_{pred} is the predicted transition vapour quality (according to Eq. 3.9) and k represents the number of data points available. The experimental transition data x_{exp} is defined as the equidistant value between the extreme data points of two consecutive flow regimes. The final equations for the bubbly-to-slug, slug-to-churn and churn-to-annular flow regime transitions are chosen based on solutions with both low RMSE and low exponents ($a_1 \dots a_N < |5|$). Equations 3.11-3.16 represent the transition lines for the three flow regime transitions and Table 3.3 provides their statistics.

The bubbly-to-slug transition in both vertical upward and downward directions is well described by the combination of the all-vapour Froude, the all-liquid Reynolds and the all-vapour Weber number. The combination of the all-liquid Froude number, the all-liquid and all-vapour Reynolds numbers, the all-vapour Weber number and the density ratio gives best results for the slug-to-churn transition for both vertical up- and downflow. Furthermore, the data fit reveals that the set of non-dimensional numbers used to describe the slug-to-churn transition is also an excellent candidate for the churn-to-annular transition providing the lowest RMSE in both up- and downward direction. It can be noticed that each flow regime transition is well described by the same set of non-dimensional numbers for both vertical upflow and downflow respectively.

Bubbly-to-slug transition in vertical upward direction:

$$x_{bs,up} = 17.614 \cdot Fr_{vo}^{0.423} \cdot Re_{lo}^{-0.772} \cdot We_{vo}^{-0.176} \quad (3.11)$$

Bubbly-to-slug transition in vertical downward direction:

$$x_{bs,down} = 1.3 \cdot 10^{-7} \cdot Fr_{vo}^{1.933} \cdot Re_{lo}^{0.102} \cdot We_{vo}^{0.227} \quad (3.12)$$

Slug-to-churn transition in vertical upward direction:

$$x_{sc,up} = 2.225 \cdot Fr_{lo}^{0.973} \cdot Re_{lo}^{-1.266} \cdot Re_{vo}^{1.463} \cdot We_{vo}^{-0.721} \cdot \rho_r^{0.809} \quad (3.13)$$

Slug-to-churn transition in vertical downward direction:

$$x_{sc,down} = 2.604 \cdot Fr_{lo}^{1.068} \cdot Re_{lo}^{-2.299} \cdot Re_{vo}^{1.435} \cdot We_{vo}^{0.588} \cdot \rho_r^{0.923} \quad (3.14)$$

Churn-to-Annular transition in vertical upward direction:

$$x_{ca,up} = 2.445 \cdot Fr_{lo}^{-0.342} \cdot Re_{lo}^{-0.836} \cdot Re_{vo}^{0.525} \cdot We_{vo}^{0.244} \cdot \rho_r^{0.509} \quad (3.15)$$

Churn-to-Annular transition in vertical downward direction:

$$x_{ca,down} = 4.108 \cdot Fr_{lo}^{-2.902} \cdot Re_{lo}^{-4.077} \cdot Re_{vo}^{2.296} \cdot We_{vo}^{2.463} \cdot \rho_r^{2.745} \quad (3.16)$$

Table 3.3 – Statistics of the identified transition equations

Transition	Direction	Eq.	relevant non-dim. No.	# Data	RMSE [%]
Bubbly-Slug	Up	3.11	$Fr_{vo} Re_{lo} We_{vo}$	11	0.1476
	Down	3.12	$Fr_{vo} Re_{lo} We_{vo}$	5	0.1827
Slug-Churn	Up	3.13	$Fr_{lo} Re_{lo} Re_{vo} We_{vo} \rho_r$	11	0.8155
	Down	3.14	$Fr_{lo} Re_{lo} Re_{vo} We_{vo} \rho_r$	8	1.2329
Churn-Annular	Up	3.15	$Fr_{lo} Re_{lo} Re_{vo} We_{vo} \rho_r$	7	1.3916
	Down	3.16	$Fr_{lo} Re_{lo} Re_{vo} We_{vo} \rho_r$	4	$7.5 \cdot 10^{-5}$

The transition lines and the entire database of flow pattern observations recorded within this study are illustrated in Figure 3.8 and Figure 3.9 for the entire temperature range of the experimental domain ($-25^\circ\text{C} \leq T_{\text{sat}} \leq +5^\circ\text{C}$). Figure 3.10 shows detailed views to the bubbly-to-slug transition. In general, it seems more appropriate to identify transition zones instead of transition lines. The changes from one flow regime to another do usually not happen abruptly, it is rather a continuous phenomenon, in particular at the transition from churn to annular, where the transition criteria are rather vaguely defined. The transition zones illustrated in Figure 3.8 and Figure 3.9 are determined with data regressions through the first and last data points of the flow regimes by using the basic structures of non-dimensional numbers according to Eq. 3.11-3.16.

In both vertical up- and downward direction the flow regime transitions show a strong correlation between mass velocity and vapour quality. In upward direction, all three flow regime transitions investigated in this study (bubbly-to-slug, slug-to-churn, churn-to-annular) are occurring at increasing vapour qualities when the mass velocity is decreasing. This effect is well incorporated in the upflow transition equations (Eq. 3.11; 3.13; 3.15) by an aggregate exponent of mass velocity smaller than zero. In general, this trend is in agreement with the shape of the transition lines presented by Bennett et al. [49] that are based on steam-water observations in vertical upward direction. The data of vertical downflow suggests an inverse behaviour compared to the upflow data, i.e. the transition vapour qualities increase with increasing mass velocity. This corroborates with an overall exponent of mass velocity > 0 in

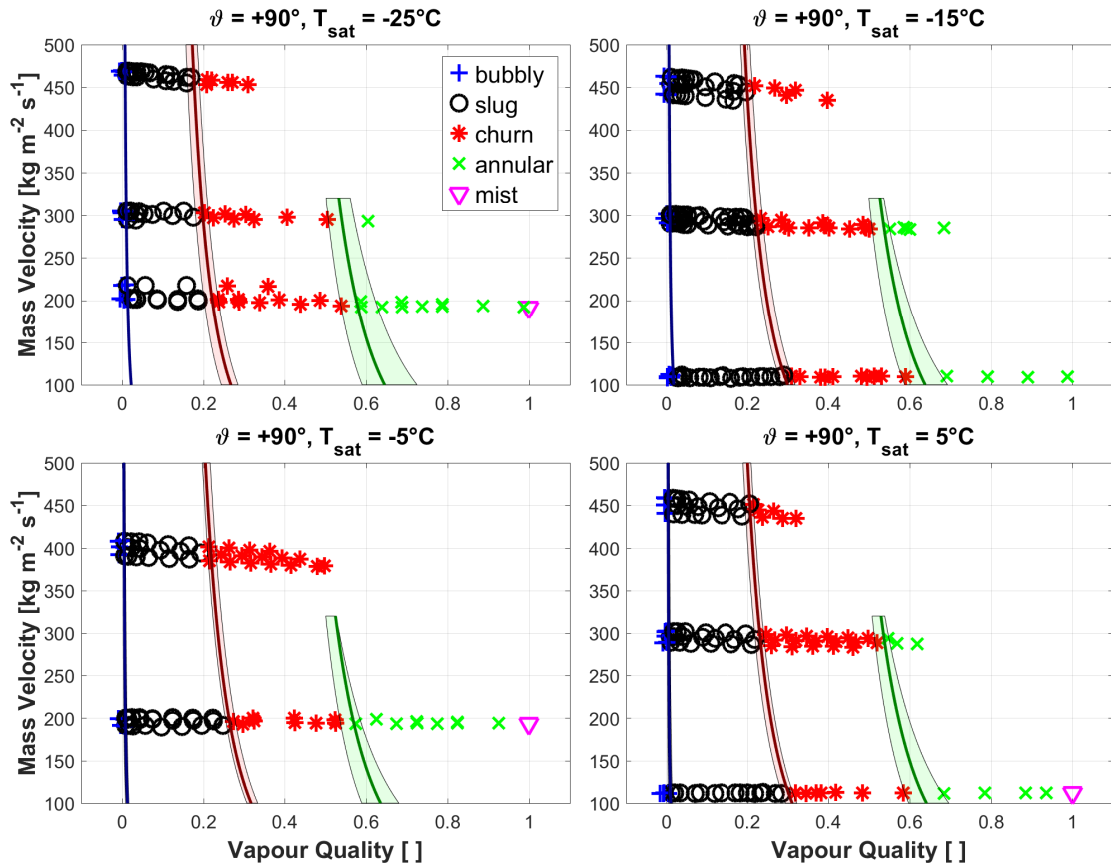


Figure 3.8 – Identified flow pattern map for vertical upflow of CO₂ in comparison to the test data. The transition zones are determined with data regressions through the first and last data points of the flow regimes.

the transition equations for downflow (Eq. 3.12; 3.14; 3.16).

The influence of mass velocity in vertical upflow is illustrated in Figure 3.11 with frames of bubbly and slug flow, that show an increase in mass velocity, while the vapour quality stays (almost) constant. At low mass velocities, it can be noticed that the flow consists of finely dispersed bubbles varying in size and rising upward on a vertical trajectory, mainly due to buoyancy. On the other hand, the flow is getting more turbulent as mass velocity increases. As a consequence, the bubbles are whirled around inside the tube and an increasing coalescence of the bubbles can be noticed due to the zigzag motion in upward direction. This results in increasing bubble sizes and small bubbles tend to disappear. Hence, in vertical upward direction, bubbly flow persists up to higher vapour qualities at low flow rates, where the flow becomes less turbulent or even laminar and the motion of the bubbles is mainly dominated by the buoyancy forces only.

In downward direction, the regimes of bubbly and slug flow tend to disappear at low mass velocities and the flow immediately turns into churn or annular flow, what is illustrated in Figure 3.12. In this case – like in upflow – the inertia of the liquid is becoming negligible and the

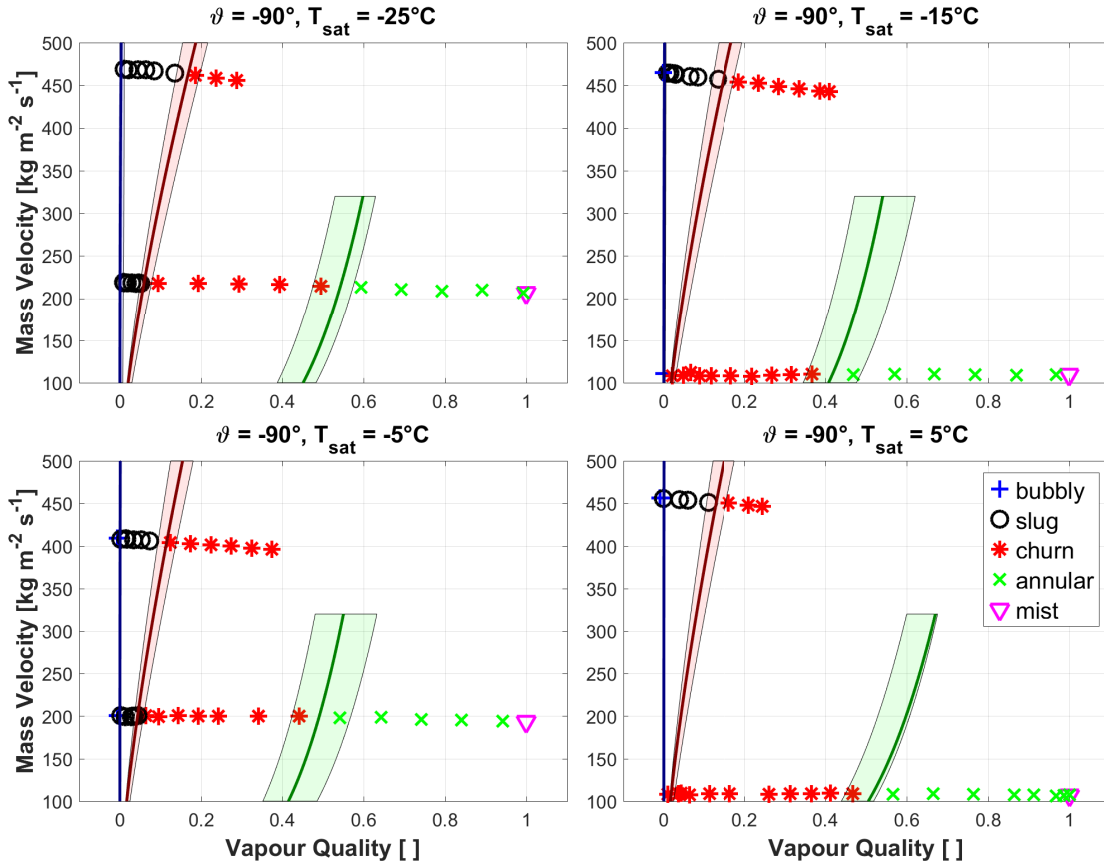


Figure 3.9 – Identified flow pattern map for vertical downflow of CO₂ in comparison to the test data. The transition zones are determined with data regressions through the first and last data points of the flow regimes.

buoyancy effects are again getting dominant as flow rates are decreasing. As a consequence, phase separation due to buoyancy is happening at low flow rates and the hydrostatic liquid column tends to disappear in the downflow channel. In general, it is observed that the flow regime transitions in upward and downward direction show mirrored trends what can be corroborated by the change from co- to counter-current buoyancy forces.

Moreover, it can be noticed that the bubbly-to-slug and the slug-to-churn transition in upflow show a trend in regard of saturation temperature. According to Figure 3.10, the bubbly-to-slug transition in upward direction is happening at higher vapour qualities when decreasing the temperature. This is well captured by Eq. 3.11, since the vapour density is decreasing and both liquid viscosity and surface tension are increasing at low temperatures. Contrary to this, no bubbly flow can be observed at low temperatures in downward direction, which corroborates observations made in [93]. According to Figure 3.8, the slug-to-churn transition vapour quality increases with increasing saturation temperature. This might be linked to the decreasing liquid viscosity that allows slug formation even at higher vapour qualities. It is recommended to consolidate this hypothesis with additional studies over a bigger range of

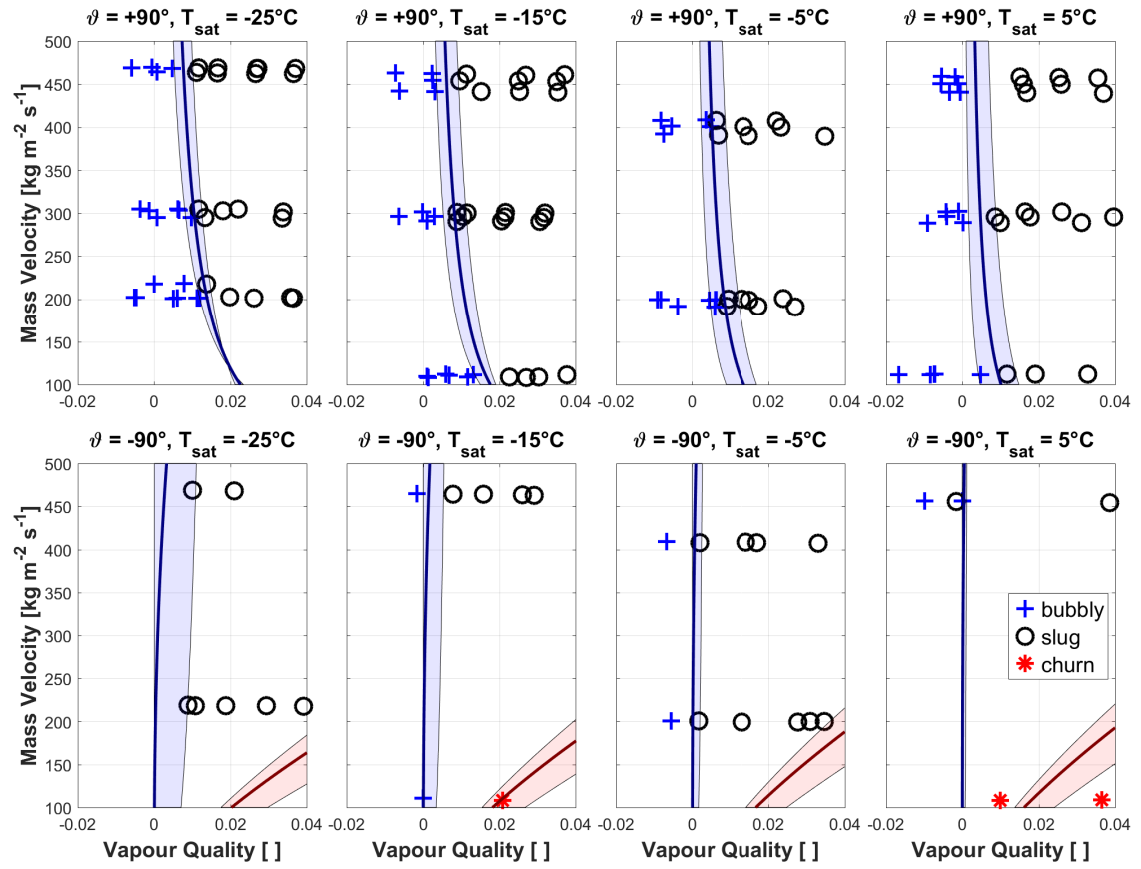


Figure 3.10 – Detailed view of the bubbly-to-slug flow regime transition in both upward ($\vartheta = +90^\circ$) and downward ($\vartheta = -90^\circ$) direction: transition lines with temperature dependent transition zones.

viscosities, e.g. by means of an increased range of saturation temperature or different working fluids. All the other transition lines do not show a clear correlation with temperature, what might be due to the limited amount of data points available.

3.7 Conclusion

Two-phase flow patterns of vertical up- and downflow of CO_2 are visualized in a dedicated test facility and flow patterns are recorded with a high-speed camera. A database of 431 flow pattern observations in upward and 123 in downward direction is set up and the records are analysed with machine learning techniques, that automatically identify the flow pattern transitions. It is observed that none of the existing flow pattern maps for vertical directions in the literature is able to describe the flow pattern transitions observed within the present study properly. In general it is questionable whether flow pattern maps elaborated with the data of mixtures are able to properly predict the flow pattern transitions of saturated single-component fluids. For that reason, the results of the present study are condensed into novel

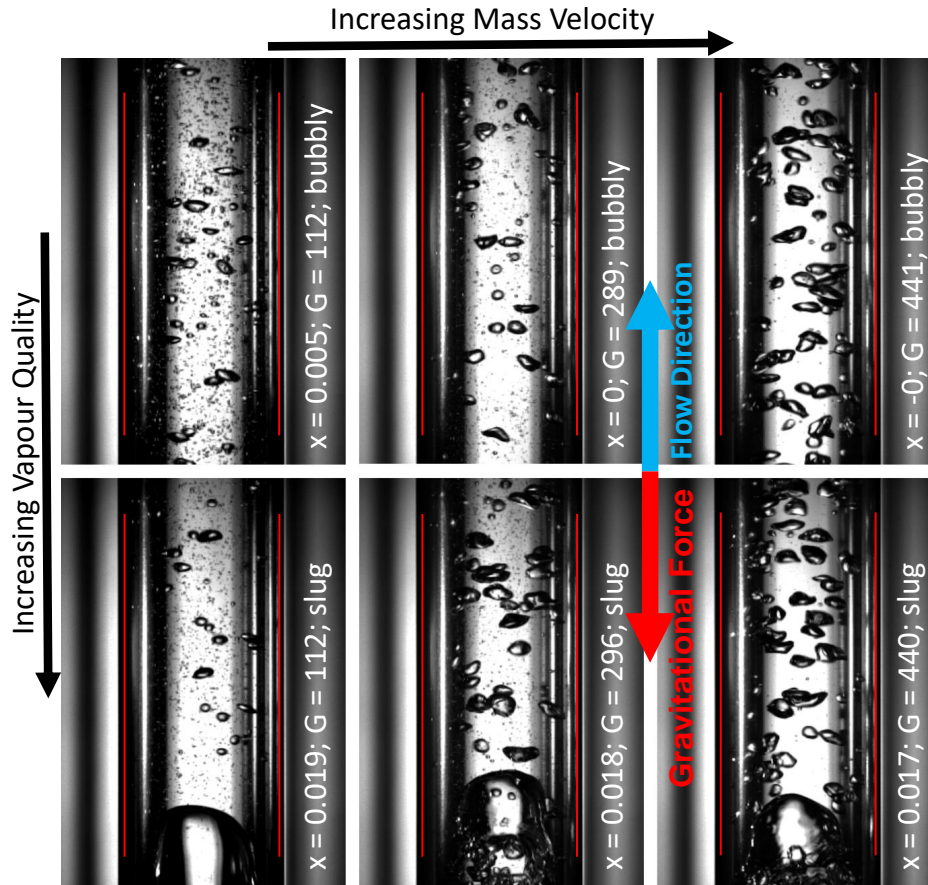


Figure 3.11 – Influence of mass velocity illustrated with observations of bubbly flow (top row) and slug flow (bottom row) of CO₂ in vertical upward direction ($\vartheta = +90^\circ$) at $T_{sat} = +5^\circ\text{C}$. Mass velocity increases from left to right, while vapour quality stays (almost) constant. Finely dispersed bubbles that move upward on a vertical trajectory can be observed at low flow rates. At increased mass velocities, the flow gets turbulent and an increasing coalescence of the bubbles can be noticed.

flow pattern maps for vertical up- and downflow of CO₂ two-phase flow. It is observed, that the changes in flow regime are strongly dependent on vapour quality, mass velocity, the flow direction and the fluid properties. The transition lines in upward and downward direction show opposed trends. This can be mainly substantiated with the changes from co- to counter-current buoyancy forces.

This work provides a baseline for further investigations on the modelling of two-phase flows of CO₂ in vertical direction and expands the existing flow pattern prediction methods for horizontal two-phase flow of CO₂ [72],[74] to vertical upward and downward directions. For both vertical channel orientations, the flow patterns of bubbly, slug, churn, annular and mist/vapour flow can be observed. However, some differences to horizontal configurations

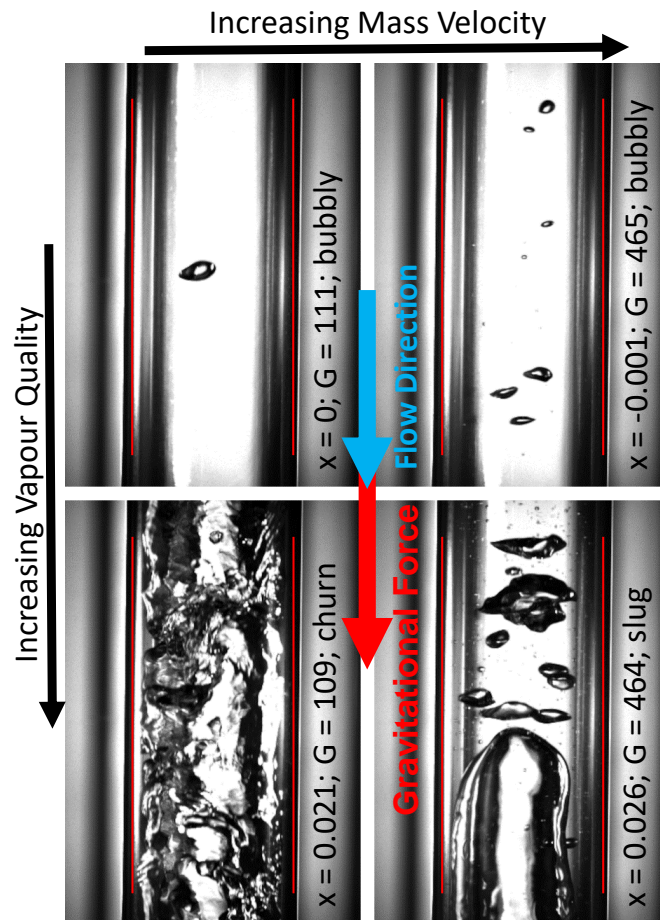


Figure 3.12 – Influence of mass velocity illustrated with observations of CO_2 in vertical downward direction ($\vartheta = -90^\circ$) at $T_{sat} = -15^\circ\text{C}$. Mass velocity increases from left to right, while vapour quality stays (almost) constant. Bubbly flow (top row) immediately turns into churn flow at low mass velocities (bottom left), whereas bubbly flow converts to slug flow at increased flow rates (bottom right).

from literature have been noticed that are illustrated in Figure 3.13. In vertical directions, flow stratification, where the co-current phases are clearly separated due to the influence of gravity, is not happening. For the same reason, a dryout region where the liquid film partly disappears, does not occur and the liquid film at the tube walls is drying out symmetrically at vapour qualities just below $x = 1$. Entrained droplets can persist beyond that in the superheated vapour phase.

The lack of other comparable data of vertical two-phase flow of CO_2 in literature can be a motivation for further experimental studies to verify the presented flow pattern maps. Furthermore, there is the potential to extend the range of validity by investigating beyond the test conditions of the present work in terms of mass velocity, saturation temperature, channel

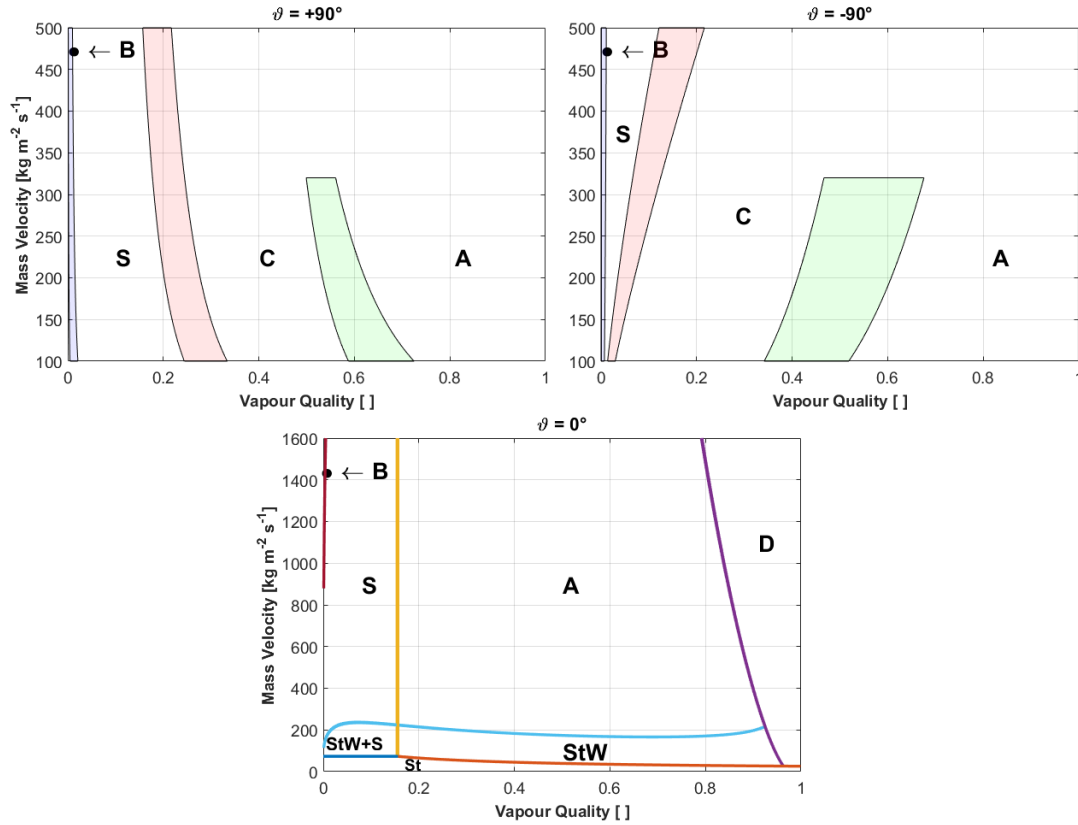


Figure 3.13 – Flow pattern maps for vertical upward (top left) and downward (top right) direction of CO₂ elaborated within this study in combination with the horizontal flow pattern map of Cheng et al. [72] (bottom). The novel transition zones in the vertical up- and downflow maps are applicable for saturation temperatures $-25^\circ\text{C} \leq T_{\text{sat}} \leq +5^\circ\text{C}$. B: bubbly, S: slug, C: churn, A: annular, D: dryout, St: stratified, StW: stratified-wavy.

size and shape, as well as inclination angle. For the thermal management of future High Energy Physics experiments it is of particular interest to explore the two-phase flow behaviour of CO₂ at temperatures below -30°C , as well as investigating different channel sizes and geometries. Concentric, vertical transfer lines require further studies in concentric annuli and for the design of vertical evaporators, it would be beneficial to analyse the differences to mini- and micro-channels, where capillary forces are becoming significant. It is also recommended to extend the ranges of viscosities and densities in future studies to intensify the examination of the dependency of flow pattern transitions on these fluid properties.

4 Pressure Drop

Pressure drop is one of the key factors that has to be given major attention throughout the design phase of cooling loops. The pressure losses of CO₂ two-phase flows are investigated within this chapter. The content and the results presented in the following have been published by the following journal:

- D. Schmid, B. Verlaet, P. Petagna, J. Schiffmann and R. Revellin. "Adiabatic two-phase pressure drop of carbon dioxide in different channel orientations", *International Journal of Heat and Fluid Flow*, 2022. doi.org/10.1016/j.ijheatfluidflow.2022.108966

Pressure drop is defined as the difference between the pressures at the channel inlet and outlet [77]. In the analysis of pressure gradients in channels where $l \gg d$, it is commonly accepted to treat this as a one-dimensional problem in axial direction, where the cross-sectional pressure distribution is assumed to be constant and radial pressure gradients are neglected. In general, two-phase pressure drops are composed of a frictional, a hydrostatic and an accelerational component and are determined by integrating the pressure gradients presented in Equation 4.1.

$$\left(-\frac{dp}{dz}\right)_t = \left(\frac{dp}{dz}\right)_{fr} + \left(\frac{dp}{dz}\right)_{st} + \left(\frac{dp}{dz}\right)_{ac} \quad (4.1)$$

The accelerational pressure drop reflects the change in kinetic energy of the flow and is calculated based on the differences between the inlet and outlet conditions of a defined volume according to Equation 4.2 [76]

$$\left(\frac{dp}{dz}\right)_{ac} = \frac{G^2}{l} \left\{ \left[\frac{(1-x)^2}{\rho_l(1-\varepsilon)} + \frac{x^2}{\rho_v\varepsilon} \right]_{out} - \left[\frac{(1-x)^2}{\rho_l(1-\varepsilon)} + \frac{x^2}{\rho_v\varepsilon} \right]_{in} \right\} \quad (4.2)$$

where x is the vapour quality, ε is the void fraction, G is the mass velocity and ρ_l, ρ_v are the respective phase densities. The calculation of the hydrostatic pressure drop component due

to static head is determined according to Equation 4.3, which corresponds to the standard approach reported in the literature [76],[77].

$$\left(\frac{dp}{dz}\right)_{st} = \rho_{2p} g \sin \vartheta \quad (4.3)$$

Equation 4.3 is strongly dependent on the two-phase density ρ_{2p} . Ghajar and Bhagwat [94] compared the vapour quality based two-phase density model (Eq. 4.4) – derived from the energy conservation equation – and the void fraction based two-phase density model (Eq. 4.5) – derived from the momentum conservation equation – to measurements conducted in their laboratory and concluded that the vapour quality approach underpredicts the two-phase density at high vapour qualities due to the fact that the velocity slip-ratio of the phases is neglected. As a consequence, the two-phase density calculation based on void fraction defined in Equation 4.5 is used for determining the static head in this work.

$$\rho_{2p} = \left(\frac{x}{\rho_v} + \frac{1-x}{\rho_l} \right)^{-1} \quad (4.4)$$

$$\rho_{2p} = \rho_v \varepsilon + \rho_l (1 - \varepsilon) \quad (4.5)$$

4.1 Literature Review

4.1.1 Frictional pressure drop models

A significant number of successful pressure drop models for two-phase flows have been proposed over the last decades, that are applicable for various fluids and mixtures over a wide range of operating parameters. An extensive literature review has been carried out by Kim and Mudawar [95] by setting up a database of 7115 frictional pressure drop results from 36 sources and by comparing it to the well-established correlations by Lockhart and Martinelli [96], Friedel [97], Müller-Steinhagen and Heck [98], Jung and Radermacher [99] and Wang et al. [100] in the macro-scale domain. The universal model by Müller-Steinhagen and Heck [98] showed the best results, followed by the model by Sun and Mishima [101], that was build upon the model for vertical pressure drops of Mishima and Hibiki [102] and has been validated with data of CO₂.

Another comprehensive review specifically for CO₂ has been conducted by Thome and Ribatski [68], where they compared 325 horizontal pressure drop measurements of two-phase CO₂ from Bredesen et al. [103] to the leading frictional pressure drop correlations from the literature. Within that study, the correlation of Friedel [97] gives the best results, followed by the model of Müller-Steinhagen and Heck [98].

Cheng et al. [72] compiled a database of horizontal pressure drop measurements of CO₂

two-phase flows from literature and compared the data to empirical pressure drop correlations by Chisholm [104],[105], Friedel [97], Grønnerud [106], Müller-Steinhagen and Heck [98], a modified Chisholm correlation by Yoon et al. [107] and to the flow pattern based correlations of Moreno Quibén and Thome [108],[109],[110]. None of the existing studies was able to predict the data satisfactorily. Thus, a new flow pattern based phenomenological pressure drop model for a wide range of horizontal flow conditions has been presented. This model has recently been validated with an extended database [74]. To conclude, the number of pressure drop measurements and investigations of horizontal two-phase flow of CO₂ has been constantly increasing within the recent years. However, no experimental data of vertical two-phase flows of CO₂ is currently available in the literature.

Hellenschmidt and Petagna [111] investigated horizontal two-phase flow of CO₂ in the transition zone from macro- to microchannels and stressed the influences of the flow conditions, in particular the impact of the saturation temperature, on pressure drops. They suggest to subdivide the analysis according to the saturation temperatures and tube diameters and observed that the homogeneous model performs best in the temperature range from +15 °C to –5 °C, while the Friedel [97] model provides best results below –5 °C in circular channels of 2.15 mm, what can still be attributed to the macro-scale domain, approaching the threshold to micro-channels.

4.1.2 Void fraction correlations

The cross-sectional void fraction – referred to as void fraction due to simplicity – is the crucial part in determining the pressure losses according to the static head in non-horizontal flows. Vijayan et al. [112] classified void fraction models into four groups: (i) the velocity-ratio (or slip-ratio) models, (ii) the drift-flux models, (iii) the $k\epsilon_h$ models and (iv) the group of empirical-miscellaneous correlations that do not fit any of the previously mentioned categories. The velocity-ratio concept is based on the assumption that the concurrent phases travel at different mean velocities. Butterworth [113] compared several velocity-ratio models [96],[114],[115],[116],[117] and concluded that – due to their similarities – they can be expressed with a basic void fraction correlation by using individual sets of factors and exponents. The drift-flux model takes into account the cross-sectional distribution profile of the void fraction inside the channel, as well as the superficial velocities of the gas and liquid phases. The first drift-flux model dates back to Zuber and Findlay [118] and to the contributions of Wallis [119]. Detailed assessment studies of drift-flux models against steam-water data have been carried out by Chexal et al. [120],[121] based on 1500 data points and by Coddington and Macian [122] with a database of 362 individual measurements. The $k\epsilon_h$ method corrects the homogeneous void fraction by an empirically derived correction factor.

Woldesemayat and Ghajar [123] conducted a comprehensive literature review and compared 68 void fraction correlations to an unbiased database, consisting of 2845 void fraction data points of air-water, air-kerosene and natural gas-water in circular pipes with diameters

ranging from 12.7 – 102.26 mm. They concluded that their newly established correlation [123] provides the best results for any kind of pipe inclination when comparing them to the compiled database. For vertical upflow, the correlations of Dix [120],[122], Premoli et al. [124], Rouhani and Axelsson [125] and Morooka [126] show good results when comparing them to the 403 data points available in vertical upward direction. Furthermore, these correlations achieve good results for any pipe inclination. In general, it was found that drift-flux models are an appropriate approach to predict void fractions for two-phase flows. This statement corroborates with data by Godbole et al. [127], who compared 52 void fraction correlations against a void fraction database of 1208 measurements of vertical upward two-phase flows.

Cioncolini and Thome [128] proposed a strongly simplified prediction method for the void fraction of annular flows, that depends on the vapour quality and vapour to liquid density ratio only. This prediction model has been built upon a database of 2633 data points for circular tubes, covering both micro- and macroscale flow conditions with channel diameters from 1.05 – 45.5 mm, vapour qualities from 0 to 1, density ratios from 0.001 – 1, mass velocities from 22 – 3420 kg m⁻² s⁻¹ and pressures from 1.1 – 207 bar. This model suggests no macro- to microscale transition. Due to the good results of their model they claim, that all other parameters that might be relevant in other flow regimes seem to be of minor importance in annular flow conditions.

Ghajar and Bhagwat [94] compared the performances of velocity-ratio and drift-flux models and advocate that drift-flux models better predict void fraction compared to other approaches. The drift-flux correlations of Bhagwat and Ghajar [129], Gomez et al. [130], Hibiki and Ishii [131] and Rouhani and Axelsson [125] show good performance within their work. An additional comprehensive study by Bhagwat and Ghajar [132] compares more void fraction models to an extensive database of 8255 data points and finally presents a flow pattern independent void fraction correlation, that is valid for a large range of pipe diameters (0.5 – 305 mm), pipe orientations ($-90^\circ \leq \theta \leq 130^\circ$), system pressures (0.1 – 18.1 MPa) and fluid properties ($0.0001 \leq \mu_l \leq 0.6$ Pa s).

A huge variety of void fraction correlations has been developed for various applications within the last decades. However, due to the lack of experimental data, non of them has been verified for vertical two-phase flow of CO₂.

4.1.3 Nature of the issue and objective of the present chapter

Pressure drop data of horizontal two-phase flow of CO₂ has been recorded and analyzed within several studies and suitable models for predicting horizontal pressure drops of CO₂ accurately have been identified and elaborated within the recent years. However, the problem of two-phase pressure drops of CO₂ in vertical directions has not been addressed so far, and as a consequence, no model has been developed or validated for this purpose. The objective of the present chapter is the identification of suitable pressure drop prediction models for horizontal and vertical two-phase flows of CO₂.

4.2 The Test Sections and the Database

The experimental setup consists of three consecutive test sections for horizontal, vertical up- and downflow that are made of smooth stainless steel tubes (EN 1.4404) with an inner diameter of 8 mm and have a length of 8 m each. Tests with a stylus instrument at the inner pipe surface of some tube samples reveal a surface roughness of $\sim 1 \mu\text{m}$. The vapour qualities at all three test sections are determined at the inlet. Each test section is equipped with absolute pressure transmitters and RTDs (PT100) at the inlet and outlet respectively. Differential pressure transmitters with ranges of 0.5 and 3 bar measure the pressure losses between the inlet and outlet of the test sections. The test facility, the instrumentation and the operating conditions are explained in detail in chapter 2 and the accuracy of the calibrated instrumentation is provided in Table 2.3.

A database of 512 data points in horizontal and 295 data points for each vertical direction (upflow and downflow respectively) has been compiled within the present work. In total, this results in 1102 pressure drop measurements of two-phase CO_2 available. Figure 5.2 summarizes the database in terms of saturation temperature and mass velocity. Data of thermodynamic non-equilibrium boiling, where tiny bubbles can be observed in the glass tubes even though the caloric properties still indicate subcooling, are excluded.

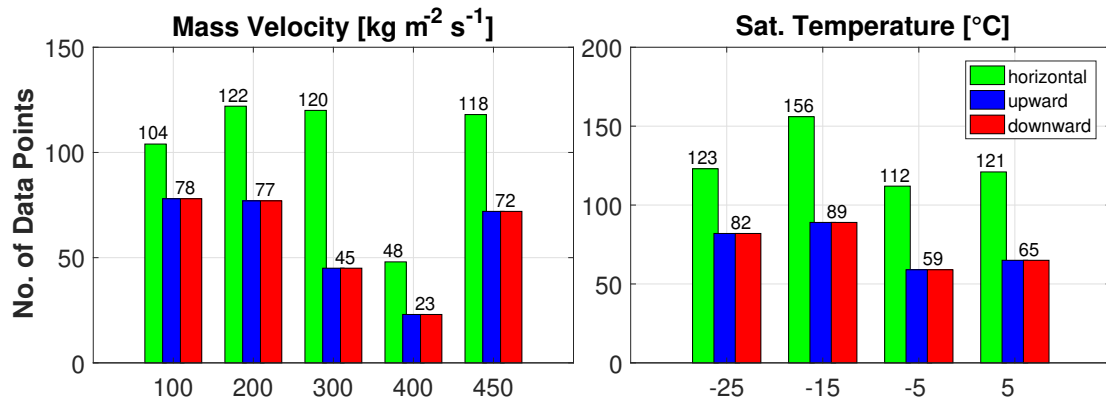


Figure 4.1 – Histograms describing the experimental pressure drop database in terms of mass velocity and saturation temperature.

4.3 Pressure Drop Phenomena and Flow Regimes

Two-phase flow phenomena, such as pressure drop are intrinsically related to the distribution and interface configurations of the concurrent phases. Many studies on the modelling of two-phase flows, like the ones by Ould Didi et al. [133] and Wojtan et al. [44],[45] have demonstrated that flow pattern dependent prediction methods enhance the accuracy significantly. In the present study, flow pattern observations were recorded alternately in vertical upward and downward direction with a digital high-speed camera and have been analyzed with a Flow-Regime-Classifer [85]. The flow regimes of the "blind" experiments in vertical direction –

where no flow pattern observations were recorded and the camera was focused on the opposite direction – have been determined with the flow pattern map correlations presented in Schmid et al. [134]. In horizontal direction, the map of Cheng et al. [72] has been used to identify the flow regimes. Figure 4.2 represents the pressure drop data grouped according to the flow regimes.

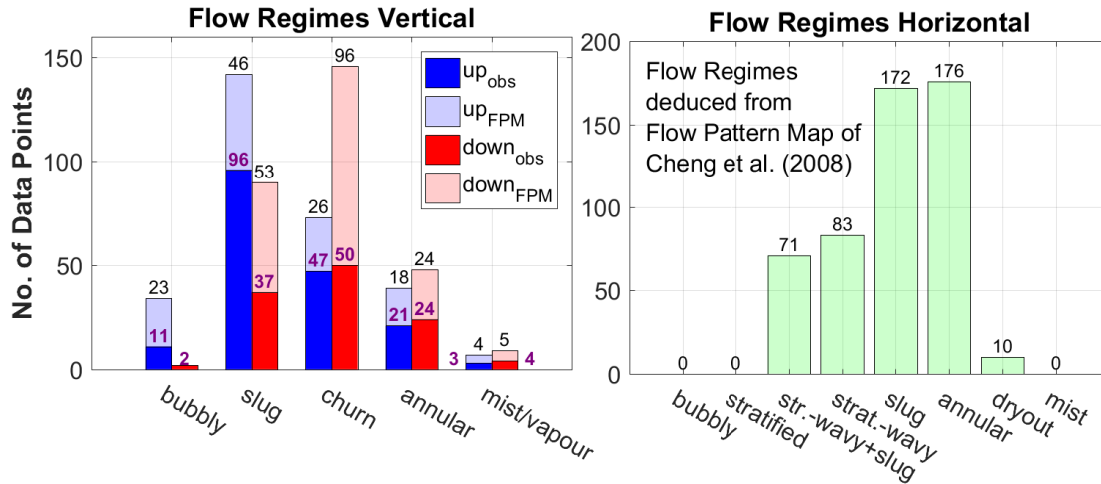


Figure 4.2 – Flow regimes of the pressure drop database recorded within this study. Left: Direct flow pattern observations (illustrated with dark blue and dark red bars) and flow regimes deduced from the flow pattern maps of Schmid et al. [134] (illustrated with light blue and light red bars) in vertical direction. Right: Flow patterns of horizontal data deduced from the flow pattern map of Cheng et al. [72].

One of the key questions in analysing two-phase flow data is, whether the flow regime transitions leave their signature in the pressure drop measurements. Figure 4.3 illustrates the standard deviation ($6\sigma_{STD}$) appearing in the pressure drop signals in horizontal, vertical upward and downward direction. It can be noticed that the magnitudes of the oscillating pressure drop signals are increasing in slug flow and in the transition zones to its neighbouring flow regimes throughout all flow orientations. In slug flow, the increasing pressure fluctuations can be explained by the alternating appearance of liquid slugs and vapour inside the channel. Liquid slugs with a high inertia collapse or collide with the pipe wall, generating pressure waves and therefore non-uniform pressure inside the channels [135]. Furthermore, the vapour phase and the liquid slugs tend to travel at different velocities due to differences in shear forces, friction and density. In the transition zone between flow regimes, the changes of the flow pattern based frictional pressure losses might induce fluctuations as well [136]. In general, any changes in flow velocity induce a change in pressure [137]. These oscillation effects get magnified in vertical direction where buoyancy forces have a significant impact on the amplification of the fluctuating pressure gradients. In particular in downflow direction, where the buoyancy force is opposed to the vector of the flow inertia, the alternation of the liquid and the vapour phase result in increasing pressure fluctuations.

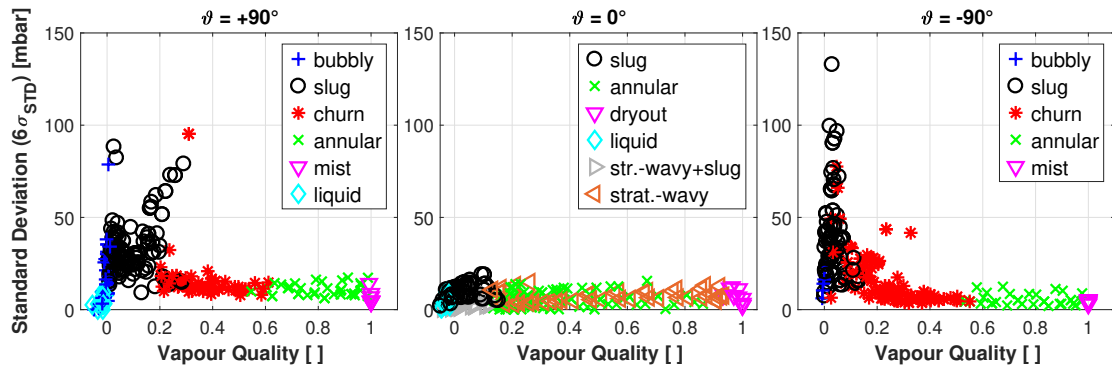


Figure 4.3 – Standard deviation ($6\sigma_{STD}$) of pressure drop oscillations in CO_2 two-phase flow in a stainless steel tube with an inner diameter of 8 mm measured in various flow directions. The plots show the entire data sets available in the present study at various mass velocities and saturation temperatures.

4.4 Pressure Drop Measurements and Influences of Flow Parameters

The pressure drop components mentioned in Eq. 4.1 are greatly affected by the fluid properties (saturation temperature/pressure), the flow inertia (mass velocity), the vapour-to-liquid ratio (vapour quality), the spatial distribution of the concurrent phases (flow patterns), and by the size, geometry and orientation of the channel. The accelerational pressure losses due to the heat pickup from ambient are found to be negligible within the present data sets and the vapour qualities are determined at the inlets of all three test sections. The influences of the saturation temperature, the mass velocity and the vapour quality on the frictional pressure losses of horizontal flow are illustrated in Figure 4.4. Increasing mass velocities result in increased turbulence with higher shear stresses and wall friction. As a consequence, the frictional pressure drops become remarkable at high mass flow rates. In the same context, the phase velocities increase with the vapour qualities, which result in increased frictional losses. This is typically characterized by the peak of the pressure drops in annular flow – just before dryout occurs – where the phase velocities are high. In the dryout region the tube perimeter is only partly wetted, hence partly in direct contact with the vapour phase. The liquid film at the inner tube perimeter disappears entirely towards $x = 1$ and the pressure drop yields to single-phase vapour flow. Moreover, Figure 4.4 also highlights the influence of the saturation temperature on the frictional pressure gradient that increases with decreasing temperatures. Decreasing saturation temperatures result in increasing fluid viscosities and as a consequence, the dissipation of kinetic energy into internal energy increases. In essence, the two-phase flow is less homogeneous at lower saturation temperatures what corroborates with well-established conclusions [111]. The differences of the phase properties with regards of viscosity and density are increasing when lowering the saturation temperature, which affects the velocity profiles of the phases. Lowering the saturation temperature results in an increasing liquid and a decreasing vapour density, thus vapour velocity increases and liquid velocity decreases. As a

consequence, the increasing slip-ratio implies higher losses due to interfacial shear.

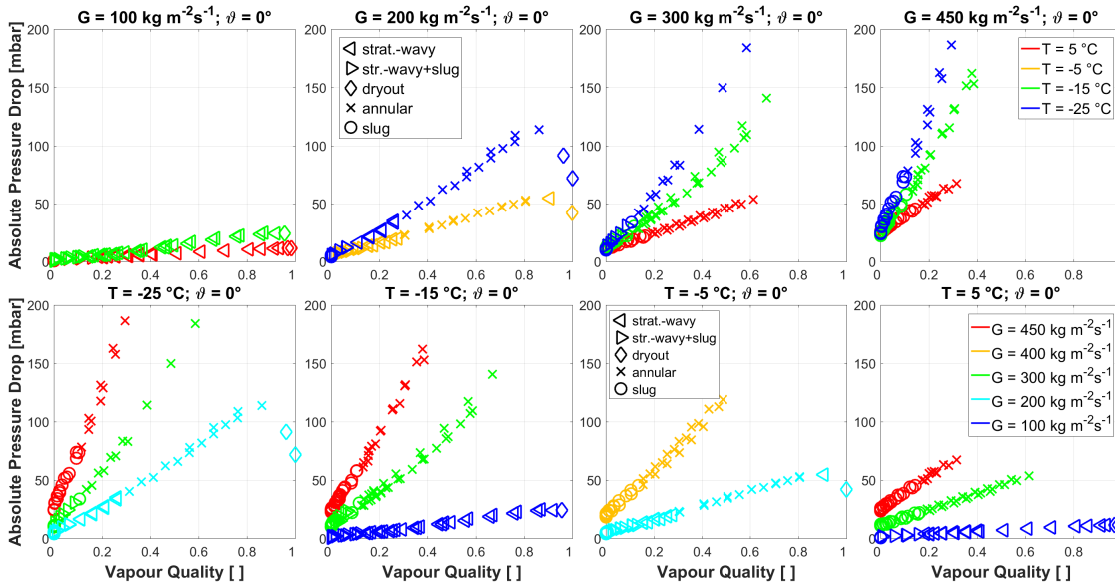


Figure 4.4 – Pressure drops of CO₂ two-phase flow measured at the horizontal test section ($\vartheta = 0^\circ$, $l = 8$ m, $d = 8$ mm) under varying flow parameters, grouped according to the mass velocity (top) and saturation temperature (bottom).

In vertical directions, the static pressure component contributes significantly to the entire pressure drop. Figure 4.5 illustrates the measurements recorded in the vertical upward test section with a length of 8 m. It can be noticed that increasing mass velocities result in increasing pressure drops, what corroborates with the observations made in horizontal flows regarding the increasing frictional losses. Furthermore, increasing saturation temperatures result in higher pressure drops at low vapour qualities in the bubbly, slug and churn flow regimes at $x < 0.2...0.3$. This is in line with the two-phase density according to Eq. 4.4 that increases with increasing temperature. In general, the static component is dominant at low vapour qualities in long vertical pipes. At higher vapour qualities around $x > 0.2...0.3$, the influence of the static head becomes of minor importance and the frictional losses become dominant.

The data points recorded in vertical downward direction illustrated in Figure 4.6 show mirrored trends to the data in vertical upward direction, with a pressure recovery (total pressure drop < 0) at low vapour qualities due to the static pressure component. However, at low mass flow rates the pressure gain gets lost even at very low vapour qualities what is characterized by the steep-increasing slope of the pressure drop measurements. This indicates that the hydrostatic liquid column disappears and phase separation is happening due to the low mass flow rates, which is in agreement with the statements in Schmid et al. [134], where it has been observed that in downward direction annular flow already occurs at very low vapour qualities, while the bubbly, slug and churn flow regimes tend to disappear.

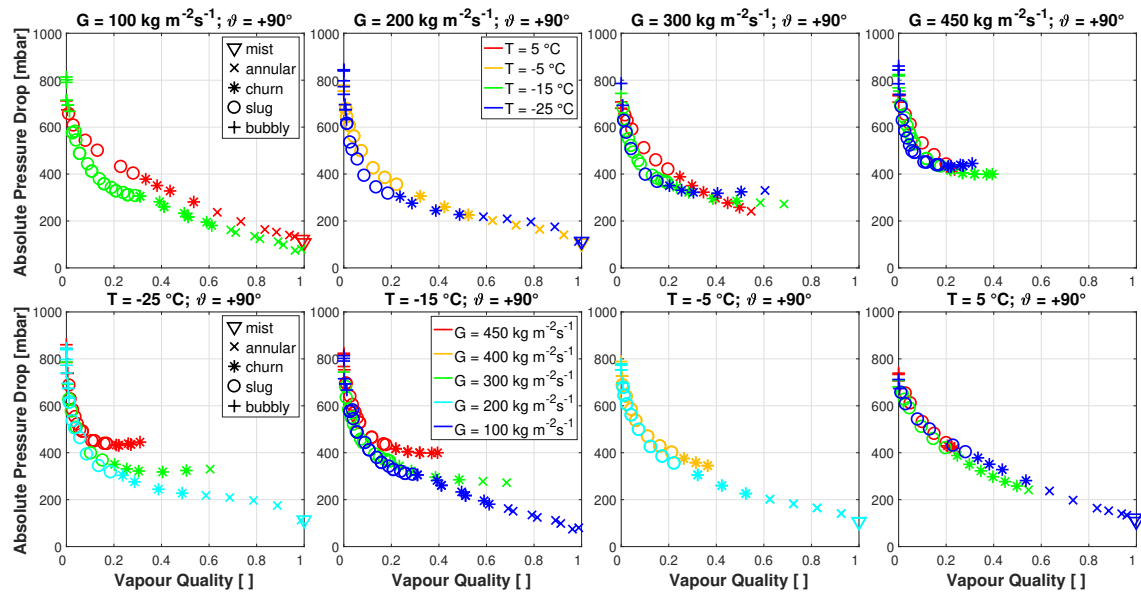


Figure 4.5 – Two-phase pressure drop measurements of CO₂ in vertical upward direction ($\vartheta = +90^\circ$, $l = 8$ m, $d = 8$ mm) under varying flow parameters, grouped according to the mass velocity (top) and saturation temperature (bottom).

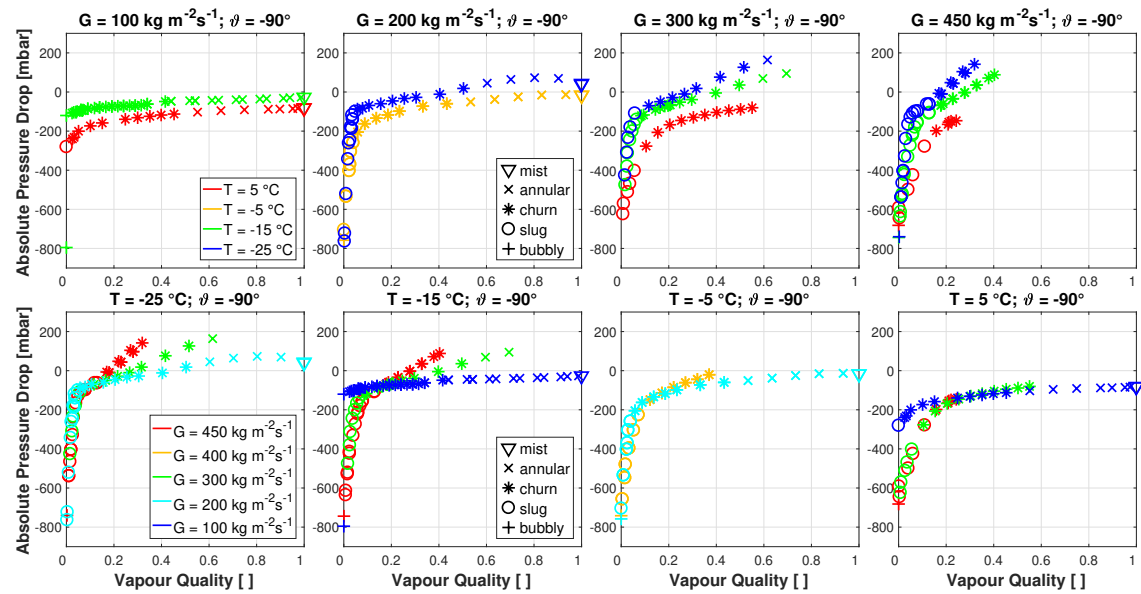


Figure 4.6 – Two-phase pressure drop measurements of CO₂ in vertical downward direction ($\vartheta = -90^\circ$, $l = 8$ m, $d = 8$ mm) under varying flow parameters, grouped according to the mass velocity (top) and saturation temperature (bottom).

4.5 Pressure Drop Measurements compared to Prediction Models

Pressure drop phenomena are quite different in micro- and macroscale channels as pointed out in [74]. Flow confinement is becoming remarkable in reduced channel sizes and as a consequence capillary forces become significant. According to the thresholds provided by Kew and Cornwell [29], Kandlikar [30] and Ong and Thome [31], the data gathered within the present study can be clearly attributed to macrochannels. In the following, the 18 frictional pressure drop correlations summarized in Table 4.1 are considered. The correlations 1) through 6) are declinations of the homogeneous pressure drop model with different two-phase viscosities. The homogeneous frictional pressure drop model assumes the vapour and liquid phases travelling at the same velocities inside the tubes, which is – besides the verified universal two-phase pressure drop correlations – an appropriate assumption to calculate the frictional pressure drop component in macrochannels, in particular at low vapour qualities. Furthermore, the models 13) and 15) are designed for specific flow regimes only. However, for the sake of completeness, these models have been included in the analysis of the entire data set, being aware that the comparison with data of other flow regimes might go beyond their extent of validity.

Table 4.1 – Frictional pressure drop correlations appropriate for macrochannels considered within this study.

No.	Authors	d <i>mm</i>	#	Fluid / Remark
1)	Owens [138]	3		steam-water
2)	McAdams et al. [139]			benzene, water, benzene-water in heated tubes; $\vartheta = 0^\circ$
3)	Cicchitti et al. [140]	5.1	56	steam-water
4)	Davidson et al. [141]	23.4		steam-water
5)	Garcia et al. [142]	23.2 – 140.2	2435	$\vartheta = 0^\circ$; air-water, air-oil, air-kerosene, gas-hydrocarbons, gas-water
6)	Awad & Muzychka II [143]	0.148 – 14		R12, R22, R717, R134a, R410A, argon (R740), propane (R290)
7)	Friedel [97]	0.98 – 257.4	25000	air-water, steam-water, air-oil, methane-water, methane-oil, nitrogen, nitrogen-water, alcohol-argon, argon-water, R11, R12, R22, R113
8)	Lockhart & Martinelli [96]	1.5 – 25.8		adiabatic; air-benzene, air-kerosene, air-water, oils
9)	Baroczy [105] & Chisholm [104]			steam-water
10)	Müller-Steinhagen & Heck [98]	4 – 392	9300	air-water, steam-water, argon, nitrogen, neon, argon-water, air-oil, R11, R12, hydrocarbons, refrigerants
11)	Sun & Mishima [101]	0.506 – 12	2092	air-water, R123, R134a, R22, R236ea, R245fa, R404a, R407c, R410a, R507, CO ₂
12)	Grønnerud [106]	26.2; 33	1000	$\vartheta = 0^\circ$; adiabatic, heated; R12, R717
13)	Bankoff [144]			steam-water; for bubbly flow only
14)	Chawla [145]	6 – 25		$\vartheta = 0^\circ$; R11; adiabatic, heated
15)	Cioncolini et al. [146]	0.517 – 31.7	3908	steam-water, air-water, nitrogen-water, argon-alcohol, argon-water+alcohol, argon-water, R134a, R245fa; annular
16)	Shannak [147]	0.98 – 257.4	16000	$\vartheta = 0^\circ, 90^\circ$; air-water, steam-water, air-oil, methane-water, methane-oil, nitrogen, nitrogen-water, alcohol-argon, argon-water, R11, R12, R22, R113
17)	Lombardi & Carsana [148]	0.2 – 446	15000	$\vartheta = +90^\circ$; adiabatic, evaporating; steam-water, nitrogen-water, argon-water, argon-water+alcohol
18)	Jung & Radermacher [99]	9.1	> 600	$\vartheta = 0^\circ$; flow boiling; annular flow; pure and mixed refrigerants of R22, R114, R12, R152a

The 21 void fraction models considered within this study are summarized in Table 4.2.

Table 4.2 – Void Fraction correlations used in this study.

No.	Authors	d mm	x []	p_{sat} bar	G $\text{kgm}^{-2} \text{s}^{-1}$	q kWm^{-2}	Geometry	θ °	Remark
Velocity-Ratio and Separated Flow Models									
i	Homogeneous [77]								
ii	Lockhart & Martinelli [96] ^a	1.5 – 25.8		1.2 – 3.6				0; 90	air-benzene, air-kerosene, air-water, oils
iii	Zivi [114] ^a			1 – 82	420 – 830	0 – 30	○, □	0; 90	water-steam; $\theta = 90^\circ$ for □, $\theta = 0^\circ$ for ○
iv	Thom [115] ^a		0.03 – 1	1 – 207				$\theta = 90^\circ$	water-steam
v	Turner & Wallis [117] ^a								
vi	Baroczy [116] ^a	31.75						0; 90	liquid mercury-nitrogen, air-water
vii	Premoli et al. [124]								steam-water, argon-water, nitrogen-water, argon-acetone, argon-ethyl alcohol
viii	Yashar et al. [149]	7.3 – 8.9	0.05 – 0.8	3.5 – 21.3	75 – 700		micro fin	0	adiabatic, evaporation, condensation; R134a, R410A
ix	Cioncolini & Thome [128] ^b	1.05 – 45.5	annular	1.1 – 70	22 – 4500		all		water-steam, R410a, water-air, water-argon, water-nitrogen, water-alcohol-air, kerosene-air
Drift-Flux Models									
x	Zuber & Findlay [118], [150] ^b	50 – 610	bubbly+slug	6 – 180		0	○	90	
xi	Wallis [119] ^b		bubbly					90	
xii	Rouhani & Axelsson [125]	9 – 25			130 – 9080	0 – 1200	○, □-RB	$0^\circ \leq \theta \leq 130^\circ$	○, □, large RB; water, heavy water D ₂ O
xiii	Bonnecaze et al. [151] ^b	152.4	slug					≤ 10	oil-gas
xiv	Dix ^c								
xv	Beattie & Sugawara [152]	73.9						90	steam-water
xvi	Morooka et al. [126]	0 – 0.12		4.9 – 9.8	830 – 1390		(4x4)-RB	90	steam-water
xvii	Bestion [153]	15 – 50.8	0 – 0.99	1 – 120					steam-water
xviii	Gomez et al. [130]	50.8 – 101.6		3.1 – 120.7				$0^\circ \leq \theta \leq 90^\circ$	air-kerosene, air-water, SF_6 -oil, nat-gas-crude
xix	Hibiki & Ishii [154]	25.4 – 60		1				90	air-water
xx	Woldesemayat & Ghajar [123]	12.7 – 102.26	0 – 1					$-90^\circ \leq \theta \leq 90^\circ$	nat-gas-water, air-water, air-kerosene
xxi	Bhagwat & Ghajar [132]	0.5 – 305	0 – 1	1 – 181	10 – 8450		all	$-90^\circ \leq \theta \leq 90^\circ$	various fluids and mixtures

^afrom Butterworth [113]^bflow-pattern-specific model^cfrom Chexal et al. [120], Coddington & Macian [122]

Again, it is important to highlight that some of the selected void fraction models are tailored for specific flow regimes only. Moreover, some frictional pressure drop models are developed for use with specific void fraction correlations and vice versa. Hence – at least in theory – some combinations only make little sense. Nonetheless, bearing this in mind, all possible methods are compared to the entire data set for being consistent. In the following, the experimental data sets available for all three flow directions are compared to the predicted pressure drops. For the vertical flow directions, the 18 frictional pressure drop models and the 21 void fraction correlations considered within this study provide 378 potential prediction methods, resulting from the factorial combinations of the static and frictional components.

4.5.1 Comparison of horizontal data

The 512 experimental data points available for horizontal direction are best predicted by the frictional pressure drop model of Müller-Steinhagen & Heck (MSt&H) [98] that estimates $\xi = 72.07\%$ of the data points within an error band of $\pm 20\%$. As illustrated in Figure 4.7, in particular the data of the slug ($\xi = 83.72\%$), the annular ($\xi = 97.73\%$) and the dryout zone ($\xi = 70\%$) are well predicted by the MSt&H model. However, it underpredicts the measurements of the stratified-wavy and the stratified-wavy+slug region. Table 4.3 provides an overview of the best results split up according to the horizontal flow regimes while Figure 4.8 illustrates the experimental data in comparison to the best identified frictional pressure drop models.

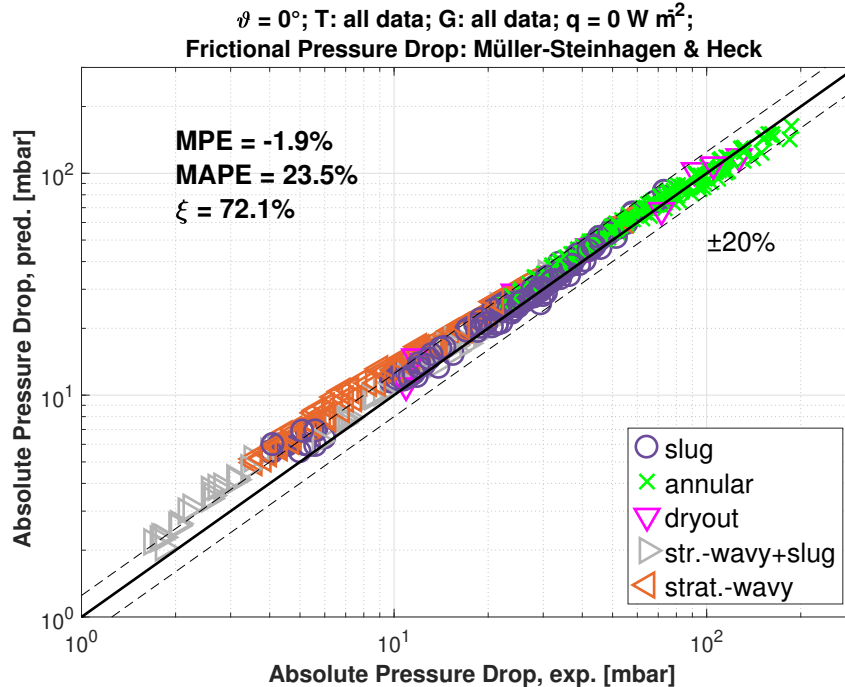


Figure 4.7 – Entire experimental data set in horizontal direction is best predicted by the frictional pressure drop model of Müller-Steinhagen & Heck [98].

Table 4.3 – Statistical comparison between frictional pressure drop models and the entire experimental database, as well as flow pattenr specific comparison, in horizontal direction.

Flow Pattern	#	Frictional Pressure Drop	MAPE	MPE	ξ_{20}
all	512	Müller-Steinhagen & Heck [98]	23.49	-1.92	72.07
bubbly	0	-	-	-	-
slug	172	homogeneous; viscosity: Awad & Muzychka II [143]	13.15	-0.55	83.72
stratified	0	-	-	-	-
stratified-wavy	83	homogeneous; viscosity: McAdams et al. [139]	11.43	1.45	86.75
stratified-wavy+slug	71	Grønnerud [106]	59.07	-0.11	78.87
annular	176	homogeneous; viscosity: Owens [138]	7.9	-1.43	98.3
dryout	10	Sun & Mishima [101]	8.54	6.97	90
mist/vapour	0	-	-	-	-

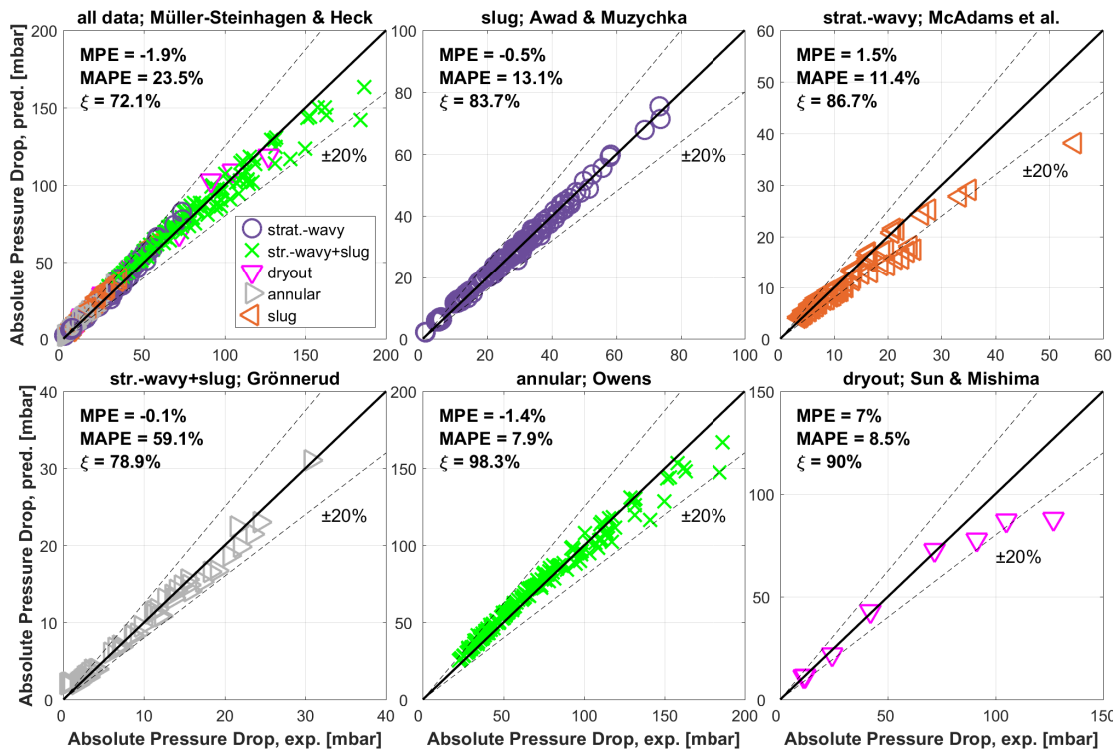


Figure 4.8 – Best performing frictional pressure drop models compared to experimental data in horizontal direction ($\theta = 0^\circ$) grouped according to the flow regimes.

In general, it can be noticed that also the homogeneous two-phase viscosity models predict the horizontal data reasonably well. As mentioned earlier, many studies suggest using the void fraction based homogeneous density (acc. Eq. 4.5) derived from the momentum conservation model for calculating the static head, since it accounts for the slip between the phase velocities. However, it is worth mentioning that the majority of studies recommends the use of the vapour quality based two-phase density (acc. Eq. 4.4) derived from the kinetic energy conservation equation for calculating the frictional pressure losses with the homogeneous two-phase viscosity models. Ghajar & Bhagwat [94] obtained better results when using the vapour quality based two-phase density for predicting the frictional losses. Table 4.4 gives the statistical

comparison of the horizontal data of the present study and the two-phase viscosity models by using (i) the vapour quality based and (ii) the void fraction based two-phase density determined with the model of Woldesemayat & Ghajar [123]. The results in general corroborate with the data by Ghajar & Bhagwat [94]. Only the model of Davidson et al. [141] shows a mirrored behaviour, where the use of the void fraction based two-phase density according to Eq. 4.5 gives better results than the vapour quality based approach (Eq. 4.4).

Table 4.4 – Statistical comparison of the horizontal measurements to the frictional two-phase viscosity models using the vapour-quality-based (Eq. 4.4) and the void-fraction-based (Eq. 4.5) two-phase densities.

Model	two-phase viscosity	ρ_m : vapour quality (Eq. 4.4)			ρ_m : void fraction (Eq. 4.5)		
		MAPE	MPE	ξ_{20}	MAPE	MPE	ξ_{20}
Owens [138]	$\mu_h = \mu_l$	24.48	-2.04	64.07	25.76	7.89	61.13
McAdams et al. [139]	$\mu_h = \left(\frac{1-x}{\mu_l} + \frac{x}{\mu_v} \right)^{-1}$	24.16	7.24	65.08	36.88	13.68	39.45
Cicchitti et al. [140]	$\mu_h = (1-x)\mu_l + x\mu_v$	23.81	2.0	70.51	29.94	10.13	52.34
Davidson et al. [141]	$\mu_h = \mu_l \left(1 + x \frac{\rho_l - \rho_v}{\rho_v} \right)$	70.7	-28.1	23.73	28.34	-5.78	70.51
Garcia et al. [142]	$\mu_h = \mu_l \frac{\rho_h}{\rho_l}$	27.78	9.8	54.58	37.13	13.99	36.91
Awad & Muzychka II [143]	$\mu_h = \mu_v \frac{2\mu_v + \mu_l - 2(\mu_v - \mu_l)(1-x)}{2\mu_v + \mu_l + (\mu_v - \mu_l)(1-x)}$	24.5	4.94	67.8	33.56	12.05	44.73

4.5.2 Comparison of vertical upflow data

The 295 experimental data points of CO₂ two-phase flow recorded in vertical upward direction are compared to the 378 vertical pressure drop models considered within this study, resulting from the factorial combinations of the 18 frictional pressure drop models and the 21 void fraction correlations accounting for the static head. Figure 4.9 illustrates the statistical comparison of the prediction models to the database. However, it has to be noted that some models are flow-pattern-specific and as a consequence it is not surprising that some methods show poor results when comparing them to the entire data set. The plots in Figure 4.9 suggest that the velocity-ratio based void fraction correlations of Baroczy [116] and Premoli et al. [124] yield the best performances in combination with many frictional pressure drop correlations, followed by the drift-flux models of Rouhani & Axelsson [125], Hibiki & Ishii [154], Woldesemayat & Ghajar [123] and Bhagwat & Ghajar [132]. In addition, all homogeneous frictional pressure drop models based on the two-phase viscosity concept – except the approach of Davidson et al. [141] – show generally good agreement with the experimental data in combination with some void fraction correlations. However, as already discussed earlier, the results in Table 4.4 give rise to the suspicion that the two-phase viscosity model of Davidson et al. [141] performs better when using the void fraction based two-phase density according to Eq. 4.5. Moreover, the frictional models of Friedel [97], Müller-Steinhagen & Heck [98], Sun & Mishima [101], Grønnerud [106] and Shannak [147] reveal good general performances. The best results in terms of the lowest mean absolute percentage error (MAPE) and mean percentage error (MPE) are provided by the combination of the Müller-Steinhagen & Heck [98] model with the void fraction correlation of Baroczy [116], followed by the Friedel [97] model combined with the correlation of Premoli et al. [124]. The combination of the Sun & Mishima [101] model with

the correlation of Baroczy [116] shows the best results in terms of the highest amount of data points within an error band of $\pm 20\%$. All three models are compared to the experimental data in Figure 4.10.

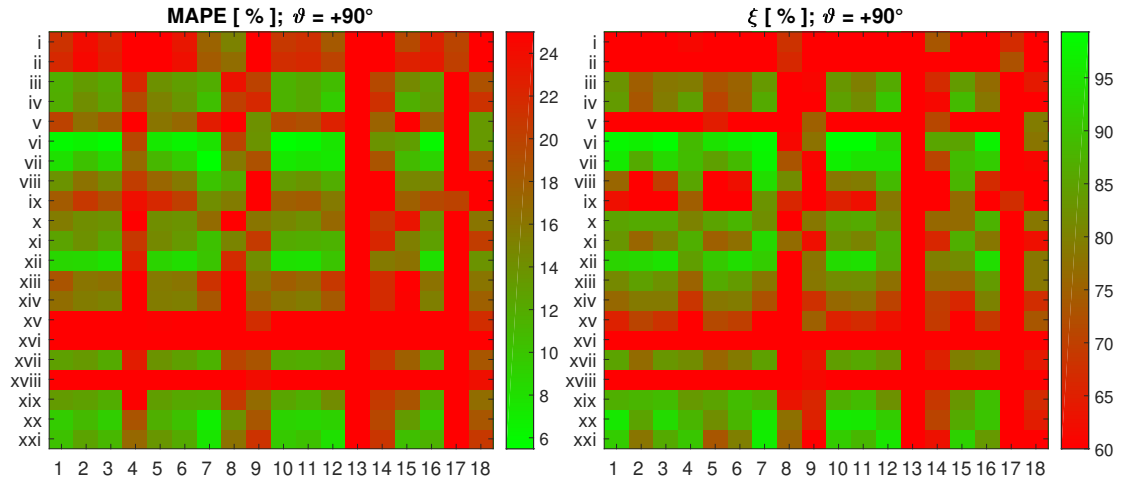


Figure 4.9 – Graphical representation of the statistical comparison (MAPE [%] and ξ_{20} [%]) between the compiled experimental data set (295 measurements) for CO₂ two-phase flow in vertical upward direction ($\vartheta = +90^\circ$) and the predicted pressure drops according the 378 possible combinations considered. The frictional pressure drop models are depicted on the abscissae in arabic numbers as listed in Table 4.1, the ordinates represent the void fraction correlations with roman numbers according to Table 4.2.

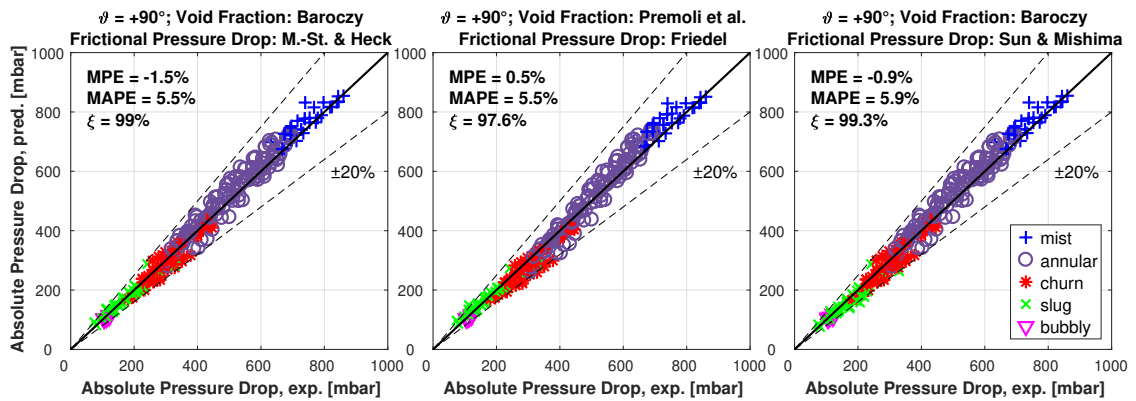


Figure 4.10 – Entire experimental data set in vertical upward direction ($\vartheta = +90^\circ$) compared to the best performing pressure drop models. Left: The combination of the frictional model of Müller-Steinhagen & Heck [98] and the void fraction correlation of Baroczy [116]; Middle: The Friedel [97] model combined with the void fraction correlation of Premoli et al. [124]; Right: The model of Sun & Mishima [101] in combination with the void fraction correlation of Baroczy [116].

Table 4.5 provides detailed information about the statistics of the best performing pressure drop models in vertical upward direction in comparison to the entire database, as well as the best flow pattern specific solutions. Figure 4.11 groups the experimental data according to the

flow regimes and compares the measurements to the best suitable pressure drop models. The subdivided analysis of the pressure drop measurements according to the flow regimes reveals that at low vapour qualities in the bubbly and slug flow patterns, both the slip-ratio as well as the drift-flux void fraction correlations show good results, in particular the slip-ratio models of Baroczy [116] and Premoli et al. [124] and the drift-flux models of Zuber & Findlay [118],[150], Wallis [119], Rouhani & Axelsson [125], Hibiki & Ishii [154], Woldesemayat & Ghajar [123] and Bhagwat & Ghajar [132]. However, at increasing vapour qualities in the churn and annular flow regimes, the separated flow models of Baroczy [116] and Premoli et al. [124] present better agreement with the experimental data than the drift-flux models, what is commonly accepted in the literature, since they account for the velocity differences of the concurrent phases. Only the correlations of Woldesemayat & Ghajar [123] and Bhagwat & Ghajar [132] are able to compete at increased vapour qualities to a certain extend, what corroborates the statements made by Cioncolini et al. [146] even though the physics of drift-flux models is not appropriate for high phase velocity slippage rates.

Table 4.5 – Statistical comparison of the 295 experimental data points in vertical upward direction ($\vartheta = +90^\circ$) and the best performing aggregate pressure drop models as a combination of the frictional and the static component.

Pattern	#	Frictional Pressure Drop	Void Fraction	MAPE	MPE	ξ_{20}
all	295	Müller-Steinhagen & Heck [98]	Baroczy [116]	5.48	-1.51	98.98
		Friedel [97]	Premoli et al. [124]	5.55	0.49	97.63
		Sun & Mishima [101]	Baroczy [116]	5.87	-0.85	99.32
bubbly	34	Jung & Radermacher [99]	homogeneous [77]	2.93	-1.11	100
		Jung & Radermacher [99]	Woldesemayat & Ghajar [123]	3.34	-1.07	100
		homogeneous; Garcia et al. [142]	homogeneous [77]	3.35	-2.84	100
slug	142	Friedel [97]	Woldesemayat & Ghajar [123]	4.3	1.07	100
		Cioncolini et al. [146]	Premoli et al. [124]	4.41	1.57	100
		homogeneous; Davidson et al. [141]	Premoli et al. [124]	4.48	0.52	100
churn	73	homogeneous; Owens [138]	Rouhani & Axelsson [125]	4.13	0.75	100
		Sun & Mishima [101]	Rouhani & Axelsson [125]	4.15	0.85	100
		Müller-Steinhagen & Heck [98]	Rouhani & Axelsson [125]	4.23	0.9	100
annular	39	Müller-Steinhagen & Heck [98]	Baroczy [116]	7.33	-1.26	92.31
		Friedel [97]	Premoli et al. [124]	7.52	-2.9	92.31
		Müller-Steinhagen & Heck [98]	Premoli et al. [124]	7.77	3.18	92.31
mist/vapour	7	Sun & Mishima [101]	Bhagwat & Ghajar [132]	2.61	1.16	100
		Grønnerud [106]	Turner & Wallis [117]	2.68	0.66	100
		Sun & Mishima [101]	Turner & Wallis [117]	2.71	2.71	100

The comparison of the measurements to the calculated pressure drops and its constituent components confirms that the previously highlighted prediction models are well in agreement with the data set in vertical upward direction. Figure 4.12 represents some pressure drop measurements in comparison to the total predicted pressure drop according to the frictional model of Müller-Steinhagen & Heck [98] and the void fraction correlation of Baroczy [116], as well as the respective pressure drop components and confirms that the momentum pressure drop is negligible within the present data. The comparisons of the measured and calculated pressure drops in Figure 4.12 corroborate the statements made earlier in section 4.4. In general, the static component is dominant at low vapour qualities in long vertical pipes. As a consequence, the accuracy of the pressure drop calculation at low vapour qualities is mainly influenced by the accuracies of the vapour quality calculation and the void fraction method.

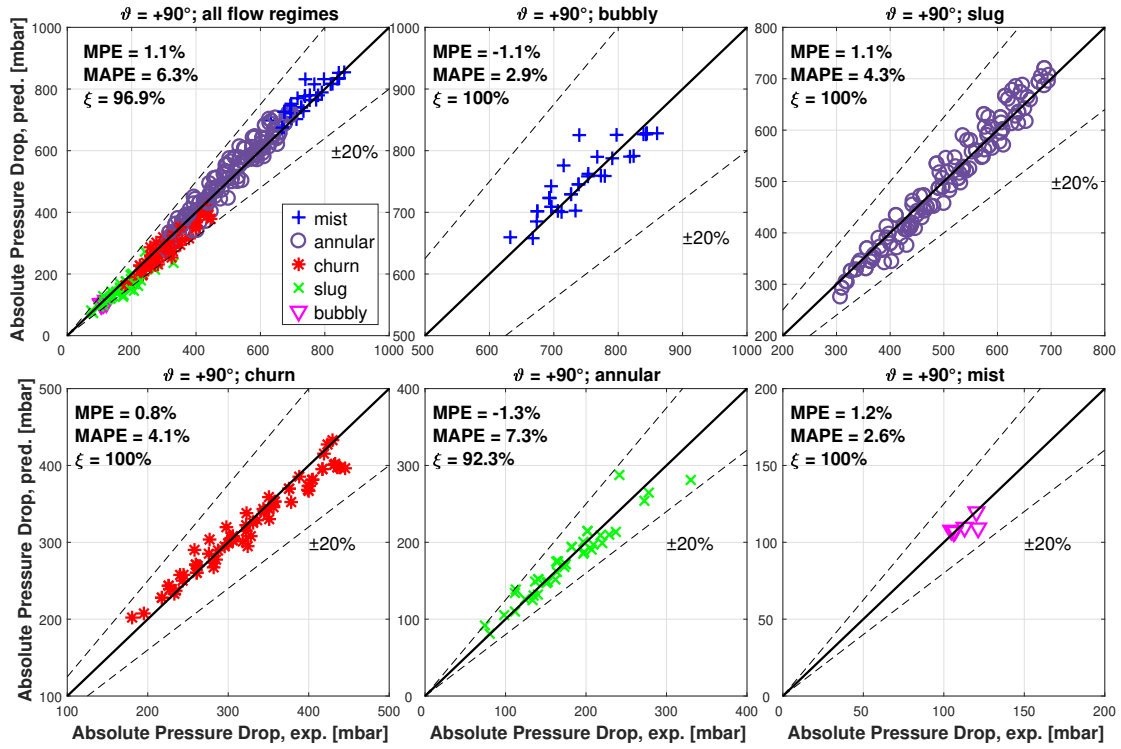


Figure 4.11 – Experimental data in vertical upward direction analyzed in regard of the flow regimes. Top left: all data points compared to the homogeneous two-phase viscosity model of Awad & Muzychka II [143] and the void fraction correlation of Baroczy [116]. The pressure drop data grouped according the flow regimes is best predicted by the frictional pressure drop models and the void fraction correlations of: top middle: Jung & Radermacher [99] and the homogeneous void fraction model for bubbly flow; top right: Friedel [97] and Woldesemayat & Ghajar [123] for slug flow; bottom left: homogeneous two-phase viscosity model of Owens [138] and Rouhani & Axelsson [125] for churn flow; bottom middle: Müller-Steinhagen & Heck [98] and Baroczy [116] for annular flow; bottom right: Sun & Mishima [101] and Bhagwat & Ghajar [132] for mist/vapour flow. The statistical comparison is given in Table 4.5.

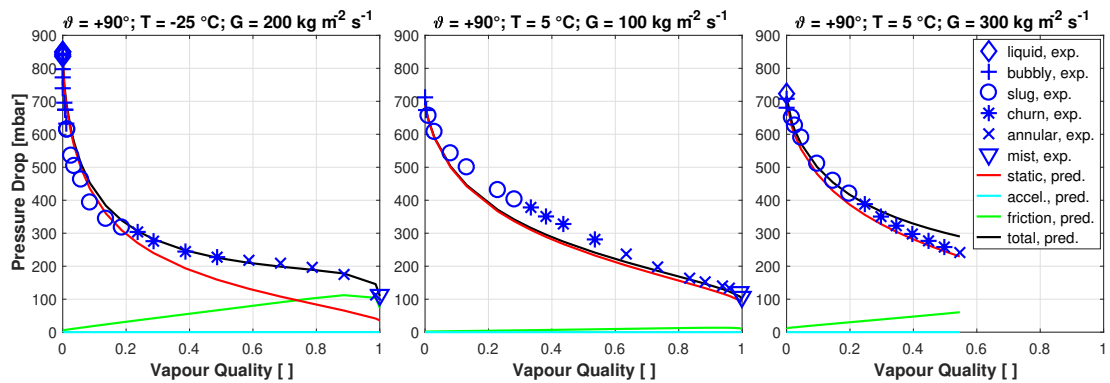


Figure 4.12 – Measured and predicted pressure drops in upward direction ($\theta = +90^\circ$) according the frictional model of Müller-Steinhagen & Heck [98] and the static head with the void fraction correlation of Baroczy [116]. The total pressure drop results from the superposition of the static head (red), the frictional (green) and the accelerational component (cyan).

4.5.3 Comparison of vertical downflow data

Applying the same procedure as for the vertical upward direction, the 295 experimental data points recorded for downflow are compared to the 378 pressure drop models considered within this study. Again, within the assessment of the prediction methods one has to be aware that some models have been designed for specific flow patterns exclusively. The statistical comparison of the pressure drop models to the experimental data is summarized in Figure 4.13 and it can be noticed that the pressure drop models generally predict the experimental data in downward direction significantly less accurately than the data in upward direction, what is emphasized by the scales of the plots. The homogeneous void fraction model, the separated flow models of Lockhart & Martinelli [96], Yashar et al. [149] and Cioncolini & Thome [128], as well as the drift-flux models of Woldesemayat & Ghajar [123] and Bhagwat & Ghajar [132] show the best results in combination with the frictional pressure drop models. However, the statistical indicators are not satisfying. In turn, only the frictional pressure drop model of Lombardi & Carsana [148] shows general agreement with the experimental data throughout all void fraction correlations.

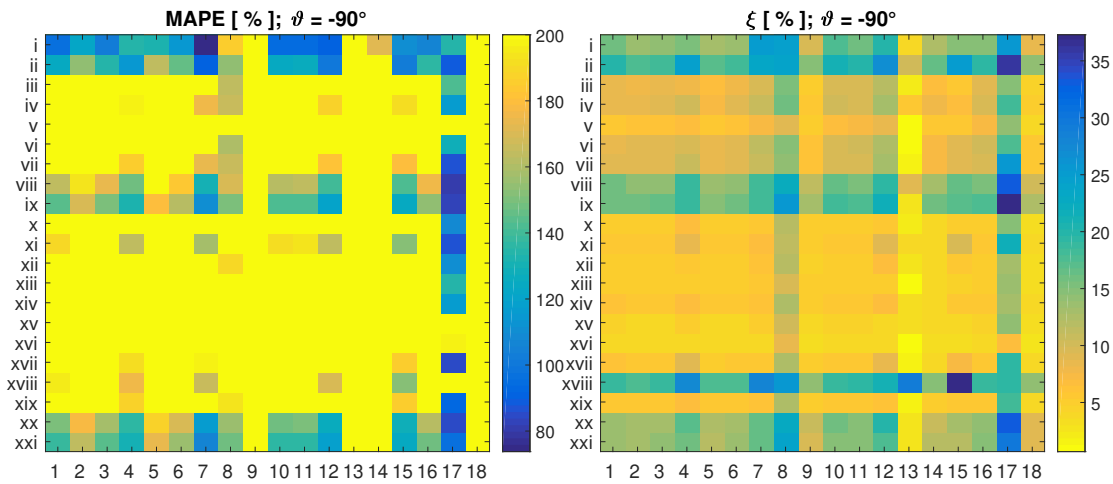


Figure 4.13 – Graphical representation of the statistical comparison (MAPE [%] and ξ_{20} [%]) between the compiled experimental data set (295 measurements) in vertical downward direction ($\theta = -90^\circ$) and the predicted pressure drops according to the 378 possible combinations considered. The frictional pressure drop models are depicted on the abscissa in arabic numbers as listed in Table 4.1, the ordinate represents the void fraction correlations with roman numbers according to Table 4.2.

The best results in terms of the lowest MAPE is provided by the combination of the Friedel [97] model and the homogeneous void fraction correlation. The frictional pressure drop model of Lombardi & Carsana [148] combined with the void fraction correlation of Cioncolini & Thome [128] predicts the highest amount of data points within an error band of $\pm 20\%$. The three leading pressure drop models are compared to the experimental downflow data in Figure 4.14.

Table 4.6 – Statistical comparison of the 295 experimental data points in vertical downward direction ($\theta = -90^\circ$) and the best performing aggregate pressure drop models as a combination of the frictional and the static component.

Pattern	#	Frictional Pressure Drop	Void Fraction	MAPE	MPE	ξ_{20}
all	295	Friedel [97]	homogeneous [77]	73.78	-58.29	25.08
		Lombardi & Carsana [148]	Cioncolini & Thome [128]	83.55	49.07	37.29
		Lombardi & Carsana [148]	Woldesemayat & Ghajar [123]	84.47	42	33.22
bubbly	2	Lockhart & Martinelli [96]	Baroczy [116]	0.43	-0.43	100
		Friedel [97]	Baroczy [116]	0.63	-0.63	100
		Lombardi & Carsana [148]	Hibiki & Ishii [154]	0.74	-0.12	100
slug	90	Lombardi & Carsana [148]	Lockhart & Martinelli [96]	22.15	-4.1	66.67
		Lombardi & Carsana [148]	Cioncolini & Thome [128]	24.48	-16.84	62.22
		Lombardi & Carsana [148]	Woldesemayat & Ghajar [123]	30.07	-27.97	52.22
churn	146	Lombardi & Carsana [148]	Yashar et al. [149]	68.95	8.88	25.34
		Lombardi & Carsana [148]	Cioncolini & Thome [128]	72.68	35.84	28.08
		Lombardi & Carsana [148]	Woldesemayat & Ghajar [123]	75.23	31.24	26.03
annular	48	Müller-Steinhagen & Heck [98]	homogeneous [77]	26.46	1.15	47.92
		Friedel [97]	homogeneous [77]	28.78	12.27	54.17
		Cioncolini et al. [146]	Gomez et al. [130]	29.52	13.16	62.5
mist/vapour	9	Grønnerud [106]	Turner & Wallis [117]	3.29	-1.42	100
		Shannak [147]	Yashar et al. [149]	3.99	-1.85	100
		Sun & Mishima [101]	Cioncolini & Thome [128]	4.75	-1.15	100

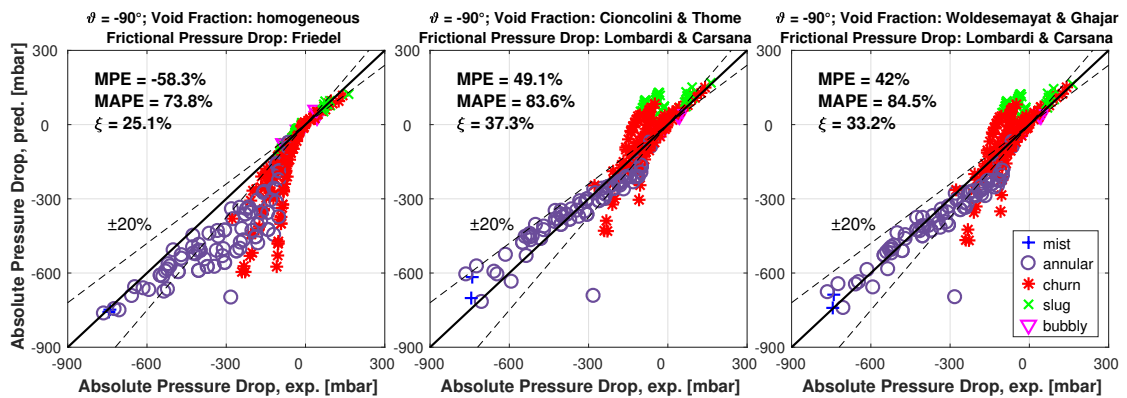


Figure 4.14 – Experimental data in vertical downward direction ($\theta = -90^\circ$) compared to the calculated pressure drops according to the combinations of Friedel [97] and the homogeneous void fraction correlation (left), Lombardi & Carsana [148] and Cioncolini & Thome [128] (middle) and Lombardi & Carsana [148] and Woldesemayat & Ghajar [123] (right).

In addition to the three best performing combinations over the entire data set, Table 4.6 provides detailed information about the statistics of the best flow pattern specific solutions. Figure 4.15 illustrates the comparison according to the flow regimes and presents the most appropriate pressure drop models. The detailed analysis of the pressure drop measurements shows that at low vapour qualities – or rather in the bubbly, the slug and the churn region – only the frictional pressure drop model of Lombardi & Carsana [148] provides reasonable results. All the other frictional models investigated within this study show a tendency to underpredict the experimental data. At increased vapour qualities in the churn and annular patterns, the universal models by Müller-Steinhagen & Heck [98], Friedel [97], Grønnerud [106] and Shannak [147] provide a better accuracy than the Lombardi & Carsana model [148] that

tends to overpredict the pressure losses. On the other hand, the homogeneous void fraction model and the correlations by Lockhart & Martinelli [96], Yashar et al. [149], Cioncolini & Thome [128], Woldesemayat & Ghajar [123] and Bhagwat & Ghajar [132] show best results over the entire database of vertical downflow. Both the void fraction models by Woldesemayat & Ghajar [123] and Bhagwat & Ghajar [132] have been built and verified upon a database containing both vertical upflow and downflow data. For that reason it is not surprising that both show reasonable results in downward direction. Still, the databases compiled in their studies were not equally balanced in regard of up- and downflow measurements, what might explain the better performance in vertical upward direction.

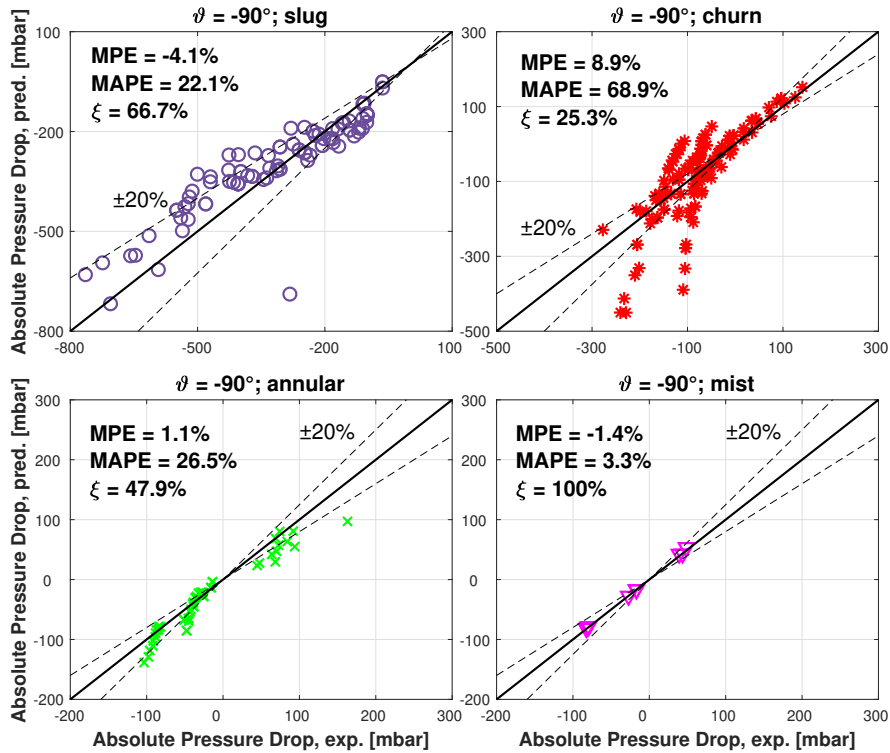


Figure 4.15 – Experimental data in vertical downward direction ($\vartheta = -90^\circ$) analyzed in regard of the flow regimes. Top left: all data points for slug flow compared to the frictional pressure drop model of Lombardi & Carsana [148] and the void fraction correlation of Lockhart & Martinelli [96]; top right: the model of Lombardi & Carsana [148] and the void fraction correlation of Yashar et al. [149] for churn flow; bottom left: the model of Müller-Steinhagen & Heck [98] and the homogeneous void fraction correlation for annular flow; bottom right: the model of Grønnerud [106] and the void fraction correlation of Turner & Wallis [117] for mist flow.

Figure 4.16 illustrates the best performing combinations of the frictional and static components in vertical downward direction. It can be noticed that the aggregate calculated pressure drops, where the frictional model of Lombardi & Carsana [148] is involved, are generally in good agreement with the measurements recorded in downward direction. However, as can be noticed in Figure 4.16, the frictional model of Lombardi & Carsana [148] shows increased

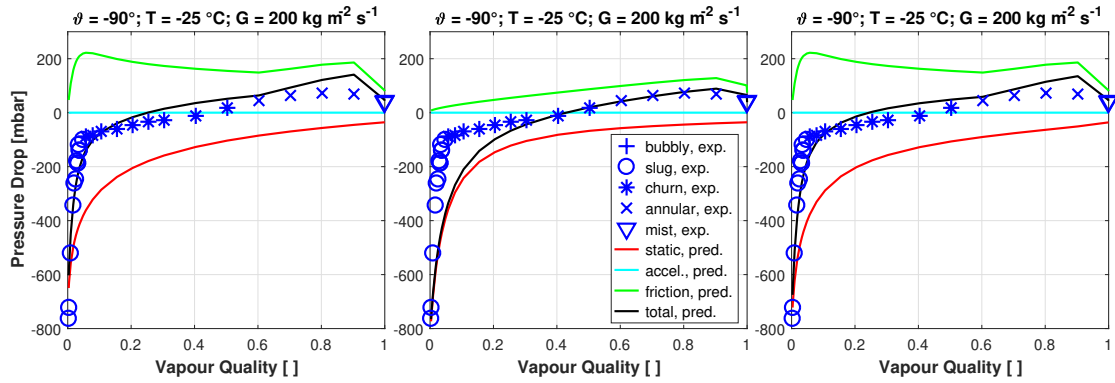


Figure 4.16 – Measured and predicted pressure drops in the vertical downward channel ($\vartheta = -90^\circ$) at $T_{sat} = -25^\circ\text{C}$, $G = 200\text{ kg m}^{-2}\text{ s}^{-1}$. The total pressure drop results from the superposition of the static head (red), the frictional (green) and the accelerational components (cyan). Left: Frictional pressure drop model of Lombardi & Carsana [148] and void fraction correlation of Cioncolini & Thome [128]; middle: Frictional pressure drop model of Friedel [97] and the homogeneous void fraction model; right: Frictional pressure drop model of Lombardi & Carsana [148] and void fraction correlation of Woldeesemayat & Ghajar [123].

frictional losses at low vapour qualities ($x < 0.3$). This gives rise to the suspicion that the frictional component is overpredicted at low vapour qualities by this model and compensates for the underprediction of the static component. This theory corroborates the statements made earlier in section 4.4 concerning the analysis of the pressure drop components, where the influence of the static component seems to be strongly reduced at low mass flow rates in downward direction, where the liquid column disappears due to phase separation [134]. The analysis of the pressure drop components throughout all combinations, represented by some examples in Figure 4.16, confirms that these effects are not incorporated by any void fraction model investigated within this study and that the static head, in particular at low mass flow rates, where the flow turns into annular flow even at very low vapour qualities, is not predicted satisfactorily. Furthermore, the loss of the static head due to the disappearing liquid column seems to happen abruptly and can be seen as a discontinuity appearing at mass velocities around $G < 300\text{ kg m}^{-2}\text{ s}^{-1}$ where the buoyancy forces become predominant over the flow inertia. These observations can be general motivation to intensify investigations of pressure drops, and in particular void fraction correlations, in vertical downward direction for CO_2 two-phase flows.

4.6 Conclusion

Pressure drop measurements of two-phase flow of CO₂ in horizontal ($\vartheta = 0^\circ$), vertical upward ($\vartheta = +90^\circ$) and downward ($\vartheta = -90^\circ$) direction have been carried out in a dedicated test facility with unheated test sections of 8 m length and inner tube diameters of 8 mm. A database of more than 1100 data points – consisting of 295 measurements for each vertical (upflow and downflow respectively) and 512 for horizontal direction – has been compiled within the present study. The analysis of the steady state pressure drop measurements reveals that the slug flow regime is in general an unstable pattern, where increasing oscillations in the pressure signals are detected. These oscillations get amplified in the two vertical setups where buoyancy has a significant impact on the pressure gradients inside the channels. The experiments have been carried out under adiabatic conditions without applying artificial heating to the test sections and the momentum pressure losses due to the heat flux from ambient are found to be negligible.

The 512 data points recorded in horizontal direction have been compared to 18 frictional pressure drop models and are best described by the model of Müller-Steinhagen & Heck [98] with a MAPE of 23.49 % and predicting 72.07 % of the data points within a deviation of ± 20 %. Also the two-phase viscosity models by Owens [138], Cicchitti et al. [140] and Awad & Muzychka II [143] show reasonable results when using the vapour quality based two-phase density derived from the energy conservation equation. The subdivided analysis of the pressure drop data according to the flow regimes is presented in Table 4.3.

In addition to the 18 frictional pressure drop models, 21 void fraction correlations have been considered to account for the static head in the analysis of the vertical pressure drop measurements. The factorial combinations of frictional and static components result in 378 pressure drop models for analyzing the vertical losses. In vertical upward direction, the combination of the frictional pressure drop model of Müller-Steinhagen & Heck [98] and the void fraction correlation of Baroczy [116] provides the best results in terms of the lowest MAPE of 5.48 %. The model of Sun & Mishima [101] combined with the void fraction correlation of Baroczy [116] provides the highest amount of data points within an error band of ± 20 % ($\xi = 99.32$ %). The subdivided analysis in regard of the flow regimes is given in Table 4.5. In general, the void fraction correlations of Baroczy [116] and Premoli et al. [124] show the best performances in combination with many frictional pressure drop models throughout all flow regimes, followed by the drift-flux models of Rouhani & Axelsson [125], Hibiki & Ishii [154], Woldesemayat & Ghajar [123] and Bhagwat & Ghajar [129]. In regard of the frictional pressure drop component, the homogeneous two-phase viscosity models [138],[139],[140],[142],[143], as well as the models of Friedel [97], Müller-Steinhagen & Heck [98], Sun & Mishima [101], Grønnerud [106] and Shannak [147] reveal good results in combination with many void fraction correlations.

The comparison in vertical downward direction reveals that the prediction models generally perform less accurately than in vertical upward direction. It is concluded that the effect of flow

separation at low mass flow rates, where buoyancy forces dominate over the inertia forces of the flow, is not sufficiently taken into consideration by the void fraction correlations considered within this study. For that reason, it is highly recommended to put a main emphasis on the detailed analysis of the static head, in particular in downward direction, in future vertical flow studies with CO₂.

5 Heat Transfer

A sound understanding of the two-phase flow phenomena inside the channels is imperative for designing evaporative cooling systems efficiently and the accurate prediction of the local two-phase heat transfer coefficients is of substantial importance for the engineering of heat exchanging processes. This chapter focuses on investigating the heat transfer characteristics of flow boiling CO₂ in vertical upward direction. The content and the results presented here have been submitted and are currently under review by the following journal:

- D. Schmid, B. Verlaet, P. Petagna, R. Revellin and J. Schiffmann. "Heat transfer of flow boiling carbon dioxide in vertical upward direction", *International Journal of Heat and Mass Transfer*, under review, submitted: Dec 09, 2021.

5.1 Literature Review

5.1.1 General heat transfer prediction methods for flow boiling of refrigerants

Flow boiling is typically defined as a superposition of a nucleate and a convective boiling contribution. The model of Chen [155] was amongst the first methods developed for predicting flow boiling heat transfer in vertical upflow and was initially tested with data points of water and organic fluids available at that time. Chen [155] proposed his correlation as a sum of nucleate and convective boiling components with a respective boiling suppression factor and a two-phase convection multiplier. Later, Shah [156] presented a flow boiling correlation for horizontal and vertical flows based on a graphical method [157]. Instead of combining the nucleate and convective terms, this method suggests using the larger of the two. Over the last decades, both correlations have been proven to achieve good performance and are – besides the model of Wojtan et al. [44],[45] – amongst the most widely used methods for predicting heat transfer mechanisms in flow boiling applications of refrigerants. Due to their success, these approaches have been seized and further developed based on increased databases and therefore making them applicable to a wider range of validity and conditions. Gungor and Winterton [158] and Liu and Winterton [159] presented updated versions of the Chen-

method built upon 3693 and more than 4300 data points from water, ethylene, glycol and several refrigerants (R11, R12, R22, R113, R114) respectively. Gungor and Winterton [160] then suggested a simplified correlation based on convective boiling only. Kandlikar [161] developed a correlation for horizontal and vertical flows incorporating the fluid characteristics with a fluid-dependent parameter. This development made use of a data set of 5246 measurements from ten fluids, however, without data from CO₂. Steiner and Taborek [162] presented an asymptotic model for vertical flow boiling that incorporates the thresholds and boundaries of the nucleate and convective boiling contributions. This correlation is applicable for a wide range of conditions and has been validated with a data set of 13000 measurements from water, refrigerants (R11, R12, R22, R113), hydrocarbons (benzene, n-pentane, n-heptane, cyclohexane, methanol, ethanol, n-butanol), cryogenics (nitrogen, hydrogen, helium) and ammonia. More recently, Fang et al. [92] presented a general model designed for all pipe orientation, covering various channel sizes and flow conditions. The correlation was fitted to a data set of 17778 data points, containing measurements from 101 sources and 13 different fluids, including CO₂. The model has been validated with a second, independent data set of 6664 measurements. Similar to the method of Kandlikar [161], the correlation of Fang et al. [92] also incorporates a fluid-dependent parameter.

5.1.2 Flow boiling heat transfer of CO₂

Heat transfer investigations with CO₂ have been intensified significantly within the last two decades due to the rising interest in natural and eco-friendly working fluids. Thome and Ribatski [68] conducted a comprehensive "state-of-the-art" review and provided an overview of the heat transfer related to flow boiling of CO₂ in macro- and micro-channels. They gathered heat transfer data from the studies available and compared the measurements to several heat transfer prediction methods. The analysis of the macro-scale database [103],[163],[164],[107],[165] reveals that the CO₂-tailored heat transfer prediction method of Thome and El Hajal [166] gave the best results, predicting 60 % of the data points within a deviation of ± 30 %. However, in particular the data points at high vapour qualities at the transition from annular to the post-dryout region are not well captured. Cheng et al. [70],[71] addressed this problem and developed a new flow boiling heat transfer model for CO₂ intrinsically related to a new flow pattern map. The model proposed is applicable to an increased range of horizontal flow conditions, such as tube diameters from 0.8 to 10 mm, mass velocities from 85 to 570 kg m⁻² s⁻¹, heat fluxes from 5 to 32 kW m⁻² and saturation temperatures from -25 to +25 °C. The model predicts 75.5 % of their CO₂ database, comprising 318 measurements, within ± 30 %. An updated version covering all flow regimes and applicable for a wider range of conditions has been presented by Cheng et al. [167]. This study incorporates heat transfer models for bubbly and mist flow and presents an updated heat transfer correlation in the dryout region. The new model is applicable for an increased range of conditions, covering horizontal tubes with inner diameters ranging from 0.6 to 10 mm, mass velocities from 50 to 1500 kg m⁻² s⁻¹, heat fluxes from 1.8 to 46 kW m⁻² and saturation temperatures from -28 to +25 °C. This model performed well on an updated data set, comprised of 1124 measurements,

with 71.4 % of the entire data set being predicted within a deviation of ± 30 %. Many studies on CO₂ heat transfer measurements recorded after 2007 confirm the good performance of the Cheng et al. [167] model. Mastrullo et al. [168], for example, carried out 217 measurements in smooth horizontal tubes of 6 mm diameter within the flow conditions specified in [167]. The statistical analysis of this data set shows that the heat transfer model by Cheng et al. [167] predicts 75.6 % of the data points within an error band of ± 30 % [168],[169]. In their most recent study, Cheng et al. [74] summarized the flow boiling studies of CO₂ carried out after 2007 and compiled a database of 4733 measurements, including the data already used in [167]. A comparison of this database to the prediction model of Cheng et al. [167] shows that 61.7 % of the entire database is predicted within ± 30 %. By excluding the post-dryout data, the accuracy of the Cheng et al. model increases to 81.8 %. The general potential and trends of CO₂ as a working fluid are analyzed and summarized by Mastrullo et al. [170]. Hellenschmidt and Petagna [171] addressed heat transfer investigations in horizontal two-phase flow of CO₂ in the transition zone from macro- to microchannels under various flow conditions, in particular focusing on the influence of saturation temperature. They conclude that the alteration of fluid properties, combined with changes in flow confinement, influence and change the phenomenological behaviour of the flow and propose a differentiated analysis of the heat transfer data accounting for the changing flow phenomena.

5.1.3 Nature of the issue and objective of the present chapter

Heat transfer measurements of horizontal two-phase flow of CO₂ have been carried out under various flow conditions, channel sizes and geometries within the recent years and validated heat transfer correlations are available for predicting evaporative flows of CO₂ in horizontal direction. However, no experimental heat transfer data of vertical two-phase flow of CO₂ are available so far and as a consequence, no heat transfer model has been validated for this purpose. To fill in this void, the objective of the present chapter is a suitable model that acceptably predicts the heat transfer mechanisms of CO₂ in vertical upward direction.

5.2 The Test Sections and the Database

The experimental test facility described in section 2.1.2 is designed for heat transfer measurements in vertical upward direction. The test section consists of an 8 m long smooth stainless steel tube EN 1.4404 (316L) with inner and outer diameters of 8 and 10 mm respectively. The fluid temperature at the in- and outlet of the test section is measured with RTDs (PT100) that are in direct contact with the fluid. Seven additional PT100 temperature probes (TT2A42 - TT2A54) are mounted onto the outer perimeter of the test section with a distance of 1 m between each other to measure the local outer wall temperature of the evaporator. The temperature probes TT2A42 - TT2A54 are attached with Kapton tape and thermal paste has been added to maximize the heat transfer between the sensor tips and the tube surface. The pressure is monitored with absolute pressure transmitters at the inlet and outlet respectively and the pressure difference across the test section is directly measured with a differential pressure transmitter. The test section is directly heated by means of the Joule effect, where direct current, provided by a *DELTA ELEKTRONIKA SM 60-100* power supply, is applied on the stainless steel tube of the test section through tailor-made copper clamps. The distance between the copper clamps is 8 m and the accuracy of the evaporator length is neglected due to $\Delta l \ll l$. The current and voltage between the copper clamps are monitored with the analog interface of the power supply and the test section is insulated with dielectric fittings. Figure 5.1 shows a cross-sectional view of the test section.

The local saturation pressure inside the evaporator is determined with a linear interpolation between the absolute pressure measurements at the inlet (2A40) and outlet (2A58) of the test section and is constantly validated with the differential pressure measurement (DP2A40). Although the real pressure distribution inside an evaporator is non-linear, this simplified model based on real measurements still provides better accuracy than a calculated pressure profile based on a pressure drop correlation that results in higher uncertainties due to error propagation compared to the deviations of the real pressure profile to a linear model. Moreover, a linear assumption is applicable for moderate changes in vapour quality, what applies to the experiments of the present study due to the moderate heat fluxes. The local heat transfer coefficient is defined according to [77],[76]

$$\alpha_{loc} = \frac{q}{T_{w,i} - T_{sat,loc}} \quad (5.1)$$

where q corresponds to the local heat flux from the tube perimeter to the fluid, $T_{sat,loc}$ denotes the local bulk saturation temperature of the fluid determined from the local saturation pressure and $T_{w,i}$ is the local wall temperature at the inner tube perimeter of the evaporator. The temperature difference between the outer and inner tube perimeter, $\Delta T_w = T_{w,o} - T_{w,i}$, is determined with the one-dimensional, radial steady-state heat conduction equation by

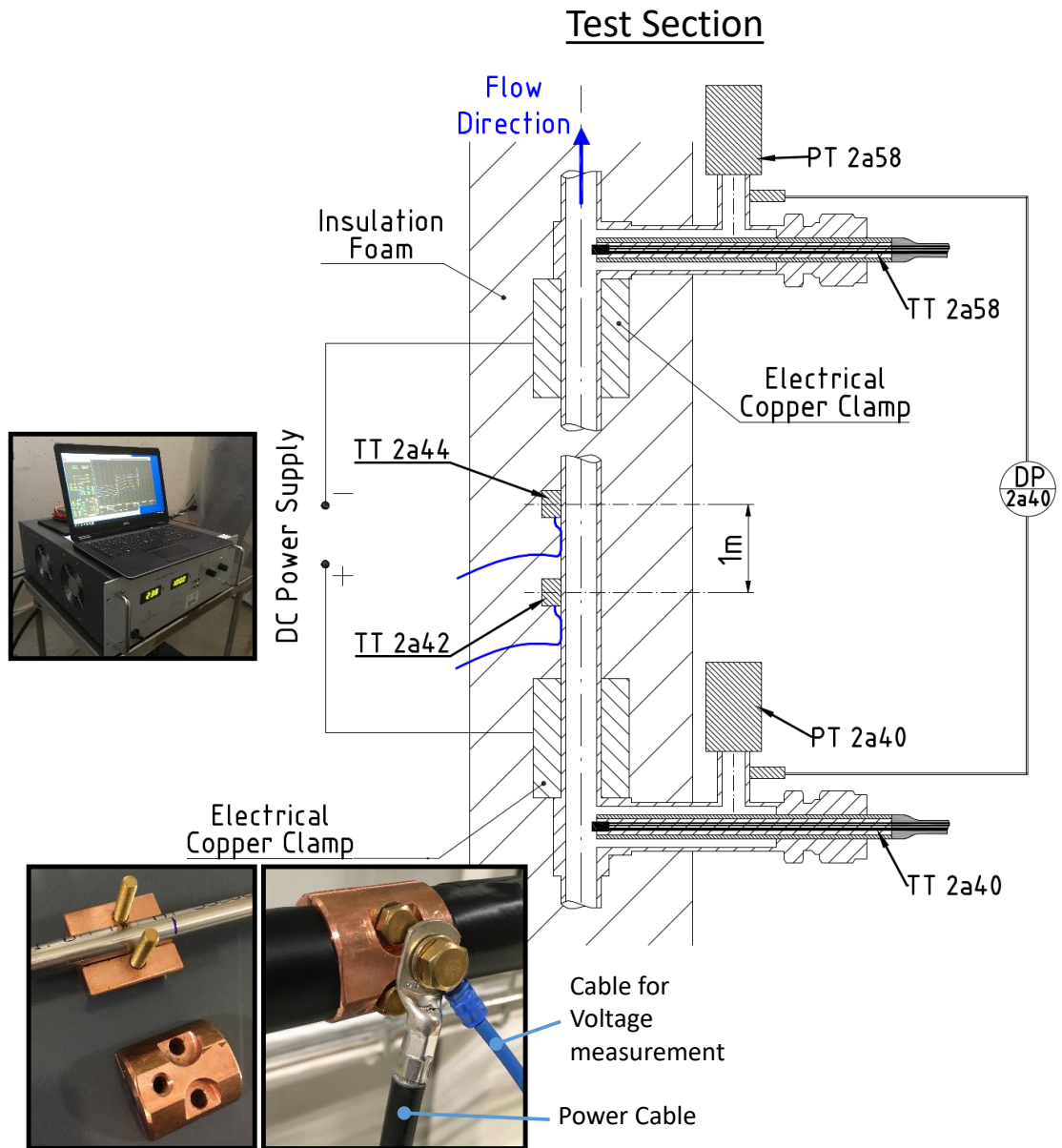


Figure 5.1 – Cross-sectional view of the test section.

assuming a uniform heat flux

$$\Delta T_w = \frac{q \cdot d_i}{4k_{1.4404}} \cdot \frac{\psi(1 - \ln \psi) - 1}{1 - \psi} \quad (5.2)$$

where $\psi = (d_o/d_i)^2$ is calculated with the outer and inner tube diameter and $k_{1.4404}$ is the temperature-dependent conductivity of stainless steel 1.4404 (316L) [172]. The test setup has

been validated with diabatic single-phase calibration measurements described in chapter 2.4.2.5 and the accuracy of the calibrated instrumentation, as well as the uncertainty of the deduced measurements are provided in Table 2.3. In total, 1941 local heat transfer measurements for vertical upflow have been carried out within the test conditions described in chapter 2.2. The details of the database with regard to saturation temperature, mass velocity, heat flux and flow pattern are shown in Figure 5.2.

The flow regimes of adiabatic and diabatic flows might differ when looking at the details, e.g. due to bubble formation at the nucleation sites at the inner tube perimeter of the evaporator. However, the differences between adiabatic and diabatic conditions are assumed to be of minor order importance, at least at moderate heat fluxes that are far from the departure of nucleate boiling (DNB or CHF), which is the case for the test conditions of the present study. For that reason, the local flow regimes inside the evaporator are determined according to the adiabatic flow pattern map presented in [134]. The present work only covers flow boiling of CO₂ where the two-phase flow is in saturated thermodynamic conditions. Thermodynamic non-equilibrium boiling, such as subcooled boiling or post-dryout evaporation, are not covered within this study.

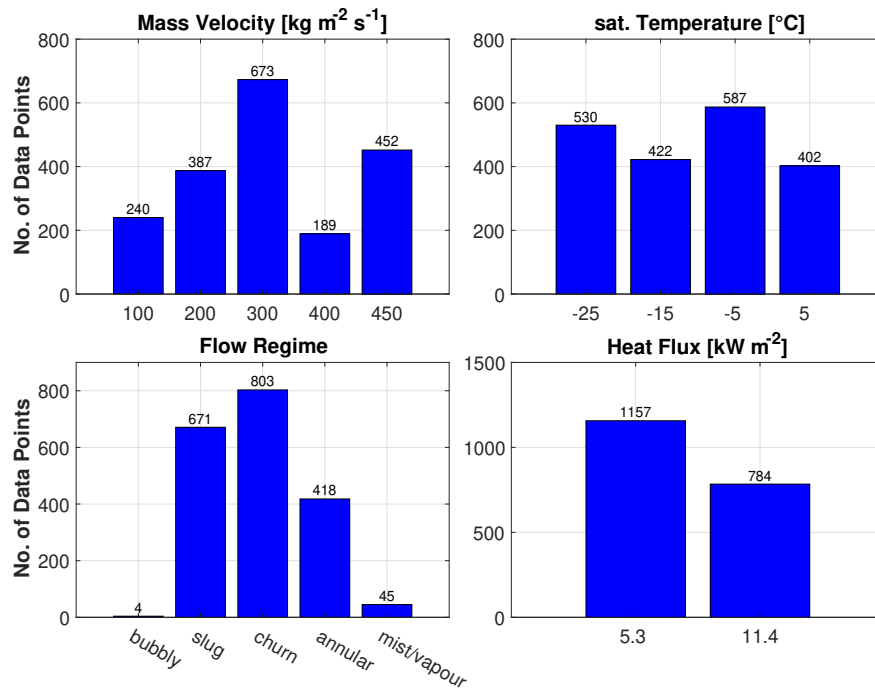


Figure 5.2 – Histograms describing the experimental heat transfer database for vertical upflow with regard to mass velocity, saturation temperature, heat flux and flow regimes.

5.3 Experimental Results and Influences of Flow Parameters

Knowledge about the influences of the flow parameters is crucial for understanding and predicting the heat transfer phenomena of evaporating flows. Figure 5.3 and Figure 5.4 illustrate the local experimental heat transfer coefficients derived from the measurements of the seven temperature probes mounted onto the evaporator at different heat fluxes, saturation temperatures and mass velocities. The errorbars indicate the uncertainties of the measurements, that are intrinsically related to the order of magnitude of the heat transfer coefficient and the heat flux. It can be noticed that the measurements reveal some scattering, what might be due to local differences between the probes. However, the measurements are within the ranges specified by the uncertainties.

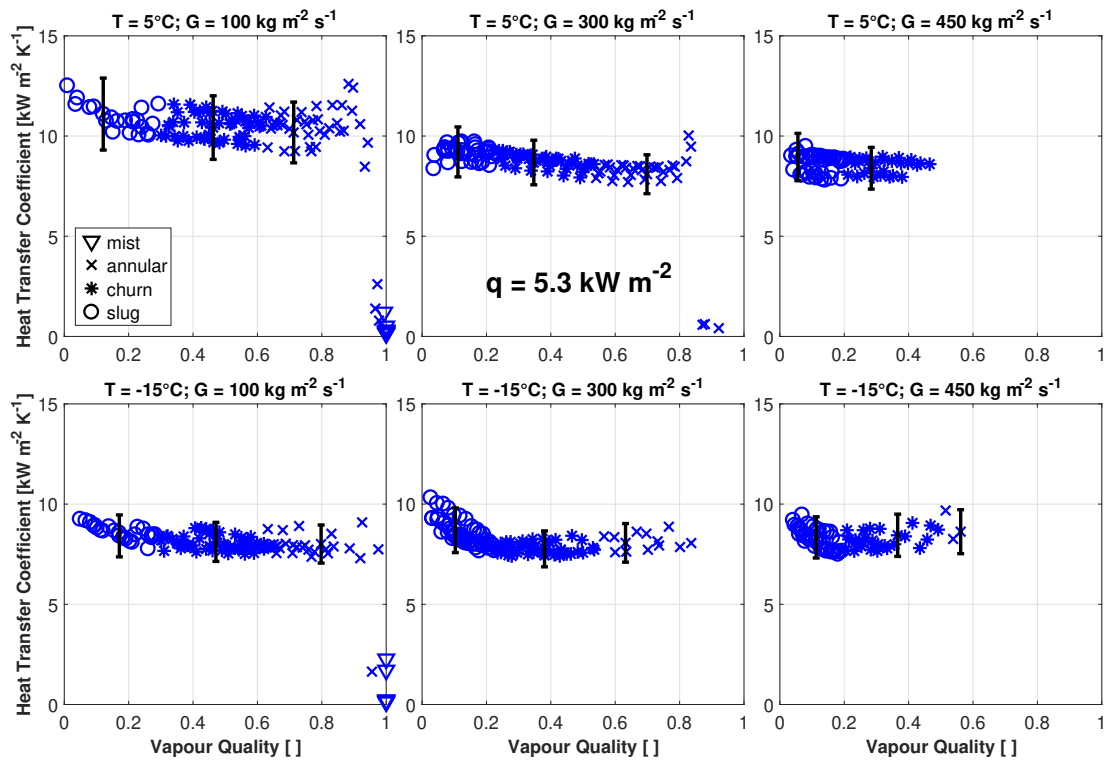


Figure 5.3 – Experimental heat transfer coefficients grouped according to saturation temperature and mass velocity, measured at a heat flux of $q = 5.3 \text{ kW m}^{-2}$. The errorbars indicate the uncertainties of the heat transfer measurements.

For a better evaluation of the influences of the parameters, the trends observed are illustrated with reduced data sets in Figures 5.5+5.6. In Figure 5.5, the heat transfer coefficients of the present study are illustrated over vapour quality, grouped according to saturation temperature and heat flux. Figure 5.6 presents the measurements grouped according to mass velocity and heat flux. It is noteworthy that the heat flux has a strong influence on the heat transfer characteristics of the CO_2 flow. Increasing heat fluxes result in enhanced heat transfer coefficients, especially at low vapour qualities, which leads to the conclusion that nucleate boiling is the dominating mechanism. The measurements show a pronounced heat transfer

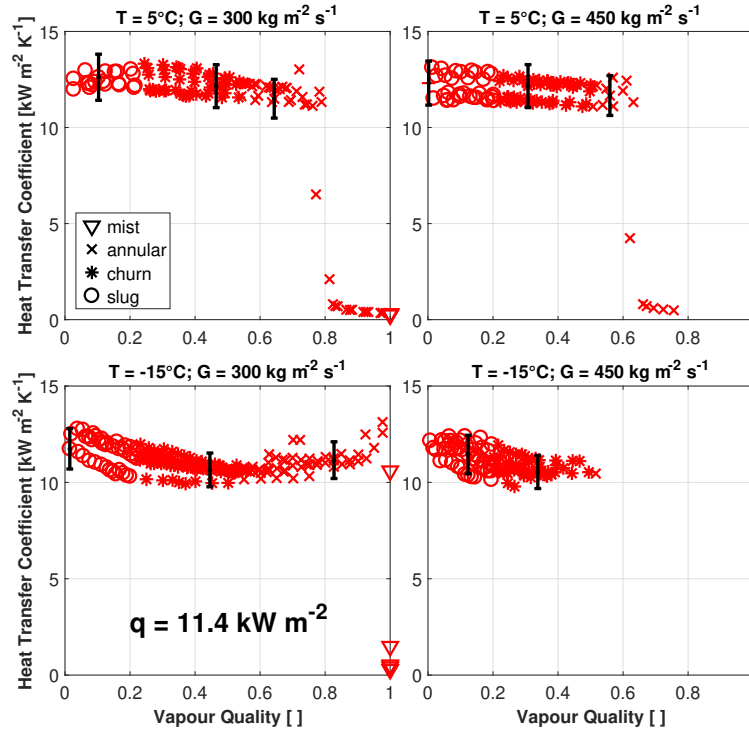


Figure 5.4 – Experimental heat transfer coefficients grouped according to saturation temperature and mass velocity, measured at a heat flux of $q = 11.4 \text{ kW m}^{-2}$. The errorbars indicate the uncertainties of the heat transfer measurements.

coefficient in the region of bubbly and slug flow that moderately decreases with increasing vapour quality, again pointing towards the fact that nucleate boiling is the governing heat transfer mechanism at low vapour qualities. However, most of the data sets covering the entire range of vapour quality from $0 \leq x \leq 1$ reveal enhanced heat transfer in the annular flow regime right before the steep fall-off. This is a clear hint that convective boiling is not entirely negligible and contributes, even though with a minor order importance, to the entire heat transfer mechanism. Mass velocity seems to have no crucial influence on the heat transfer coefficient, which substantiates the assumption that nucleate boiling is dominant and the convective contribution is less significant. The saturation temperature is observed to have a moderate impact on the heat transfer coefficients. In essence, the observations made based on Figures 5.5 + 5.6 are in agreement with the general understanding of flow boiling in macroscale channels and the observations reported in the literature on flow boiling of CO_2 in horizontal direction [74],[171]. Charnay et al. [173] summarized the typical trends observed in experimental studies on flow boiling heat transfer in macroscale tubes. According to their classification, the trends observed within the present study can be categorized as flow boiling of "type B" and "type C" typically observed in flows where nucleate boiling is dominant.

The sharp drop-off of the heat transfer coefficient at increased vapour qualities is a typical phenomenon observed in any kind of flow boiling due to the inception of dryout and the

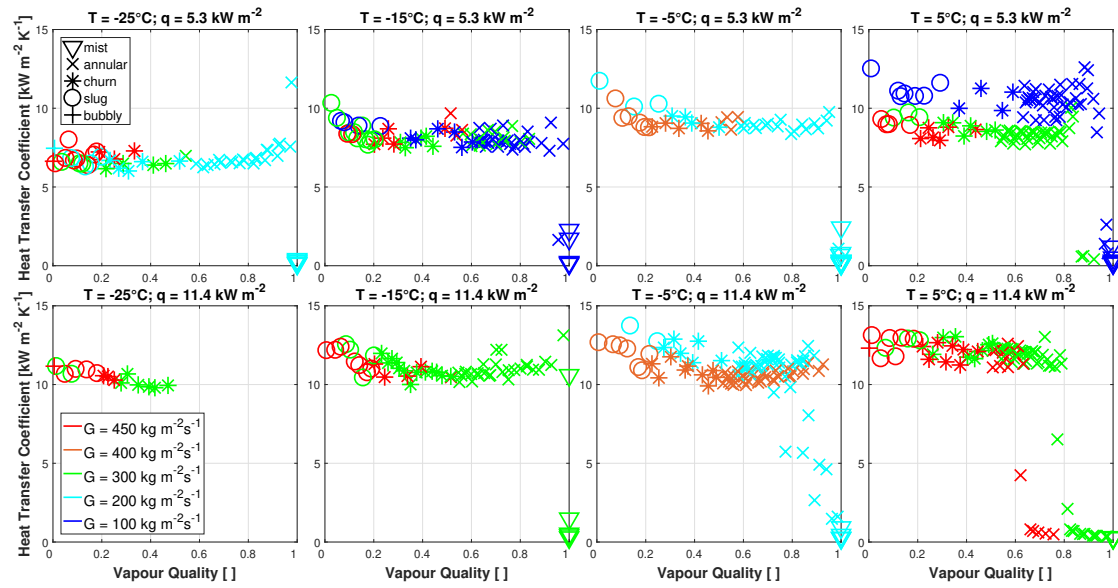


Figure 5.5 – Reduced data sets of experimental heat transfer coefficients versus vapour quality grouped according to the saturation temperature and the heat flux. Increasing saturation temperature from left to right, increasing heat flux from top to bottom.

reduced liquid film thickness in the annular flow regime, where nucleate boiling is suppressed. In evaporative flows of CO_2 , however, it is commonly observed that this phenomenon occurs at lower vapour qualities compared to other working fluids [74]. The heat transfer data of the present study show a shift of the sharp fall-off to lower vapour qualities with increasing saturation temperature, increasing mass velocity and increasing heat flux, which is fully in line with the observations reported in horizontal flow studies of CO_2 [167],[174]. Moreover, this corroborates with the conclusions made by Schmid et al. [134], where a shift of the flow pattern transitions to lower vapour qualities has been observed with increasing mass velocities in vertical upflow. The shift of the churn-to-annular flow pattern transition to lower vapour qualities consequently results in premature thinning of the annular liquid film. Thus, a shift of the nucleate boiling suppression to lower vapour qualities can be observed.

The heat transfer coefficients measured in vertical upward direction within the present work show comparable trends to the observations made in studies with horizontal flows of CO_2 . The measurements reported in [175],[168],[176] were carried out in horizontal pipes of similar tube diameters and flow conditions that are within the spectrum of the present test campaign. The data sets of all studies show high heat transfer coefficients at low vapour qualities that do not change significantly with varying vapour qualities and mass velocities. However, the heat transfer measurements recorded in vertical direction within the present study are about 20 % higher than the measurements performed in horizontal direction by Park and Hrnjak [175] and show an increase by a factor of ~ 2 compared to the horizontal data of Mastrullo et al. [168]. Increased heat transfer coefficients in vertical upward direction compared to horizontal flows corroborate with the observations made by Saisorn et al. [177].

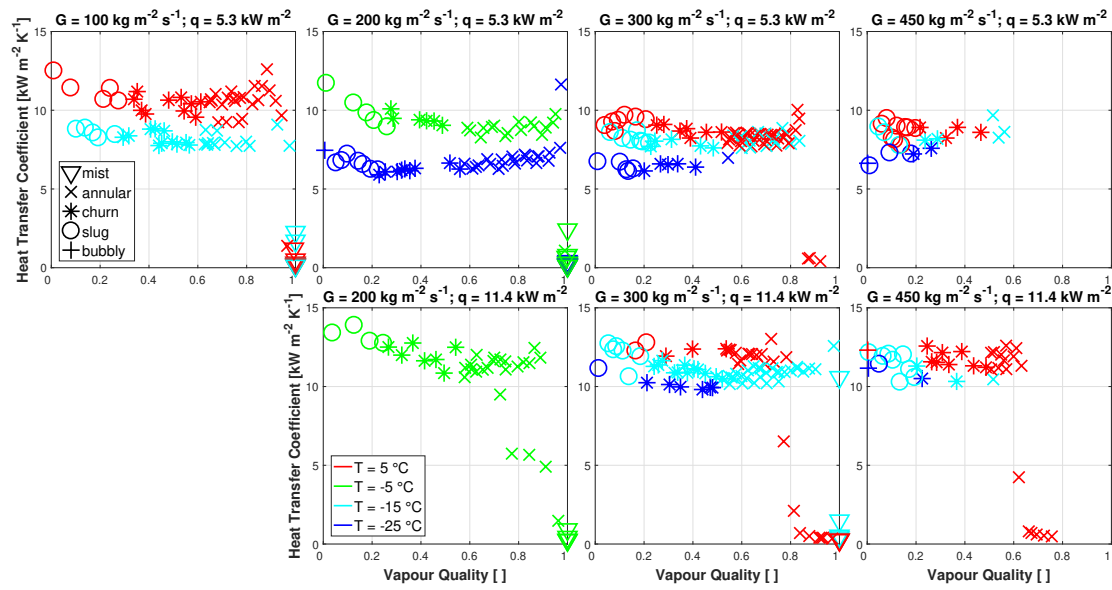


Figure 5.6 – Reduced data sets of experimental heat transfer coefficients versus vapour quality grouped according to the mass velocity and the heat flux. Increasing mass velocity from left to right, increasing heat flux from top to bottom.

5.4 Prediction of the Critical Vapour Quality

The sudden drop-off of the heat transfer coefficient identified in Figures 5.5 and 5.6 is of major interest in many engineering applications. Within the design phase of the cooling system of HEP experiments, for example, it is of particular significance to avoid conditions where the heat transfer coefficient is drastically reduced. Several studies proposed models to predict the inception and completion of dryout in horizontal two-phase flows of CO₂ [70],[72],[107]. These correlations, however, are not necessarily valid for vertical flows, since the dryout phenomena are significantly influenced by the pipe orientation. In horizontal flows, the onset of dryout appears at the top of the tube perimeter, since gravity acts perpendicular to the vector of motion. Contrary to this, the liquid film of vertical flows disappears symmetrically as reported by Schmid et al. [134]. The dryout inceptions within the present data set are determined by differentiating the experimental data with respect to vapour quality, according to

$$\left(\frac{\partial \alpha_{exp}}{\partial x} \right)_{p,T,q} \cdot \quad (5.3)$$

The limitations of the test facility do not allow encountering the dryout region throughout all set points of the test matrix. The test conditions, where the entire range of vapour quality is covered and the sharp fall-off of the heat transfer coefficient is observed, are shown in Figure 5.7.

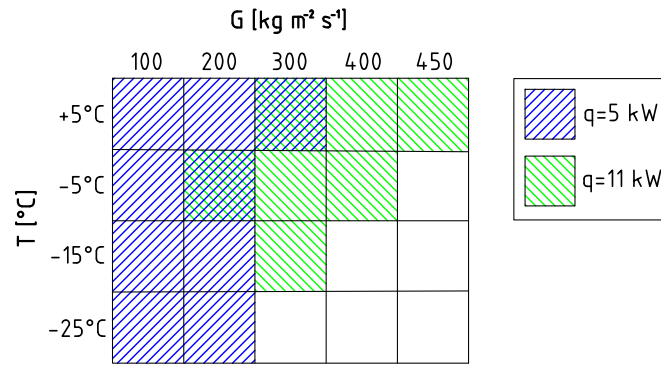


Figure 5.7 – Conditions where dryout is encountered within the present data set.

To incorporate the influences of the flow parameters on the dryout inception described in the previous section, the critical vapour quality can be modelled by means of non-dimensional numbers and quantities. The influence of the heat flux is considered in the boiling number and the effects of mass velocity are reflected by the Reynolds-, the Froude- and the Weber numbers. The Weber number considers the influence of the interface configuration between the two phases, while the Froude number takes the buoyancy effects into account. The impact of the saturation temperature is described by the reduced pressure and the fluid properties of the non-dimensional numbers. The critical vapour quality, where the onset of dryout develops,

is described by the following formula that is valid for the flow conditions specified in Figure 5.7.

$$x_{di} = 0.064 \cdot p_r^{-0.196} \cdot Re_{lo}^{0.155} \cdot Fr_{vo}^{-0.112} \cdot We_{vo}^{-0.226} \cdot Bo^{-0.294} \quad (5.4)$$

The constant and the exponents of Eq. 5.4 are determined with an optimization algorithm, based on an unconstrained multidimensional nonlinear minimization method. The root mean square error (RMSE), defined by the predicted values and the experimental data according to Eq. 5.3, is chosen as the target value to be minimized. The statistical comparison of the critical vapour qualities determined according to Eq. 5.4 and the experimental data points of the present study, where the onset of dryout occurs, reveals a mean percentage error (MPE) of 1.55 % and a mean absolute percentage error (MAPE) of 4.78 %.

5.5 Comparison of the experimental Heat Transfer Data to Prediction Models

Flow boiling phenomena are known to be a function of flow confinement and vary between micro- and macroscale channels [171]. The data recorded within the present study can be clearly attributed to the macroscale domain according the thresholds defined in [29],[30] and [31]. A key question in further analyzing the results is whether the trends can be properly captured by existing models. The experimental heat transfer data set of the present study is compared to the most commonly used macroscale correlations [155], [156], [158], [159], [160], [161], [162], [178], [179], that are valid for vertical upflow and/or in horizontal direction. The CO₂ specific flow boiling models by [107],[167],[174],[180] have been designed and validated exclusively with horizontal data and the studies of [174] and [180] can be attributed to the mini- and micro-channel domain. However, due to the lack of validated vertical correlations for CO₂, these models have been included in the analysis of the present data set, being aware that vertical macro-scale applications might go beyond their extent of validity. Concerning the heat transfer model of Cheng et al. [167], which is intrinsically related to the flow patterns defined in [72], only the correlations for the bubbly, slug, churn, annular and mist flow patterns, which have been observed in vertical flows by Schmid et al. [134], have been taken into consideration. Furthermore, the models by [181],[92],[182] are also included in the analysis, since the authors claim their validity for CO₂. In addition to the flow boiling correlations, the general pool boiling model of Cooper [183] has been considered, since the present CO₂ data set shows hints of a nucleate boiling dominance. Table 5.1 provides an overview of the experimental data in comparison to the prediction models. The analysis is subdivided and has been carried out with the entire, as well as the reduced data set excluding the dryout measurements according to Eq. 5.4. Table 5.2 presents the results grouped according to the local flow regimes.

Table 5.1 – Statistical comparison of the entire and the reduced experimental data set to the predicted heat transfer coefficients in chronological order.

#	all			without dryout data (Eq. 5.4)		
	1941			1751		
	MPE	MAPE	ξ	MPE	MAPE	ξ
Chen [155]	75.97	87.81	0.36	84.88	84.88	0.00
Shah [156]	50.47	78.38	0.41	67.17	67.17	0.00
Cooper [183]	-1.10	100.11	0.57	51.91	51.91	0.29
Gungor & Winterton [158]	5.20	69.33	8.60	38.34	38.34	9.08
Gungor & Winterton [160]	36.59	78.01	0.36	59.28	59.28	0.00
Liu & Winterton [159]	4.79	100.33	0.26	54.73	54.73	0.00
Jung et al. [178]	13.44	100.13	3.92	60.06	60.06	3.48
Kandlikar [161]; N_2	-10.39	42.55	67.34	8.83	20.45	73.90
Steiner & Taborek [162]	-95.74	120.75	69.19	6.02	20.84	71.39
Wattelet et al. [179]	-18.74	96.69	10.66	41.07	41.07	9.82
Yoon et al. [107]	-9.45	91.00	6.85	42.19	42.19	7.25
Yun et al. [180]	6.21	100.72	0.36	56.12	56.12	0.00
Cheng et al. [167]	13.97	52.16	24.16	34.48	34.52	23.13
Ducoulombier et al. [174]	-26.28	99.15	14.01	38.37	38.37	13.76
Fang et al. [92]	27.28	27.28	40.24	27.59	27.59	40.26
Shah [182]	13.07	91.48	0.36	54.25	54.25	0.00

The post-dryout heat transfer data are not predicted satisfactory by any model considered, what is substantiated by the poor performances within the annular and the mist/vapour flow regimes in Table 5.2. Therefore, the reduced data set excluding the dryout data according to Eq. 5.4 is more appropriate for evaluating the performances of the correlations.

Table 5.2 – Statistical comparison split up according to the flow patterns in chronological order.

Flow Pattern	bubbly			slug			churn			annular			mist/ vapour		
#	MPE	MAPE	ξ	MPE	MAPE	ξ	MPE	MAPE	ξ	MPE	MAPE	ξ	MPE	MAPE	ξ
Chen [155]	81.70	81.70	0.00	87.86	87.86	0.00	83.32	83.32	0.00	64.35	90.02	0.96	-125.08	147.23	6.67
Shah [156]	74.62	74.62	0.00	74.13	74.13	0.00	63.20	63.20	0.00	25.58	89.25	0.96	-300.26	311.89	8.89
Cooper [183]	53.13	53.13	0.00	54.21	54.21	0.00	50.46	50.46	0.25	-24.21	114.80	2.15	-1536.01	1538.18	0.00
Gungor & Winterton [158]	39.15	39.15	0.00	38.24	38.24	11.03	37.19	37.19	10.34	-12.44	91.72	1.67	-897.69	901.15	6.67
Gungor & Winterton [160]	65.18	65.18	0.00	60.56	60.56	0.00	57.39	57.39	0.00	25.82	89.35	0.96	-594.67	601.72	6.67
Liu & Winterton [159]	58.21	58.21	0.00	55.12	55.12	0.00	53.50	53.50	0.00	-4.45	108.73	1.20	-1533.79	1535.96	0.00
Jung et al. [178]	63.85	63.85	25.00	69.92	69.92	0.00	55.90	55.90	2.62	-10.92	97.64	12.68	-1364.52	1366.50	2.22
Kandlikar [161]; N_2	-23.66	25.17	75.00	-6.96	15.90	90.46	11.50	17.48	78.58	-5.69	84.05	15.55	-494.69	503.26	2.22
Steiner & Taborek [162]	19.05	36.60	25.00	12.97	24.69	59.02	2.53	18.68	80.07	-154.95	169.27	72.25	-2930.34	2931.14	2.22
Wattelet et al. [179]	50.58	50.58	0.00	46.32	46.32	2.53	38.18	38.18	11.58	-47.63	113.03	23.21	-1742.32	1744.13	0.00
Yoon et al. [107]	44.20	44.20	0.00	38.81	38.81	14.46	42.55	42.55	3.74	-22.98	112.48	1.44	-1536.00	1538.17	0.00
Yun et al. [180]	58.91	58.91	0.00	58.71	58.71	0.00	54.57	54.57	0.00	-18.69	115.70	1.44	-1412.91	1415.25	2.22
Cheng et al. [167]	40.72	40.72	25.00	39.63	39.63	8.64	31.78	31.78	28.14	-52.67	105.65	41.87	-69.79	106.66	20.00
Ducoulombier et al. [174]	40.97	40.97	25.00	42.25	42.25	6.86	37.01	37.01	13.82	-53.01	112.64	27.27	-1934.96	1936.62	0.00
Fang et al. [92]	30.86	30.86	0.00	28.07	28.07	32.34	27.66	27.66	42.96	26.40	26.40	44.02	16.76	16.76	77.78
Shah [182]	48.18	48.18	0.00	55.52	55.52	0.00	52.29	52.29	0.00	13.99	91.20	1.20	-1331.45	1333.17	4.44

The statistical comparison presented in Table 5.1 reveals that none of the models provides a satisfactory prediction of the measurements and the correlations generally underpredict the heat transfer coefficients of the reduced data set, indicated by $MPEs > 0$. In particular the general flow boiling methods [155], [156], [158], [159], [160], [178], [179], designed with data from conventional synthetic refrigerants, anticipate reduced heat transfer coefficients compared to the present CO_2 data. This trend is illustrated – representatively for all general prediction methods – in Figure 5.8 and corroborates the general opinion that CO_2 has enhanced heat

transfer properties compared to conventional working fluids [175],[74]. The comparison of the data to the classical pool boiling method of Cooper [183] in Figure 5.8 confirms the idea that the nucleate boiling contribution is increased in two-phase flows of CO₂ and therefore supports the general approaches of incorporating correction factors for the nucleate and the convective boiling contribution. Moreover, the statistical comparison reveals that only the prediction methods of Kandlikar [161] – by considering the fluid-dependent parameter defined for the use of nitrogen (N₂), since all the other values result in an underprediction – and Steiner & Taborek [162] yield a MAPE in the order of ~ 20 % and predict ~ 70 % of the data points within an error band of ± 30 %. However, the prediction method of Kandlikar [161] shows a high scattering with no clear trends of under- or overpredicting. The asymptotic model of Steiner & Taborek [162], illustrated in Figure 5.8, shows reduced scattering compared to the method of Kandlikar [30], however, not always capturing the trends of CO₂ satisfactory.

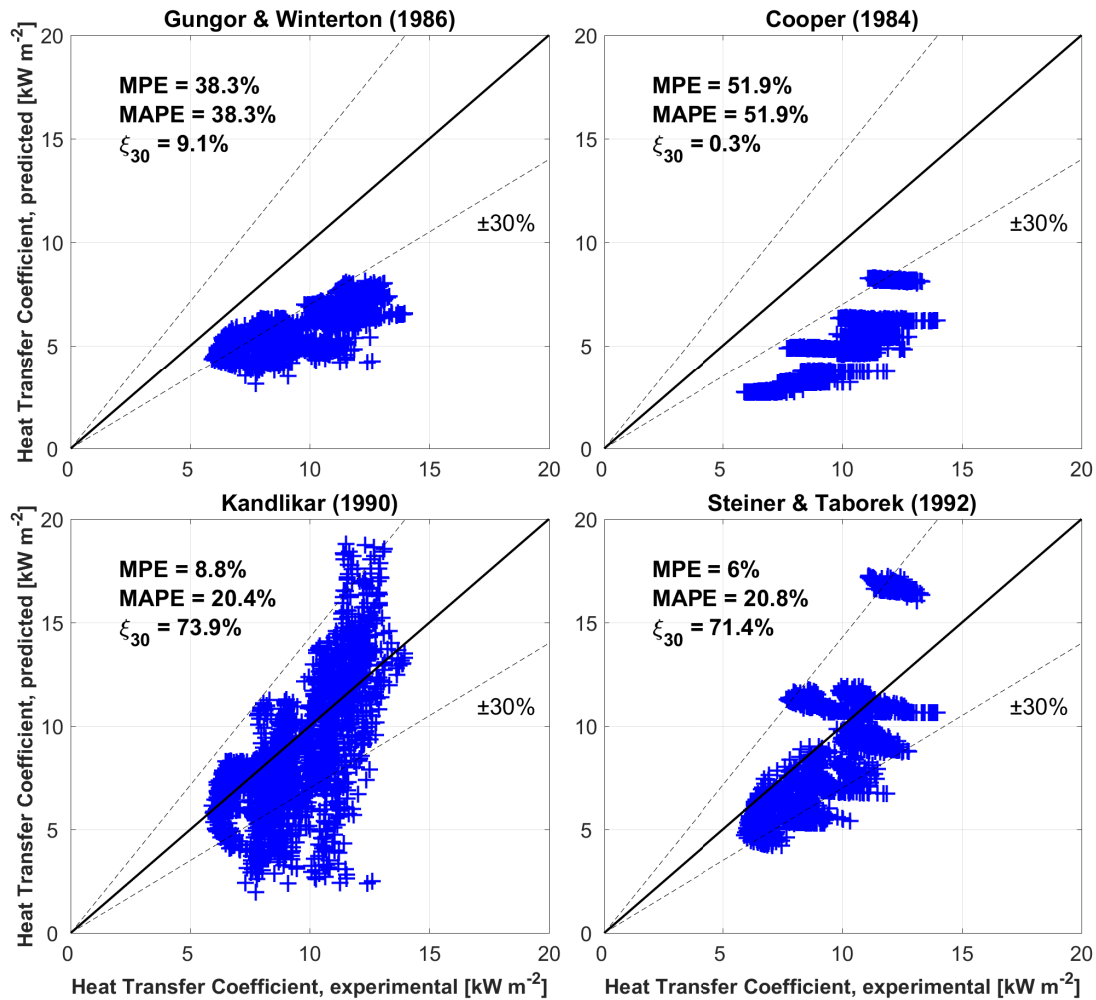


Figure 5.8 – Comparison of the reduced data set, excluding the dryout data, to several heat transfer models.

The CO₂ models of Cheng et al. [167] and Ducoulombier et al. [174], presented in Figure 5.9, underpredict the vertical data set of the present study. Both, however, were designed for horizontal applications only. In a similar manner, also the general correlations by Fang et al. [92] and Shah [182] underpredict the present vertical data set. These models were developed and validated with large databases, containing also horizontal data for CO₂.

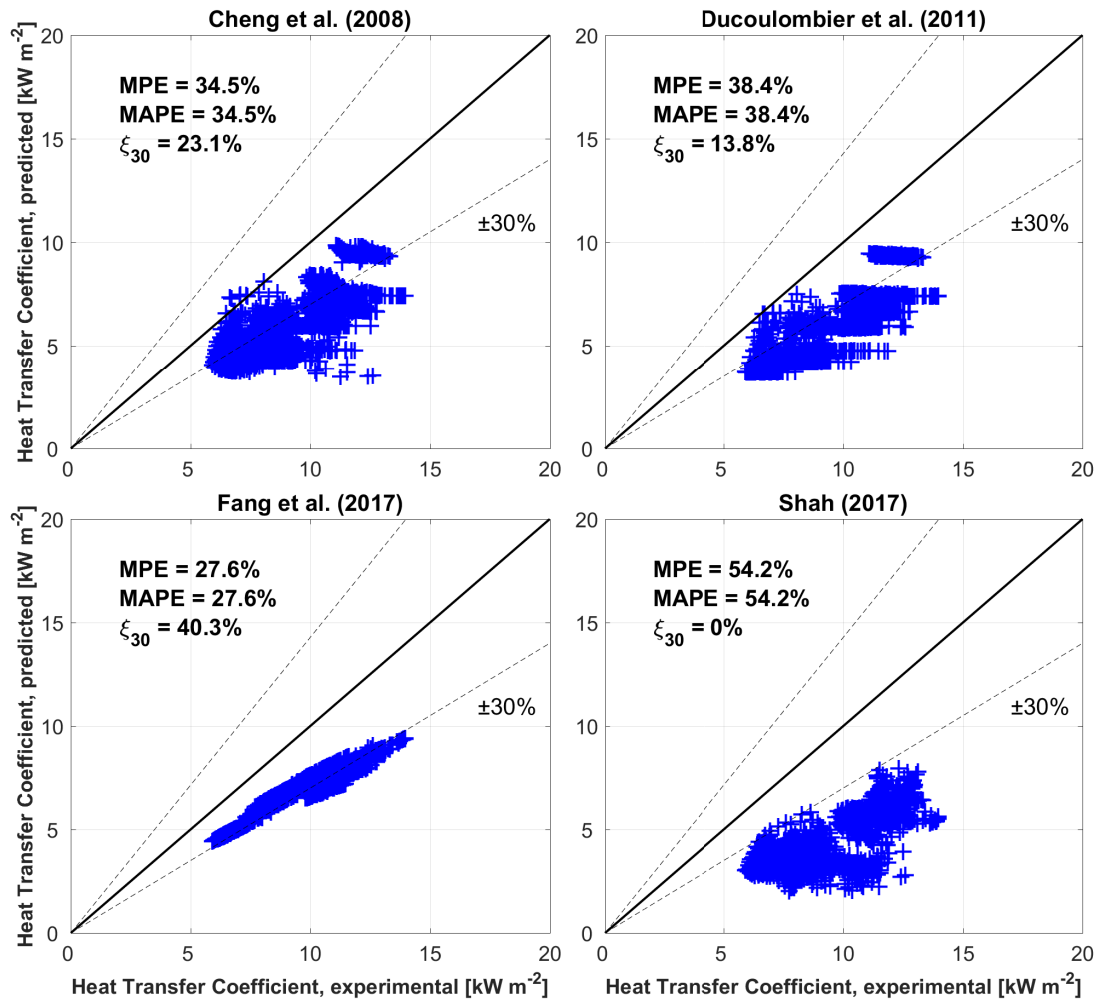


Figure 5.9 – Comparison of the reduced data set, excluding the dryout data, to several heat transfer models developed with databases including horizontal data of CO₂.

In general, the experimental data of the present study consistently exceed the predicted values of the established heat transfer models for CO₂ and the conclusions drawn by [177] point towards the idea that the offset can be explained by the change of the flow direction. Based on the observed increase of the heat transfer coefficients in vertical upward direction and the fact, that the existing prediction models have only been validated with horizontal data of CO₂, a correction of the horizontal predictions by a linear factor is assumed to be an efficient approach to properly predict the heat transfer properties of vertical two-phase flow of CO₂. Therefore, a correction factor is proposed for the well-established models of Cheng et al.

[167] and Fang et al. [92] to predict the increased heat transfer properties in vertical upward direction according to

$$\alpha_{up} = \alpha_{hor} \cdot F_{up}. \quad (5.5)$$

The heat transfer enhancement multiplier for vertical upflow F_{up} is determined to be 1.4915 for the model of Cheng et al. [167] and 1.3948 for the model of Fang et al. [92] respectively. Figure 5.10 presents the predicted heat transfer coefficients corrected by the respective multipliers.

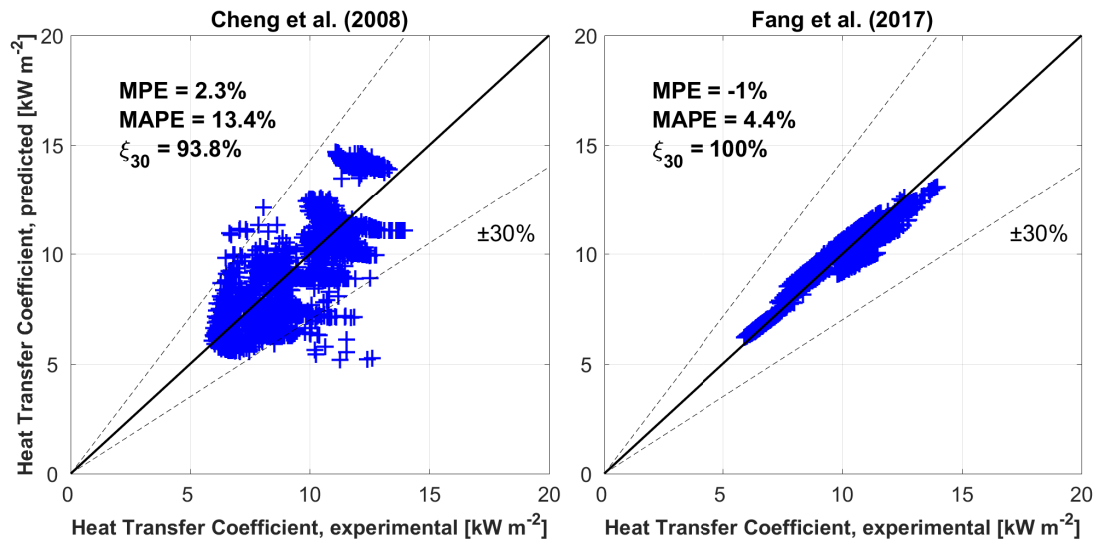


Figure 5.10 – Comparison of the reduced data set, excluding the dryout data, to the prediction models corrected by the enhancement factor for vertical upflow.

5.6 Conclusion

Heat transfer measurements of flow boiling CO₂ have been carried out in vertical upward direction in a test section of 8 m length and an inner pipe diameter of 8 mm. The measurements were conducted with several temperature probes mounted at different locations onto the outer perimeter of the evaporator and a database of 1941 measurements has been compiled. The heat transfer mechanism shows typical signs of a nucleate boiling dominance, where the heat flux has a strong influence on the heat transfer coefficient, while the saturation temperature has a moderate impact. On the other hand, the influence of the mass velocity – and hence the convective boiling contribution – seems to be of minor importance. In general, the CO₂ heat transfer measurements of the present study confirm the trends observed in horizontal CO₂ flow boiling, where the heat transfer properties are enhanced compared to most commonly used working fluids.

The onset of dryout, characterized by a sharp reduction of the heat transfer coefficient, is observed to be a function of the saturation temperature, the mass velocity, the vapour quality and the heat flux. For predicting the critical vapour quality where the onset of dryout occurs, a dryout inception model is suggested that incorporates the crucial flow parameters and captures the experimental dryout inception data of the present study with an accuracy of MPE = 1.55 % and MAPE = 4.78 % respectively.

The comparison of the reduced experimental data set, excluding the post-dryout measurements according to the suggested dryout inception model, reveals that the heat transfer measurements are underpredicted by all models considered. In particular the prediction methods designed and validated with synthetic working fluids underperform the data of the present study. This substantiates the general understanding that CO₂ has increased heat transfer properties compared to synthetic working fluids. However, also the horizontal prediction models specifically designed for CO₂ underpredict the vertical data set of the present study. This corroborates the idea that heat transfer coefficients are a function of the flow direction and are generally enhanced in vertical upflow. To incorporate the increasing heat transfer coefficients of CO₂ in vertical upward direction, heat transfer enhancement factors are suggested for the prediction models of Cheng et al. [167] and Fang et al. [92].

The general lack of vertical heat transfer measurements of CO₂ can be motivation for future studies to increase the present data set by going beyond the experimental conditions with regard to saturation temperature, mass velocity, tube diameter and channel geometry. Furthermore, it is recommended to envisage the development of a heat transfer model that is valid for flow boiling of CO₂ in any flow direction.

6 Epilogue

6.1 Summary and Conclusion

The demand for refrigeration appliances with constantly increasing capacities consolidates the trend towards evaporative cooling concepts in many applications. Triggered by ambitious objectives on climate protection, an increasing interest in natural refrigerants can be observed within the recent years. Carbon Dioxide has recently been gaining renewed interest and has already proven good performance in multiple refrigeration appliances in both scientific and industrial facilities. Driven by the positive experiences obtained from several refrigeration systems in the recent years, CERN decided to use CO₂ as the working fluid for the thermal management of the future Particle Tracker Detectors in the ATLAS and CMS experiments. As a consequence, a comprehensive research program has been launched to better understand the two-phase flow behaviour and cooling properties of CO₂.

Within the scope of the present work, a test facility for investigating the two-phase flow phenomena of CO₂ has been built. The rig comprises macro-scale test sections with horizontal, vertical up- and downflow orientations made of stainless steel tubes of 8 mm inner diameter. The test setup is connected to a refrigeration unit that provides flow conditions in the range of $16 \text{ bar} \leq p_{\text{sat}} \leq 40 \text{ bar}$; $-26.5 \text{ }^{\circ}\text{C} \leq T_{\text{sat}} \leq +5.3 \text{ }^{\circ}\text{C}$ and mass flow rates resulting in mass velocities from $100 \text{ kg m}^{-2} \text{ s}^{-1} \leq G \leq 450 \text{ kg m}^{-2} \text{ s}^{-1}$.

Flow Patterns

Prediction methods taking the geometrical structures of the concurrent liquid and vapour phases into account have proven to achieve better performances in predicting the flow behaviour of multiphase flows. Inspired by this fact, two transparent sections are installed at ground level of the vertical test sections to allow flow visualization. Flow pattern observations of vertical up- and downflow have been recorded with a high-speed camera and a database of 431 observations in upward direction and 123 in downward direction has been compiled. The records have been analyzed with a Frame- and Flow-Regime Classifier that has been built

in a side project by making use of computer vision and machine learning techniques. The results of the experimental observations in vertical directions have been compared to existing flow pattern maps. None of the existing charts was able to predict the experimental flow pattern transitions properly, what might be due to the fact that the majority of the existing flow pattern maps for vertical orientations is mainly based on data sets of mixtures. Thus, it is questionable whether such charts are generally capable to capture the flow regime transitions of pure working fluids at saturated conditions. Another explanation for the deviations to existing maps can be found in the different thermophysical properties of CO₂, e.g. the ratios of the liquid-to-vapour viscosities and densities, that significantly differ to the ones of many commonly used working fluids. For that reason, the outcome of the flow pattern observations of the present work are condensed in novel correlations to describe the flow pattern transitions and new flow pattern maps for vertical up- and downflow of CO₂ are presented.

Pressure Drop

Pressure drop is one of the key factors that has to be accurately taken into consideration in the design phase of refrigeration systems. In particular within the scope of High Energy Physics experiments, where the detectors are positioned in shielded areas far from their ancillary service systems, the pressure drop of the two-phase flow is paramount since it directly influences the saturation conditions and the temperature budget on the detector side. Miscalculation might lead to severe consequences, like a reduced detector performance or, in a worst case scenario, a thermal runaway. The pressure drop phenomena of CO₂ have been investigated in horizontal, vertical up- and downflow with the test rig of the present work. Data sets of 512 measurements in horizontal and 295 records in each of the vertical flow directions have been compiled and compared to existing prediction models. The horizontal data points have been compared to 18 frictional pressure drop models. For the comparison of the vertical data sets, the 18 models for frictional pressure drop have been combined with 21 void fraction correlations accounting for the static head. This results in 378 factorial combinations for anticipating vertical pressure losses. The best models were highlighted for each flow orientation. Furthermore a subdivided analysis split up according to the flow regimes has been carried out and the most accurate solutions have been identified. In general, the data sets of the horizontal and the vertical upflow pressure drop measurements are predicted by several models with an acceptable accuracy. However, the performance of the pressure drop models decrease drastically for the downflow data and deviations in the prediction of void fraction are identified as possible reasons for the reduced accuracies.

Heat Transfer Coefficient

Besides pressure drop, a sound understanding of the heat transfer characteristics of refrigerants is key for the development of refrigeration cycles. The lack of heat transfer measurements in vertical flow directions of CO₂ was motivation to investigate the heat exchanging properties in vertical upward direction with the present test rig by means of the Joule effect. Diabatic

tests with heat fluxes in the order of ~ 5 and $\sim 11 \text{ kW m}^{-2}$ respectively have been carried out and a data set of more than 1900 measurements has been compiled. Within the analysis of the recorded data, the characteristic drop-off of the heat transfer coefficient at increased vapour qualities can be observed, what is a typical hint for the onset of dryout in flow boiling applications. To avoid scenarios with reduced cooling properties during operation, a dryout inception model has been suggested to predict the critical vapour quality, where the heat transfer coefficient sharply decreases. The experimental data points – excluding the data of the dryout region – have been compared to established heat transfer correlations. It can be concluded that all the evaluated models underpredict the measurements and that the heat transfer characteristics of vertical CO_2 upflow are generally increased compared to horizontal applications. As a consequence, an enhancement factor for two existing prediction models has been suggested to account for the increased flow boiling properties of CO_2 in vertical upward direction.

Global Conclusion of the present Work

The investigations carried out within the present work strengthen the general idea that CO_2 has great potential for future cooling applications in many domains. The high heat transfer coefficients allow very efficient and compact refrigeration concepts on a wide temperature range. Due to its dielectricity, CO_2 is particularly suitable for the thermal management of electronic components and the radiation hardness make it an excellent candidate for equipment in highly radiated environments, which is a disqualifying criterion for the popular and often used Hydrofluorocarbons (HFC) R134A or the blend R404A. Furthermore, the reduced temperature gradients due to pressure drop – the temperature glide – combined with enhanced heat transfer characteristics, make CO_2 it superior to Perfluorocarbons (PFC) that are commonly used in the cooling systems of the current Particle Trackers of ATLAS and CMS. The present work provides engineering guidelines for designing evaporative cooling systems with CO_2 and can serve as a baseline of further research topics.

6.2 Outlook and Prospects

Needless to mention that there is plenty of potential to further investigate the two-phase flow characteristics of CO_2 beyond the present work in every respect, in particular in vertical and inclined tube orientations. However, some suggestions are made in this section and the following outlook lists the measures according the efforts implied.

Further Potential of the present Setup

Many sections of the rig are not accessible due to space restrictions and retrofit upgrades are not possible without dismantling large parts of the system, especially at the vertical test

sections that have an elevation of ~ 10 m. For that reason, additional instrumentation (to the ones used and presented within the present work) has been considered from the very early stages of the conceptual design phase. Thus, additional heat transfer measurements at the horizontal and vertical downflow test section are feasible right away and do not require any modification of the test facility.

Furthermore, it seems logical to increase the size of the data sets presented within the present work to increase the statistical significance of the presented results. In particular additional flow pattern observations in downward direction can contribute to an increased accuracy of the flow pattern map presented for vertical downflow and swapping one of the transparent sections to the horizontal test section allows horizontal flow pattern observations in 8 mm tubes.

Additional Potential with moderate Changes of the present Setup

Extending the test conditions beyond the limitations of the present study is certainly a desirable objective to either (i) confirm the validity of the results and correlations postulated within the present work for an increased range of conditions, or (ii) to adapt the results of the present work accordingly. The test conditions of the current facility are mainly limited by the capacity of the refrigeration unit. Extending the experimental domain towards lower temperatures and higher mass velocities can be realized by replacing the cooling plant or by simply connecting the test rig to an other system, e.g. to the new DEMO-refrigeration-prototype currently developed by the EP-DT-FS group at CERN. The DEMO prototype provides temperatures down to -50 °C and allows mass flow rates up to 1.5 kg s^{-1} , increasing the range of mass velocity by a factor of ~ 60 .

For extending the temperature range towards warmer conditions, either (i) the glass tubes inside the transparent sections have to be adapted according the increase in pressure, or (ii) the transparent sections have to be disconnected or bypassed to protect them from elevated pressures.

Additional Research Potential beyond the Possibilities of the present Setup

The topic of flow boiling CO_2 – and natural refrigerants in general, like Krypton for example – provides a huge potential for further investigations on their two-phase flow characteristics. Within CERN's area of interest it is for sure worth considering further studies in different pipe sizes and geometries. To increase the accuracy of the calculations carried out within the design phase of the transfer lines for the future Particle Trackers, it is certainly worth considering additional studies in different pipe geometries, like concentric annuli for example. Furthermore, with regard to the detector design, it is recommended to investigate the flow boiling phenomena in inclined and vertical evaporator lines with reduced diameters that are approaching the criteria of flow confinement.



Appendix

A: Accuracy and Uncertainties

The values obtained with measurement procedures cannot be categorized as fundamentally true or false. All measurements contain errors and deviate from their true value. DIN 1319 [184] defines the error of measurements the following:

$$\text{Error of Measurement } E = \text{Result of Measurement } X_e - \text{True Value } X \quad (1)$$

In general, the error of a measurement is difficult to determine since it requires the knowledge of the true value. Therefore, it is more practical to evaluate an interval in which the true value is likely to occur, what is defined as the uncertainty of a measurement [185]. Within the present work, an emphasis has been put on the thorough calibration of the instrumentation in order to get most accurate results possible. In the following sections, the accuracies and uncertainties of the instrumentation of the test facility, the measurement procedures and the derived properties are summarized.

A.1 Error Propagation

Derived properties are influenced by the errors of their factors. Due to the concatenation of the quantities involved, the propagation of errors and uncertainties have to be taken into consideration. Erven and Schwägerl [186] describe the propagation of uncertainties as follows

$$|df| = \sum_{i=1}^n \left| \frac{\partial f}{\partial x_i} (x_1, \dots, x_n) \cdot dx_i \right| \leq \sum_{i=1}^n \left| \frac{\partial f}{\partial x_i} (x_1, \dots, x_n) \right| \cdot |dx_i|. \quad (2)$$

The latter expression of Eq. 2, representing the limit of the deviation when considering dx_i being the absolute error Δx_i – which is usually rather easy to determine – can be seen as maximum of the error function. Hence, Eq. 3 – in this case illustrated with two factors involved – can be considered as being the “conservative” formulation of the propagation of

errors or uncertainties.

$$|\Delta f_{\max}| = \left| \frac{\partial f}{\partial x_1}(x_1, x_2) \right| \cdot \Delta x_1 + \left| \frac{\partial f}{\partial x_2}(x_1, x_2) \right| \cdot \Delta x_2 \quad (3)$$

Many problems, however, are influenced by physically distinct quantities that are independent of each other and are determined by entirely different processes. Thus, a correlation between the sources of errors related to the different quantities is almost inconceivable. Taylor [187] in this case suggests the addition in quadrature according to Eq. 4 that provides smaller uncertainties than the simple sum of the original errors. This method is appropriate in the case where the various uncertainties are independent and random, since there is a good chance of partial cancellation of the errors. The error defined in Eq. 3 can be interpreted as the "worst case" scenario.

$$\delta f = \sqrt{\left(\frac{\partial f}{\partial x_1} \delta x_1 \right)^2 + \dots + \left(\frac{\partial f}{\partial x_i} \delta x_i \right)^2} \quad (4)$$

In the present work, both methods are applied, depending on the respective scenario, the magnitude of the factor's influence on the final result and the complexity of the calculation method.

A.2 Uncertainties of Instrumentation and Measurements

A.2.1 Temperature

All temperature probes of the present test facility are calibrated prior to installation. The reference measurement throughout the calibration cycles is provided by a calibrated *FLUKE 5626* Platinum Resistance Thermometer that is integrated into the DAQ of the test facility. The uncertainty of the reference probe according to the calibration certificates is

$$\Delta T_{ref} = \pm 0.004 \text{ } ^\circ\text{C at } 0 \text{ } ^\circ\text{C}.$$

The temperature probes have been calibrated over the entire field of data collection, ranging from ambient lab conditions down to the lowest temperature the test facility is able to provide ($-30 \text{ } ^\circ\text{C} \leq T_{\text{sat}} \leq +25 \text{ } ^\circ\text{C}$). The thermal conditions during the calibration procedure are provided by a temperature-controlled bath of a *LAUDA RK20 KS* chiller and the calibration cycles are carried out in steps of 5 K, starting from the highest to the lowest temperature and vice versa, for checking the hysteresis effects. To moderate the influences of disturbances, like instabilities of the temperature source for example, the probes are placed in close proximity to

the reference probe inside a copper block that provides a certain thermal inertia. The copper block is largely immersed into the glycol of the temperature-controlled bath, as illustrated in Figure 1.

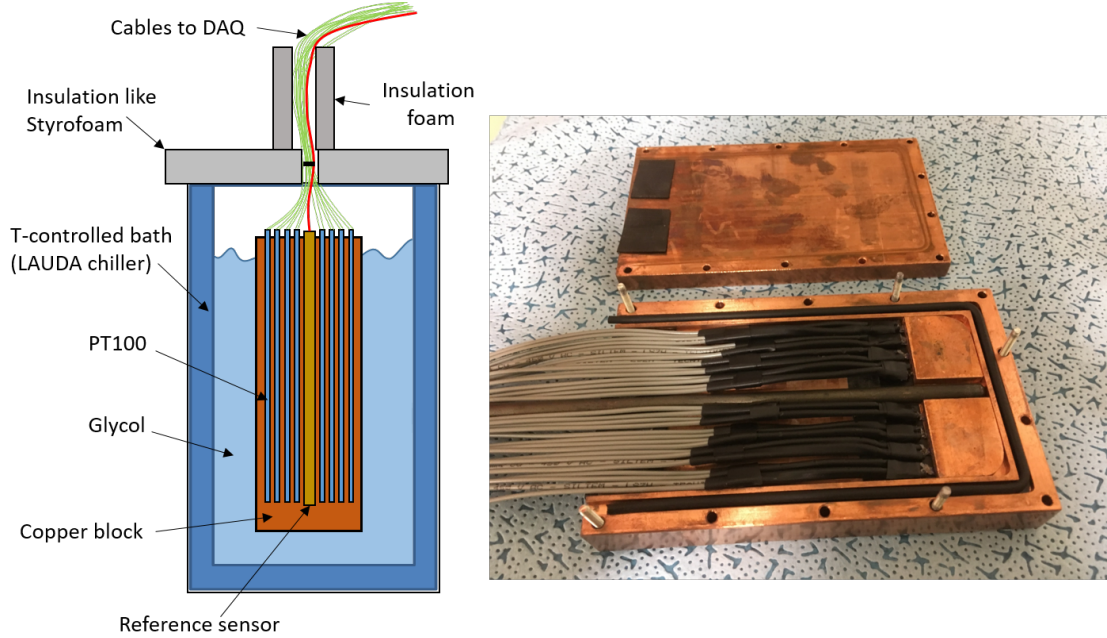


Figure 1 – T-probe calibration with a temperature-controlled bath (left). The T-probes are placed inside a copper block next to the reference sensor (right).

The measured values of the temperature probes are correlated to the reference value by means of correction functions, that are determined with a least-square regression. Third order polynomials according to Eq. 5 are found to provide reasonable accuracy.

$$T_{cor,i} = a \cdot T_{meas,i}^3 + b \cdot T_{meas,i}^2 + c \cdot T_{meas,i} + d \quad (5)$$

The individual correction formulae for all temperature probes are implemented into the PLC logic of the DAQ system and both the initial measurements as well as corrected values are archived. Figure 2 shows some temperature measurements just before and right after the implementation of the correction formulae.

The correction measures are validated with sanity checks. The statistical evaluation of the pre- and post- calibrated measurements – presented in Figure 3 based on the characteristics of T-probe TT2A60 – reveal a significant improvement in accuracy.

The final accuracy of the calibrated temperature probes is described by the absolute error determined with several sanity checks and by taking the accuracy of the reference probe into account. Finally, all temperature probes are within an accuracy of

$$\Delta T = \pm 55 \text{ mK.}$$

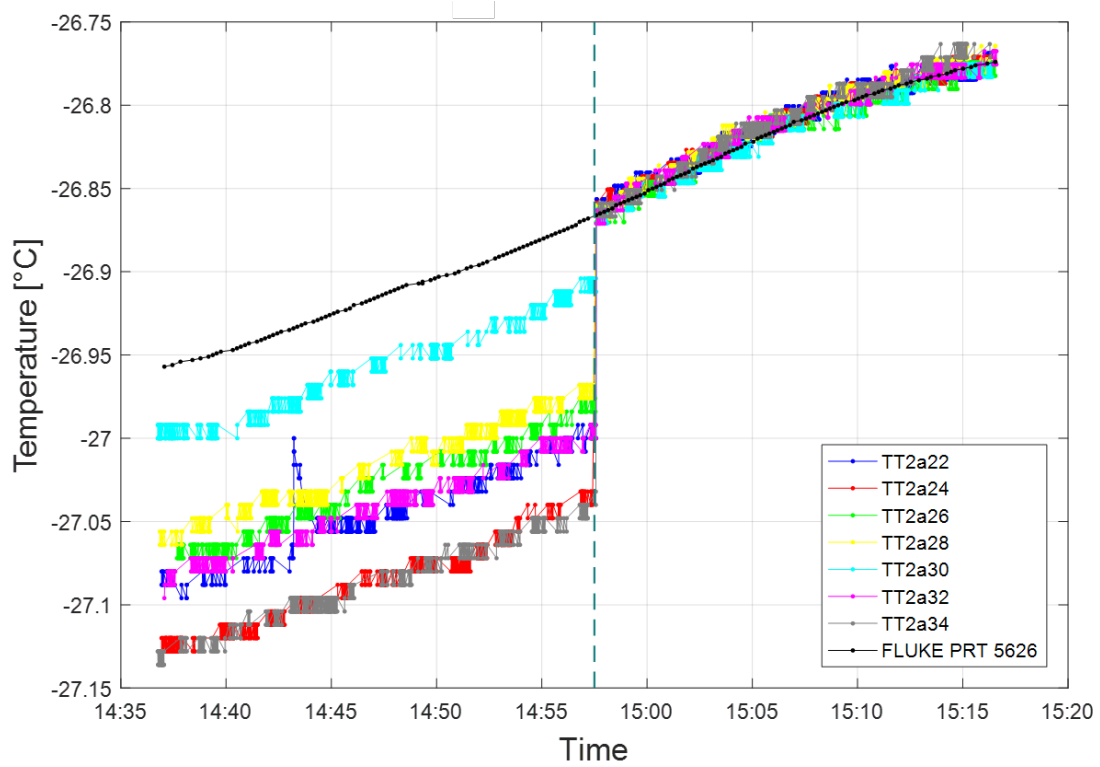


Figure 2 – Pre- and post-calibration measurements.

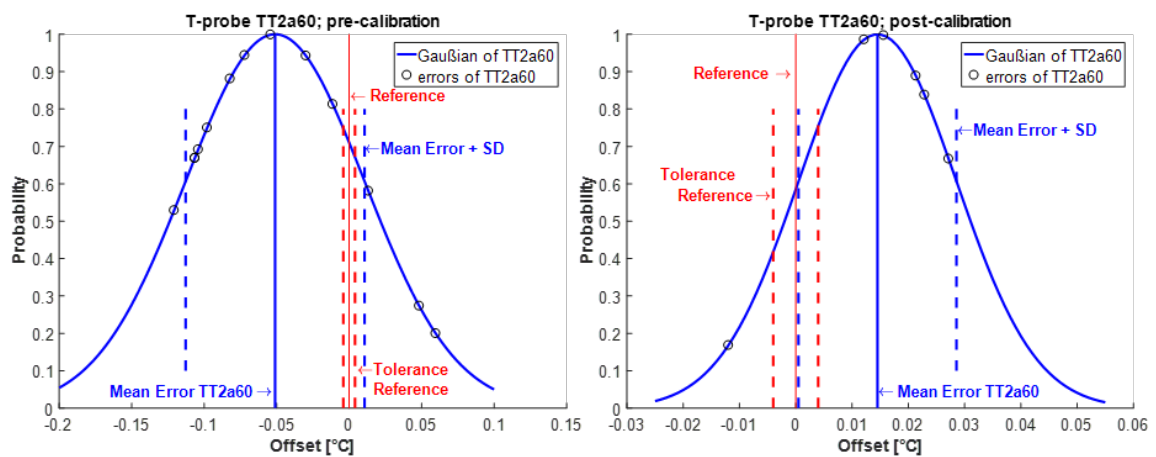


Figure 3 – Statistical evaluation of temperature measurements before (left) and after calibration (right). Illustration based on measurements of T-probe TT2A60.

A: Accuracy and Uncertainties

A.2.2 Pressure

The test facility is equipped with two different types of absolute pressure transmitters that are listed in Table 1. The absolute pressure transmitters from *KELLER* are located at the in- and outlets of the three test sections, the ones from *GE DRUCK* are installed before and after the pre- and post-heaters.

Table 1 – Specifications of the absolute pressure transmitters installed in the test facility.

Brand	Series-No	Range	Output	Accuracy	Type
KELLER	PAA-33X	0...100 bar abs	4...20 mA	±0.1 % Full Span	absolute
GE DRUCK	PTX 7500	0...100 bar abs	4...20 mA	±0.1 % Full Span	sealed gauge

In addition to the absolute pressure measurements, the test sections are equipped with differential pressure transmitters *Deltabar S PMD75* from *Endress+Hauser*. The specifications of the differential pressure transmitters provided by the supplier are listed in Table 2.

Table 2 – Specifications of the differential pressure transmitters installed at the test sections.

Test Section	Series	Type	Sensor Range	max. Error
Horizontal	Deltabar PMD75	PMD75-AAD7F11BYAA	−500...500 mbar	±0.05 %
Vertical Up	Deltabar PMD75	PMD75-AAD7H11BYAA	−3...3 bar	±0.05 %
Vertical Down	Deltabar PMD75	PMD75-AAD7H11BYAA	−3...3 bar	±0.05 %

The calibration procedure of the pressure transmitters is similar to the one applied for the temperature probes previously described in section A.2.1. A deadweight tester is used to provide the reference pressure and the transmitters are connected via a manifold as shown in Figure 4. The individual correction formulae have been determined with a data regression based on a least-squares method. The accuracy of the deadweight tester specified in the calibration certificate is

$$\Delta p_{ref} = 0.00015 \cdot p_{ref} \rightarrow 0.015 \%.$$

The individual uncertainty of each pressure transmitter described by the absolute error — which is a rather conservative assumption — has been determined with post-calibration sanity checks over the entire pressure range and can be generally assumed to be within

$$\frac{\Delta p}{p} = 7 \cdot 10^{-4} \rightarrow \pm 0.07 \%.$$

The uncertainties of the differential pressure transmitters are assumed to be within

$$\frac{\Delta p}{p} = 5 \cdot 10^{-4} \rightarrow \pm 0.05 \%.$$

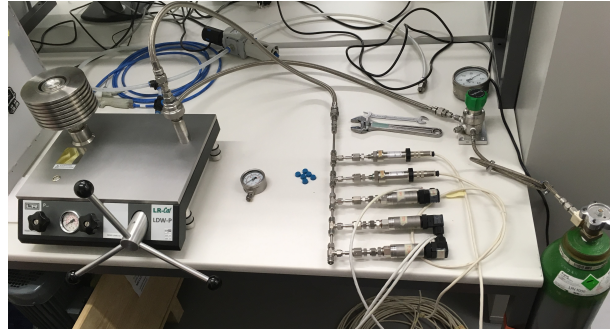


Figure 4 – Calibration of pressure transmitters with a deadweight tester.

A.2.3 Mass flow rate

The accuracy of the *KROHNE OPTIMASS 3300C S03* Coriolis mass flowmeter is specified in its data sheet. Depending on the physical conditions, the accuracy provided is

- $\Delta \dot{m} = 0.0015 \dot{m} \rightarrow$ for liquid
- $\Delta \dot{m} = 0.0055 \dot{m} \rightarrow$ for vapour.

The mass flow meter is located right after the pump discharge and the flow present at the mass flow meter is always in liquid phase. Thus, the uncertainty of the mass flow measurement is:

$$\frac{\Delta \dot{m}}{\dot{m}} = 0.0015 \rightarrow \pm 0.15 \text{ \%}.$$

A.2.4 Diameter and wall thickness

The outer tube diameter was determined with five tube samples, each measured at three different positions with a micrometer. The mean average value of the measurements results in $\bar{d}_o = 9.9957 \text{ mm}$ with a standard deviation of $SD_{d_o} = 0.0032 \text{ mm}$. For further analysis it is assumed that the deviation of the outer diameter can be neglected.

According to the standard ASTM A 269, the tolerances of the inner tube diameter and the wall thickness of seamless tubes with an outer diameter $< 1/2''$ are $\Delta d_i = \pm 0.43 \text{ mm}$ and $\Delta s = \pm 0.15 \text{ mm}$ respectively. This results in uncertainties of $\pm 5.4 \text{ \%}$ for the inner diameter and $\pm 15 \text{ \%}$ for the wall thickness. However, the mean average value of the inner diameter of five tube samples, each measured at three different positions with a inner micrometer reveals an uncertainty of

$$d_i = 8 \text{ mm} \pm 1.1 \text{ \%}.$$

A.2.5 Length of test sections and evaporator

All test sections, including the evaporator, have a length of 8 m. The uncertainties of the lengths are neglected due to $\Delta l \ll l$.

A.3 Uncertainties of derived Quantities

A.3.1 Mass velocity

The mass velocity G is defined as a function of the mass flow rate and the cross-sectional area of the tube, according to

$$G = \frac{\dot{m}}{A}; \text{ where } A = f(d^2). \quad (6)$$

Considering the error propagation of Eq. 4, the uncertainty of the mass velocity results in

$$\frac{\Delta G}{G} = 0.0156 \rightarrow \pm 1.56 \, \%.$$

A.3.2 Enthalpy in single-phase

The single-phase enthalpy, as described in chapter xxx, is determined with REFPROP from NIST [38] in MATLAB. The maximum deviation of the single-phase enthalpy is given by the uncertainties of the single-phase temperature and pressure measurements according to

$$\Delta h_{\max} = \max(h(T \pm \Delta T; p \pm \Delta p)) - \min(h(T \pm \Delta T; p \pm \Delta p)) \quad (7)$$

and can be allocated at the following conditions within the present test range:

$$T_{\max} = 5.2 \, ^\circ\text{C}; p_{\max} = 40 \, \text{bar} \rightarrow h_{5.2 \, ^\circ\text{C}; 40 \, \text{bar}} = 212998.8 \, \text{J kg}^{-1}.$$

The deviating enthalpies according to the uncertainties of the pressure and temperature measurements are listed in Table 3.

Table 3 – Single-phase enthalpies according to the uncertainties of the pressure and temperature measurements at 5.2 °C and 40 bar.

	5.255 °C	5.145 °C
39.965 bar	213154.9 J kg ⁻¹	212854.1 J kg ⁻¹
40.035	213143.6 J kg ⁻¹	212842.9 J kg ⁻¹

According to Equation 7, this results in a maximum error of

$$\max\left(\frac{\Delta h_{\max}}{h}\right) = \frac{h_{5.255 \, ^\circ\text{C}; 39.965 \, \text{bar}} - h_{5.145 \, ^\circ\text{C}; 40.035 \, \text{bar}}}{h_{5.2 \, ^\circ\text{C}; 40 \, \text{bar}}} = 0.0015$$

that deviates symmetrically around the nominal value.

$$\frac{\Delta h_{1p}}{h_{1p}} = \pm 0.075 \, \%$$

A.3.3 Enthalpy in two-phase before the evaporator

Verification of insulation

The calculated heat pickup from ambient, determined with the local temperature difference between ambient and the flow and the thermal bulk resistances of the pipe sections, is verified with single-phase sanity checks. As shown in Figure 5, the calculated values increase in enthalpy according to Eq. 2.8 and the increase in enthalpy derived from the single-phase measurements are consistent throughout the entire temperature range and deviate by about

$$\frac{h_{meas} - h_{pred}}{h_{meas}} \leq 0.3 \text{ \%}.$$

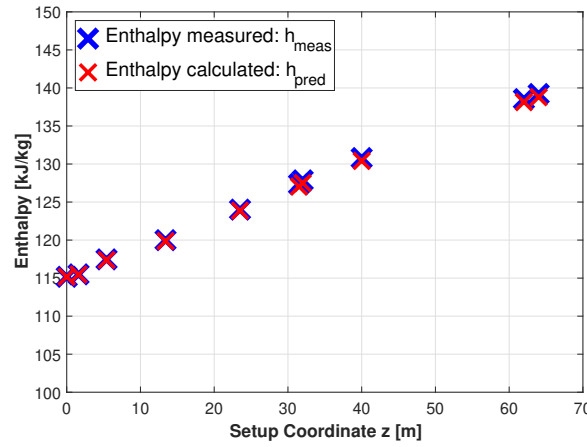


Figure 5 – Sanity check to validate the thermal bulk resistance of the insulation used in Eq. 2.8 for determining the heat pickup from ambient.

Electrical power dissipated by the pre-heater

The power of both the pre- and post-heater are controlled by pulse-width modulation (PWM). The max. voltage and current measured at a full nominal power of 3 kW are determined with repetitive measurements with different instrumentation. The repetitive measurements show very little variance, even when using different multimeters, at both the pre- and the post-heater respectively and reveal the following values.

$$U_{EH,max} = 399.7 \text{ V}$$

$$I_{EH,max} = 4.34 \text{ A}$$

The electrical power dissipated in the 3-phase heaters due to ohmic resistance is determined according to

$$P_{EH,meas} = \sqrt{3} \cdot U \cdot I = 3004.6 \text{ W}.$$

A: Accuracy and Uncertainties

The offset to the nominal heater power of

$$\Delta P_{EH} = |P_{EH,meas} - P_{EH,nom}| \approx 5 \text{ W}$$

results in an uncertainty of $\sim 0.15 \%$.

Enthalpy in two-phase before the evaporator

Based on the uncertainties above and the error propagation according to Eq. 3, the uncertainty of the enthalpy calculation before the evaporator based on Eq. 2.8 results in

$$\frac{\Delta h_{2p}}{h_{2p}} = \pm 0.675 \%$$

A.3.4 Enthalpy in two-phase inside or after the evaporator

Electrical power provided by the power supply

The electrical power applied to the stainless steel tubes for ohmic heating is monitored with the analog interface of the *DELTA ELEKTRONIKA SM 60-100* power supply. The voltage and current are monitored with an accuracy of $\pm 0.2 \%$ respectively. According to Eq. 3, this results in an uncertainty of

$$\frac{\Delta P_{eva}}{P_{eva}} = \pm 0.4 \%$$

Enthalpy in two-phase inside or after the evaporator

The uncertainty of the enthalpy calculation inside or after the evaporator, determined according to Eq. 2.9, amounts to

$$\frac{\Delta h_{2p,eva}}{h_{2p,eva}} = \pm 1.075 \%$$

A.3.5 Vapour quality

The vapour quality defined in Eq. 2.10 is calculated with REFPROP from NIST [38] as a function of the measured pressure and the derived two-phase enthalpy (Eq. 2.8 or 2.9)

$$x = f(p, h_{2p}). \quad (8)$$

The max. deviation of the vapour quality is a result of the max. deviations of the pressure measurement and the derived two-phase enthalpy.

$$\Delta x_{\max} = \max(x(p \pm \Delta p; h_{2p} \pm \Delta h_{2p})) - \min(x(p \pm \Delta p; h_{2p} \pm \Delta h_{2p})) \quad (9)$$

Based on the corresponding uncertainties of the pressure measurements and the two-phase enthalpies, the uncertainty of the vapour quality calculations before the evaporator amounts to

$$\frac{\Delta x}{x} = \pm 0.3 \, \%$$

The uncertainty of the vapour quality calculations inside or after the evaporator result in

$$\frac{\Delta x_{eva}}{x_{eva}} = \pm 0.5 \, \%$$

These values are valid within the range of operation of the setup (16–40 bar).

A.3.6 Heat flux

The heat flux due to the Joule effect (Eq. 2.11) is influenced by the evaporator power, the inner tube diameter of the evaporator and by the length of the test section. The uncertainty in the length of the test section is neglected due to $\Delta l_{eva} \ll l_{eva}$. The electrical power of the evaporator, provided by the power supply and dissipated due to the ohmic resistance of the tube, is determined based on the voltage measured between the copper clamps and the current conducted through the stainless steel pipe.

$$P_{PS} = \dot{Q}_{eva} = U_{eva} \cdot I_{eva} \quad (10)$$

According to Eq. 3 this results in an uncertainty of

$$\frac{\Delta \dot{q}}{\dot{q}} = \pm 1.5 \, \%$$

A.3.7 Heat transfer coefficient

The heat transfer coefficient is defined according to Eq. xxx. The uncertainty of the heat transfer coefficient is a superposition of the uncertainties of (i) the power applied to the flow inside the evaporator \dot{Q}_{eva} , (ii) the temperature measured at the outer tube wall $T_{w,o}$, (iii) the saturation temperature T_{sat} derived from the measured saturation pressure (and hence dependent on the uncertainty of p_{sat}) and (iv) the inner tube diameter d_i . As mentioned earlier, the uncertainties of the outer tube diameter d_o , the length of the evaporator l_{eva} and the temperature dependent conductivity of the tube wall $k_{1.4404}$ are neglected. Table 4 presents the uncertainty of the heat transfer coefficient as a function of its magnitude and the heat flux.

$$\alpha = \frac{\dot{q}}{\Delta T} = \frac{\dot{q}}{T_{w,o} - T_{sat} - \Delta T_w} \quad (11)$$

Table 4 – Uncertainties of the heat transfer coefficient [%].

		α [W m ⁻² K ⁻¹]						
		2000	4000	6000	8000	10000	12000	14000
q [W m ⁻²]	5000	3.26	5.01	7.02	9.12	11.26	13.42	15.59
	10000	2.64	3.26	4.08	5.01	6.00	7.02	8.07
	15000	2.51	2.81	3.26	3.79	4.38	5.01	5.67

List of Acronyms

2PACL	Two-Phase Accumulator Controlled Loop
ALICE	A Large Ion Collider Experiment
ATLAS	A Toroidal LHC ApparatuS
ATLAS ITk	ATLAS Inner Tracker
CHF	Critical Heat Flux
CNN	Convolutional Neural Network
CO ₂	Carbon Dioxide
CORA	CO ₂ Research Apparatus
DAQ	Data Acquisition
DNB	Departure of Nucleate Boiling
EVA	Evaporator
GWP	Global Warming Potential
HEP	High Energy Physics
HL-LHC	High-Luminosity Large Hadron Collider
ISS	International Space Station
LHC	Large Hadron Collider
LHCb	Large Hadron Collider beauty
NIST	National Institute of Standards and Technology
P&ID	Piping and Instrumentation Diagram
PFC	Perfluorocarbon
PLC	Programmable Logic Controller
RAHEL	Research Apparatus with Horizontal Evaporative Lines
RTD	Resistance Temperature Detector
STD	Standard Deviation
SCADA	Supervisory Control and Data Acquisition
UNICOS	Unified Industrial Control System

List of Symbols

Roman

Symbol	Unit	Definition
Bo	[]	Boiling Number
c	$\text{J kg}^{-1} \text{K}^{-1}$	Specific Heat
d	m	Diameter
E	J	Energy
F	[]	Heat Transfer enhancement Factor
Fr	[]	Froude Number
G	$\text{kg m}^{-2} \text{s}^{-1}$	Mass Velocity / Mass Flux
g	m s^{-2}	Gravitational Constant $g = 9.81$
h	J kg^{-1}	Specific Enthalpy
I	A	Current
j	m s^{-1}	Superficial Velocity
k	$\text{W m}^{-1} \text{K}^{-1}$	Thermal Conductivity
l	m	Length
\dot{m}	kg s^{-1}	Mass Flow Rate
MAPE	%	Mean Absolute Percentage Error
MPE	%	Mean Percentage Error
Nu	[]	Nusselt Number
P	W	Power
p	bar	Pressure
\dot{Q}	W	Heat Flow Rate
q	W m^{-2}	Heat Flux
\bar{R}	$\text{W K}^{-1} \text{m}^{-1}$	Mean Thermal Bulk Resistance per Unit Length
Re	[]	Reynolds Number
RMSE	unit	Root Mean Square Error
T	$^{\circ}\text{C}$	Temperature
t	s	Time
U	V	Voltage
ν	$\text{m}^3 \text{kg}^{-1}$	Specific Volume
W	J	Mechanical Work

Symbol	Unit	Definition
We	[]	Weber Number
x	[]	Vapour Quality
X_0	cm	Radiation Length
y	m	Axial Coordinate of Evaporator
z	m	Coordinate of unheated Piping

Greek

Symbol	Unit	Definition
α	$\text{W m}^{-2}\text{K}^{-1}$	Heat Transfer Coefficient
ε	[]	Void Fraction
ϑ	°	Angle of Inclination
μ	$\text{Pa s} = \text{N s m}^{-2}$	Dynamic Viscosity
ξ	%	Percentage of Data Points within specified Deviation
ρ	kg m^{-3}	Density
σ	N m^{-1}	Surface Tension
σ_{STD}	unit	Standard Deviation

Subscripts

Symbol	Definition
1p	single-phase
2p	two-phase
ac	acceleration
accu	accumulator
abs	absorbed
bs	bubbly-slug
ca	churn-annular
CV	control volume
di	dryout inception
EH	electrical heater
eva	evaporator
exp	experimental
f	fluid
fa	fluid-ambient
fr	friction
i	inner / increment
in	input
inc	inclined

List of Symbols

Symbol	Definition
l	liquid
lo	liquid only
loc	local
m	measured
o	outer
pred	predicted
r	reduced / ratio
sat	saturation
sc	slug-churn
st	static
STD	standard deviation
t	total
tr	transition
ts	test section
v	vapour
vo	vapour only
w	wall

Bibliography

- [1] L. Evans, “The Large Hadron Collider”, [“New Journal of Physics”](#), vol. 9, no. 9, Sep. 2007.
- [2] P. Vankov, “ATLAS Upgrade for the HL-LHC: meeting the challenges of a five-fold increase in collision rate”, [“EPJ Web of Conferences”](#), vol. 28, 2012.
- [3] M. Brice and J. M. Ordan, LHC tunnel pt1, Feb. 2018.
- [4] E. Mobs, The CERN accelerator complex - 2019. Complexe des accélérateurs du CERN - 2019, Jul. 2019.
- [5] The ATLAS Experiment, <https://atlas.cern/discover/collaboration>.
- [6] The_ATLAS_Collaboration, G. Aad, E. Abat, *et al.*, “The ATLAS Experiment at the CERN Large Hadron Collider”, [“Journal of Instrumentation”](#), vol. 3, no. 08, Aug. 2008.
- [7] P. Petagna, B. Verlaet, and A. Francescon, “Two-Phase Thermal Management of Silicon Detectors for High Energy Physics”, *Encyclopedia of Two-Phase Heat Transfer and Flow III: Macro and Micro Flow Boiling and Numerical Modeling Fundamentals Volume 4: Special Boiling Topics*, J. R. Thome, Ed., vol. 4, WORLD SCIENTIFIC, May 2018, pp. 335–412.
- [8] S. Seidel, “Silicon strip and pixel detectors for particle physics experiments”, [“Physics Reports”](#), vol. 828, Oct. 2019.
- [9] C. Marcelloni, The ATLAS pixel detector, the most inner part of the inner detector installed in the cavern, Jun. 2007.
- [10] M. Brice, First half of CMS inner tracker barrel, Oct. 2006.
- [11] The_ATLAS_Collaboration, “Letter of Intent for the Phase-II Upgrade of the ATLAS Experiment”, CERN, Geneva, Tech. Rep. CERN-LHCC-2012-022, LHCC-I-023, Dec. 2012.
- [12] H. Weber, “The construction of the phase-1 upgrade of the CMS pixel detector”, [“Journal of Instrumentation”](#), vol. 12, no. 12, Dec. 2017.

-
- [13] S. Braibant, N. Demaria, L. Feld, A. Frey, A. Fürtjes, W. Glessing, R. Hammarström, A. Honma, M. Mannelli, C. Mariotti, P. Mättig, E. Migliore, S. Piperov, O. Runolfsson, B. Schmitt, A. Söldner-Rembold, and B. Surrow, “Investigation of design parameters for radiation hard silicon microstrip detectors”, [“Nuclear Instruments and Methods in Physics Research Section A: Accelerators, Spectrometers, Detectors and Associated Equipment”](#), vol. 485, no. 3, Jun. 2002.
- [14] P. Tropea, J. Daguin, D. Giakoumi, N. Koss, P. Petagna, H. Postema, D. Schmid, B. Verlaat, and L. Zwalinski, “Advancements and plans for the LHC upgrade detector thermal management with CO₂ evaporative cooling”, [“Nuclear Instruments and Methods in Physics Research Section A: Accelerators, Spectrometers, Detectors and Associated Equipment”](#), vol. 936, Aug. 2019.
- [15] H. Pernegger, “The ATLAS Insertable B-Layer Pixel Detector”, *International Workshop on Vertex Detectors*, ATL-COM-INDET-2011-061, Rust, Austria, Jun. 2011.
- [16] ATLAS_Collaboration, “Technical Design Report for the ATLAS Inner Tracker Strip Detector”, CERN, Geneva, Tech. Rep. CERN-LHCC-2017-005, ATLAS-TDR-025, Apr. 2017.
- [17] CMS_Collaboration, “The Phase-2 Upgrade of the CMS Tracker; Technical Design Report”, CERN, Geneva, Tech. Rep. CERN-LHCC-2017-009, CMS-TDR-014, Jun. 2017.
- [18] ATLAS_Collaboration, “Technical Design Report for the ATLAS Inner Tracker Pixel Detector”, CERN, Geneva, Tech. Rep. CERN-LHCC-2017-021, ATLAS-TDR-030, Sep. 2017.
- [19] Verlaat, M. Van Beuzekom, and A. Van Lysebetten, “CO₂ cooling for HEP experiments”, *Proceedings of the Topical Workshop on Electronics for Particle Physics*, ser. TWEPP-2008, Publisher: CERN, Naxos, Greece, 2008.
- [20] B. Verlaat, A. Colijn, and H. Postema, “The future of CO₂ cooling in particle physics detectors”, *International Conference of Refrigeration*, ser. ICR11-B2-309, Prague, Czech Republic, 2011, p. 8.
- [21] G. Lorentzen, “The use of natural refrigerants: a complete solution to the CFC/HCFC predicament”, [“International Journal of Refrigeration”](#), vol. 18, no. 3, Mar. 1995.
- [22] D. K. und Klimatechnischer Verein, Ed., Kohlendioxid - Besonderheiten und Einsatzchancen als Kältemittel, ser. Statusbericht des Deutschen Kälte- und Klimatechnischen Vereins 20. Stuttgart: DKV, 1998.
- [23] A. Van Lysebetten, B. Verlaat, and M. van Beuzekom, “CO₂ cooling experience (LHCb)”, *Proceedings of The 16th International Workshop on Vertex detectors — PoS(Vertex 2007)*, Lake Placid, NY, USA: Sissa Medialab, Aug. 2008, p. 009.
- [24] L. Feld, W. Karpinski, J. Merz, and M. Wlochal, “CO₂ cooling for the CMS tracker at SLHC”, [“Journal of Instrumentation”](#), vol. 6, no. 01, Jan. 2011.

BIBLIOGRAPHY

- [25] B. Verlaet, M. Ostrega, L. Zwalinski, C. Bortolin, S. Vogt, J. Godlewski, O. Crespo-Lopez, M. V. Overbeek, and T. Blaszyk, "The ATLAS IBL CO₂ cooling system", ["Journal of Instrumentation"](#), vol. 12, no. 02, Feb. 2017.
- [26] B. Verlaet, H. B. Rookhuizen, A. A. M. Delil, A. A. Woering, E. Perrin, M. Pohl, and R. Battiston, "Feasibility demonstration of a mechanically pumped two-phase CO₂ cooling loop for the AMS-2 tracker experiment", *AIP Conference Proceedings*, ISSN: 0094243X, vol. 608, Albuquerque, New Mexico (USA): AIP, 2002, pp. 57–64.
- [27] V. Bhanot, L. Zwalinski, J. Noite, H. Postema, J. Godlewski, T. Köttig, and B. Verlaet, "The CORA CO₂ Cooling Plant", *Proceedings of the 10th IIT-Gustav Lorentzen Conference on Natural Working Fluids*, ser. GL-239, Delft, The Netherlands, 2012.
- [28] B. Verlaet, "Controlling a 2-phase CO₂ loop using a 2-phase accumulator", *International Conference of Refrigeration*, ser. ICR07-B2-1565, Beijing, China, 2007.
- [29] P. A. Kew and K. Cornwell, "Correlations for the prediction of boiling heat transfer in small-diameter channels", ["Applied Thermal Engineering"](#), vol. 17, no. 8-10, Aug. 1997.
- [30] S. G. Kandlikar, "Fundamental issues related to flow boiling in minichannels and microchannels", ["Experimental Thermal and Fluid Science"](#), vol. 26, no. 2-4, Jun. 2002.
- [31] C. Ong and J. Thome, "Macro-to-microchannel transition in two-phase flow: Part 1 – Two-phase flow patterns and film thickness measurements", ["Experimental Thermal and Fluid Science"](#), vol. 35, no. 1, Jan. 2011.
- [32] M. Ritzert, E. Blanco Viñuela, M. Ostrega, and L. Zwalinski, "UNICOS Framework and EPICS: A Possible Integration", *Proceedings of the 16th Int. Conf. on Accelerator and Large Experimental Control Systems*, ser. ICALEPCS2017, Barcelona, Spain: JACoW, 2018, p. 3.
- [33] C. Roderick, "CERN accelerator data logging and analysis", *2013 IEEE Nuclear Science Symposium and Medical Imaging Conference (2013 NSS/MIC)*, Seoul, Korea (South): IEEE, Oct. 2013, pp. 1–3.
- [34] W. Hulek, "Functional Analysis for Continuous Process Control (CPC); CO₂ DAQ RACK A", CERN, Geneva, CERN EDMS Document 2427301, 2008, p. 28.
- [35] H. Blasius, "Das Aehnlichkeitsgesetz bei Reibungsvorgängen in Flüssigkeiten", *Mitteilungen über Forschungsarbeiten auf dem Gebiete des Ingenieurwesens*, Verein deutscher Ingenieure, Ed., Berlin, Heidelberg: Springer Berlin Heidelberg, 1913, pp. 1–41.
- [36] VDI e. V., Ed., VDI Heat Atlas. Berlin, Heidelberg: Springer Berlin Heidelberg, 2010.
- [37] G. Cerbe and G. Wilhelms, Technische Thermodynamik: theoretische Grundlagen und praktische Anwendungen. München: Hanser, 2007, OCLC: 263706592.
- [38] M. Huber, A. Harvey, E. Lemmon, G. Hardin, I. Bell, and M. McLinden, NIST Reference Fluid Thermodynamic and Transport Properties Database (REFPROP) Version 10 - SRD 23, type: dataset, 2018.
- [39] R. Winterton, "Where did the Dittus and Boelter equation come from?", ["International Journal of Heat and Mass Transfer"](#), vol. 41, no. 4-5, Feb. 1998.

-
- [40] V. Gnielinski, "Neue Gleichungen für den Wärme- und den Stoffübergang in turbulent durchströmten Rohren und Kanälen", *"Forschung im Ingenieurwesen"*, vol. 41, 1975.
- [41] MATLAB, 9.1.0.441655 (R2016b). Natick, Massachusetts: The MathWorks Inc., 2016.
- [42] N. Kattan, J. R. Thome, and D. Favrat, "Flow Boiling in Horizontal Tubes: Part 1—Development of a Diabatic Two-Phase Flow Pattern Map", *"Journal of Heat Transfer"*, vol. 120, no. 1, Feb. 1998.
- [43] —, "Flow Boiling in Horizontal Tubes: Part 3—Development of a New Heat Transfer Model Based on Flow Pattern", *"Journal of Heat Transfer"*, vol. 120, no. 1, Feb. 1998.
- [44] L. Wojtan, T. Ursenbacher, and J. R. Thome, "Investigation of flow boiling in horizontal tubes: Part I—A new diabatic two-phase flow pattern map", *"International Journal of Heat and Mass Transfer"*, vol. 48, no. 14, Jul. 2005.
- [45] —, "Investigation of flow boiling in horizontal tubes: Part II—Development of a new heat transfer model for stratified-wavy, dryout and mist flow regimes", *"International Journal of Heat and Mass Transfer"*, vol. 48, no. 14, Jul. 2005.
- [46] J. El Hajal, J. Thome, and A. Cavallini, "Condensation in horizontal tubes, part 1: two-phase flow pattern map", *"International Journal of Heat and Mass Transfer"*, vol. 46, no. 18, Aug. 2003.
- [47] J. Thome, J. El Hajal, and A. Cavallini, "Condensation in horizontal tubes, part 2: new heat transfer model based on flow regimes", *"International Journal of Heat and Mass Transfer"*, vol. 46, no. 18, Aug. 2003.
- [48] G. F. Hewitt and D. N. Roberts, "Studies of two-phase flow patterns by simultaneous x-ray and fast photography", Atomic Energy Research Establishment, Harwell, England (United Kingdom), Tech. Rep. AERE-M-2159, Feb. 1969.
- [49] B. A. W. Bennett, G. F. Hewitt, H. A. Kearsley, R. K. F. Keeys, and P. M. C. Lacey, "Flow Visualization Studies of Boiling at High Pressure", *"Proceedings of the Institution of Mechanical Engineers, Conference Proceedings"*, vol. 180, no. 3, Jun. 1965.
- [50] Y. Taitel, D. Barnea, and A. E. Dukler, "Modelling flow pattern transitions for steady upward gas-liquid flow in vertical tubes", *"AIChE Journal"*, vol. 26, no. 3, May 1980.
- [51] D. Barnea, "A unified model for predicting flow-pattern transitions for the whole range of pipe inclinations", *"International Journal of Multiphase Flow"*, vol. 13, no. 1, Jan. 1987.
- [52] Y. Taitel and A. E. Dukler, "A model for predicting flow regime transitions in horizontal and near horizontal gas-liquid flow", *"AIChE Journal"*, vol. 22, no. 1, Jan. 1976.
- [53] V. Kadambi, "Stability of annular flow in horizontal tubes", *"International Journal of Multiphase Flow"*, vol. 8, no. 4, Aug. 1982.
- [54] P. Lin and T. Hanratty, "Prediction of the initiation of slugs with linear stability theory", *"International Journal of Multiphase Flow"*, vol. 12, no. 1, Jan. 1986.

BIBLIOGRAPHY

- [55] M. Kaichiro and M. Ishii, "Flow regime transition criteria for upward two-phase flow in vertical tubes", ["International Journal of Heat and Mass Transfer"](#), vol. 27, no. 5, May 1984.
- [56] K. McQuillan and P. Whalley, "Flow patterns in vertical two-phase flow", ["International Journal of Multiphase Flow"](#), vol. 11, no. 2, Mar. 1985.
- [57] D. Barnea, O. Shoham, and Y. Taitel, "Flow pattern transition for vertical downward two phase flow", ["Chemical Engineering Science"](#), vol. 37, no. 5, 1982.
- [58] D. Barnea and N. Brauner, "Holdup of the liquid slug in two phase intermittent flow", ["International Journal of Multiphase Flow"](#), vol. 11, no. 1, Jan. 1985.
- [59] D. Barnea, O. Shoham, and Y. Taitel, "Flow pattern transition for downward inclined two phase flow; horizontal to vertical", ["Chemical Engineering Science"](#), vol. 37, no. 5, 1982.
- [60] D. Barnea, "Transition from annular flow and from dispersed bubble flow—unified models for the whole range of pipe inclinations", ["International Journal of Multiphase Flow"](#), vol. 12, no. 5, Sep. 1986.
- [61] S. Rouhani and M. Sohal, "Two-phase flow patterns: A review of research results", ["Progress in Nuclear Energy"](#), vol. 11, no. 3, Jan. 1983.
- [62] L. Cheng, G. Ribatski, and J. R. Thome, "Two-Phase Flow Patterns and Flow-Pattern Maps: Fundamentals and Applications", ["Applied Mechanics Reviews"](#), vol. 61, no. 5, Sep. 2008.
- [63] J. Pettersen, "Flow vaporization of CO₂ in microchannel tubes", ["Experimental Thermal and Fluid Science"](#), vol. 28, no. 2-3, Jan. 2004.
- [64] —, "Two-Phase Flow Patterns in Microchannel Vaporization of CO₂ at Near-Critical Pressure", ["Heat Transfer Engineering"](#), vol. 25, no. 3, Apr. 2004.
- [65] R. Yun and Y. Kim, "Flow regimes for horizontal two-phase flow of CO₂ in a heated narrow rectangular channel", ["International Journal of Multiphase Flow"](#), vol. 30, no. 10, Oct. 2004.
- [66] A.-E. Schael and M. Kind, "Flow pattern and heat transfer characteristics during flow boiling of CO₂ in a horizontal micro fin tube and comparison with smooth tube data", ["International Journal of Refrigeration"](#), vol. 28, no. 8, Dec. 2005.
- [67] J. L. Gasche, "Carbon dioxide evaporation in a single microchannel", ["Journal of the Brazilian Society of Mechanical Sciences and Engineering"](#), vol. 28, no. 1, Mar. 2006.
- [68] J. R. Thome and G. Ribatski, "State-of-the-art of two-phase flow and flow boiling heat transfer and pressure drop of CO₂ in macro- and micro-channels", ["International Journal of Refrigeration"](#), vol. 28, no. 8, Dec. 2005.
- [69] J. R. Thome and J. E. Hajal, "Two-Phase Flow Pattern Map for Evaporation in Horizontal Tubes: Latest Version", ["Heat Transfer Engineering"](#), vol. 24, no. 6, Nov. 2003.

-
- [70] L. Cheng, G. Ribatski, L. Wojtan, and J. R. Thome, "New flow boiling heat transfer model and flow pattern map for carbon dioxide evaporating inside horizontal tubes", ["International Journal of Heat and Mass Transfer"](#), vol. 49, no. 21-22, Oct. 2006.
- [71] —, "Erratum to: "new flow boiling heat transfer model and flow pattern map for carbon dioxide evaporating inside horizontal tubes", ["International Journal of Heat and Mass Transfer"](#), vol. 50, no. 21-22, 2007.
- [72] L. Cheng, G. Ribatski, J. Moreno Quibén, and J. R. Thome, "New prediction methods for CO₂ evaporation inside tubes: Part I – A two-phase flow pattern map and a flow pattern based phenomenological model for two-phase flow frictional pressure drops", ["International Journal of Heat and Mass Transfer"](#), vol. 51, no. 1-2, Jan. 2008.
- [73] R. Mastrullo, A. W. Mauro, J. R. Thome, D. Toto, and G. P. Vanoli, "Flow pattern maps for convective boiling of CO₂ and R410A in a horizontal smooth tube: Experiments and new correlations analyzing the effect of the reduced pressure", ["International Journal of Heat and Mass Transfer"](#), vol. 55, no. 5, Feb. 2012.
- [74] L. Cheng, G. Xia, and J. R. Thome, "Flow boiling heat transfer and two-phase flow phenomena of CO₂ in macro- and micro-channel evaporators: Fundamentals, applications and engineering design", ["Applied Thermal Engineering"](#), vol. 195, Aug. 2021.
- [75] X. Fu, P. Zhang, H. Hu, C. J. Huang, Y. Huang, and R. Z. Wang, "3D visualization of two-phase flow in the micro-tube by a simple but effective method", ["Journal of Micromechanics and Microengineering"](#), vol. 19, no. 8, Aug. 2009.
- [76] J. R. Thome and Wieland-Werke, *The Heat Transfer Data Book III Enhanced heat transfer design methods for tubular heat exchangers*. 2016, OCLC: 962096023.
- [77] J. R. Thome and A. Cioncolini, *Encyclopedia of Two-Phase Heat Transfer and Flow I: Fundamentals and Methods Volume 3: Flow Boiling in Macro and Microchannels*, J. R. Thome, Ed. WORLD SCIENTIFIC, Oct. 2015, vol. 3.
- [78] Y. Taitel, D. Barnea, and A. Dukler, "A film model for the prediction of flooding and flow reversal for gas-liquid flow in vertical tubes", ["International Journal of Multiphase Flow"](#), vol. 8, no. 1, Feb. 1982.
- [79] D. Barnea and Y. Taitel, "Stability of annular flow", ["International Communications in Heat and Mass Transfer"](#), vol. 12, no. 5, Sep. 1985.
- [80] K. McQuillan and P. Whalley, "A comparison between flooding correlations and experimental flooding data for gas-liquid flow in vertical circular tubes", ["Chemical Engineering Science"](#), vol. 40, no. 8, 1985.
- [81] R. Revellin, V. Dupont, T. Ursenbacher, J. R. Thome, and I. Zun, "Characterization of diabatic two-phase flows in microchannels: Flow parameter results for R-134a in a 0.5mm channel", ["International Journal of Multiphase Flow"](#), vol. 32, no. 7, Jul. 2006.
- [82] H. Wu and Q. Duan, "Gas Void Fraction Measurement of Gas-Liquid Two-Phase CO₂ Flow Using Laser Attenuation Technique", ["Sensors"](#), vol. 19, no. 14, Jul. 2019.

BIBLIOGRAPHY

- [83] K. He, X. Zhang, S. Ren, and J. Sun, "Deep Residual Learning for Image Recognition", ["arXiv:1512.03385 \[cs\]"](#), Dec. 2015, arXiv: 1512.03385.
- [84] S. Hochreiter and J. Schmidhuber, "Long Short-Term Memory", ["Neural Computation"](#), vol. 9, no. 8, Nov. 1997.
- [85] S. Kadish, D. Schmid, J. Son, and E. Boje, "Computer Vision-Based Classification of Flow Regime and Vapor Quality in Vertical Two-Phase Flow", ["Sensors"](#), vol. 22, no. 3, Jan. 2022.
- [86] J. Weisman and S. Kang, "Flow pattern transitions in vertical and upwardly inclined lines", ["International Journal of Multiphase Flow"](#), vol. 7, no. 3, Jun. 1981.
- [87] H. Mukherjee and J. P. Brill, "Empirical equations to predict flow patterns in two-phase inclined flow", ["International Journal of Multiphase Flow"](#), vol. 11, no. 3, May 1985.
- [88] S. Jayanti and G. Hewitt, "Prediction of the slug-to-churn flow transition in vertical two-phase flow", ["International Journal of Multiphase Flow"](#), vol. 18, no. 6, Nov. 1992.
- [89] X. Chen and J. Brill, "Slug to churn transition in upward vertical two-phase flow", ["Chemical Engineering Science"](#), vol. 52, no. 23, Dec. 1997.
- [90] S. Lips and J. P. Meyer, "Experimental study of convective condensation in an inclined smooth tube. Part I: Inclination effect on flow pattern and heat transfer coefficient", ["International Journal of Heat and Mass Transfer"](#), vol. 55, no. 1-3, Jan. 2012.
- [91] T. Layssac, S. Lips, and R. Revellin, "Experimental study of flow boiling in an inclined mini-channel: Effect of inclination on flow pattern transitions and pressure drops", ["Experimental Thermal and Fluid Science"](#), vol. 98, Nov. 2018.
- [92] X. Fang, Q. Wu, and Y. Yuan, "A general correlation for saturated flow boiling heat transfer in channels of various sizes and flow directions", ["International Journal of Heat and Mass Transfer"](#), vol. 107, Apr. 2017.
- [93] D. Hellenschmidt, M. Bomben, G. Calderini, M. Boscardin, M. Crivellari, S. Ronchin, and P. Petagna, "New insights on boiling carbon dioxide flow in mini- and micro-channels for optimal silicon detector cooling", ["Nuclear Instruments and Methods in Physics Research Section A: Accelerators, Spectrometers, Detectors and Associated Equipment"](#), vol. 958, Apr. 2020.
- [94] A. J. Ghajar and S. M. Bhagwat, "Effect of Void Fraction and Two-Phase Dynamic Viscosity Models on Prediction of Hydrostatic and Frictional Pressure Drop in Vertical Upward Gas-Liquid Two-Phase Flow", ["Heat Transfer Engineering"](#), vol. 34, no. 13, Oct. 2013.
- [95] S.-M. Kim and I. Mudawar, "Review of databases and predictive methods for pressure drop in adiabatic, condensing and boiling mini/micro-channel flows", ["International Journal of Heat and Mass Transfer"](#), vol. 77, Oct. 2014.
- [96] R. Lockhart and R. Martinelli, "Proposed correlation of data for isothermal two-phase, two-component flow in pipes", ["Chemical Engineering Progress"](#), vol. 45, 1949.

-
- [97] L. Friedel, "Improved Friction Pressure Drop Correlation for Horizontal and Vertical Two-Phase Pipe Flow", *"3R International"*, vol. 18, 1979.
- [98] H. Müller-Steinhagen and K. Heck, "A simple friction pressure drop correlation for two-phase flow in pipes", *"Chemical Engineering and Processing: Process Intensification"*, vol. 20, no. 6, Nov. 1986.
- [99] D. Jung and R. Radermacher, "Prediction of pressure drop during horizontal annular flow boiling of pure and mixed refrigerants", *"International Journal of Heat and Mass Transfer"*, vol. 32, no. 12, Dec. 1989.
- [100] C.-C. Wang, C.-S. Chiang, and D.-C. Lu, "Visual observation of two-phase flow pattern of R-22, R-134a, and R-407C in a 6.5-mm smooth tube", *"Experimental Thermal and Fluid Science"*, vol. 15, no. 4, Nov. 1997.
- [101] L. Sun and K. Mishima, "Evaluation Analysis of Prediction Methods for Two-Phase Flow Pressure Drop in Mini-Channels", *Volume 2: Fuel Cycle and High Level Waste Management; Computational Fluid Dynamics, Neutronics Methods and Coupled Codes; Student Paper Competition*, Orlando, Florida, USA: ASMEDC, Jan. 2008, pp. 649–658.
- [102] K. Mishima and T. Hibiki, "Some characteristics of air-water two-phase flow in small diameter vertical tubes", *"International Journal of Multiphase Flow"*, vol. 22, no. 4, Aug. 1996.
- [103] A. M. Bredesen, A. Hafner, J. Pettersen, P. Neksa, and K. Aflekt, "Heat transfer and pressure drop for in-tube evaporation of CO₂", *Proceedings of the International Conference on Heat Transfer Issues in Natural Refrigerants*, University of Maryland, USA, 1997, pp. 1–15.
- [104] D. Chisholm, "Pressure gradients due to friction during the flow of evaporating two-phase mixtures in smooth tubes and channels", *"International Journal of Heat and Mass Transfer"*, vol. 16, no. 2, Feb. 1973.
- [105] C. J. Baroczy, "Systematic correlation for two-phase pressure drop", *"Chem. Eng. Progr., Symp. Ser., 62: No. 64, 232-49"*, Jan. 1966, Institution: Atomics International, Canoga Park, Calif.
- [106] R. Grönnerud, "Investigation of liquid hold-up, flow resistance and heat transfer in circulation type evaporators. 4. Two-phase flow resistance in boiling refrigerants.", *IIR conference, Heat and mass transfer in refrigeration systems and in air conditioning*, Freudenstadt, Germany, Sep. 1972, pp. 127–138.
- [107] S. H. Yoon, E. S. Cho, Y. W. Hwang, M. S. Kim, K. Min, and Y. Kim, "Characteristics of evaporative heat transfer and pressure drop of carbon dioxide and correlation development", *"International Journal of Refrigeration"*, vol. 27, no. 2, Mar. 2004.
- [108] J. Moreno Quibén and J. R. Thome, "Flow pattern based two-phase frictional pressure drop model for horizontal tubes. Part I: Diabatic and adiabatic experimental study", *"International Journal of Heat and Fluid Flow"*, vol. 28, no. 5, Oct. 2007.

BIBLIOGRAPHY

- [109] —, “Flow pattern based two-phase frictional pressure drop model for horizontal tubes, Part II: New phenomenological model”, [“International Journal of Heat and Fluid Flow”](#), vol. 28, no. 5, Oct. 2007.
- [110] J. Moreno Quibén, “Experimental and analytical study of two-phase pressure drops during evaporation in horizontal tubes”, Ph.D. dissertation, EPFL, Lausanne, 2005.
- [111] D. Hellenschmidt and P. Petagna, “Effects of saturation temperature on the boiling properties of carbon dioxide in small diameter pipes at low vapour quality: Pressure drop”, [“International Journal of Heat and Mass Transfer”](#), vol. 163, Dec. 2020.
- [112] P. K. Vijayan, A. P. Patil, D. S. Pilkhwal, D. Saha, and V. Venkat Raj, “An assessment of pressure drop and void fraction correlations with data from two-phase natural circulation loops”, [“Heat and Mass Transfer”](#), vol. 36, no. 6, Nov. 2000.
- [113] D. Butterworth, “A comparison of some void-fraction relationships for co-current gas-liquid flow”, [“International Journal of Multiphase Flow”](#), vol. 1, no. 6, Apr. 1975.
- [114] S. M. Zivi, “Estimation of Steady-State Steam Void-Fraction by Means of the Principle of Minimum Entropy Production”, [“Journal of Heat Transfer”](#), vol. 86, no. 2, May 1964.
- [115] J. Thom, “Prediction of pressure drop during forced circulation boiling of water”, [“International Journal of Heat and Mass Transfer”](#), vol. 7, no. 7, Jul. 1964.
- [116] C. Baroczy, “Correlation of liquid fraction in two-phase flow with application to liquid metals”, United States, Tech. Rep. NAA-SR-8171, 4742622, Apr. 1963, p. 42.
- [117] J. Turner and G. Wallis, “The separate-cylinders model of two-phase flow”, Thayer School of Engineering, Dartmouth College, Hanover, NH, USA, Tech. Rep. NYO-3114-6, 1965.
- [118] N. Zuber and J. A. Findlay, “Average Volumetric Concentration in Two-Phase Flow Systems”, [“Journal of Heat Transfer”](#), vol. 87, no. 4, Nov. 1965.
- [119] G. B. Wallis, One-dimensional two-phase flow. New York, NY: McGraw-Hill, Jan. 1969.
- [120] B. Chexal, J. Horowitz, and G. Lellouche, “An assessment of eight void fraction models for vertical flows”, Nuclear Safety Analysis Center, Palo Alto, United States, Tech. Rep. NSAC-107, 1986, INIS Reference Number: 19084499.
- [121] B. Chexal, J. Horowitz, and G. Lellouche, “An assessment of eight void fraction models”, [“Nuclear Engineering and Design”](#), vol. 126, no. 1, Apr. 1991.
- [122] P. Coddington and R. Macian, “A study of the performance of void fraction correlations used in the context of drift-flux two-phase flow models”, [“Nuclear Engineering and Design”](#), vol. 215, no. 3, Jun. 2002.
- [123] M. A. Woldesemayat and A. J. Ghajar, “Comparison of void fraction correlations for different flow patterns in horizontal and upward inclined pipes”, [“International Journal of Multiphase Flow”](#), vol. 33, no. 4, Apr. 2007.

-
- [124] A. Premoli, D. Di Francesco, and A. Prina, “Una correlazione adimensionale per la determinazione della densità di miscele bifasiche”, *XXV Congresso Nazionale ATI*, vol. 25, Trieste: La Termotecnica, 1970, pp. 17–26.
- [125] S. Rouhani and E. Axelsson, “Calculation of void volume fraction in the subcooled and quality boiling regions”, *“International Journal of Heat and Mass Transfer”*, vol. 13, no. 2, Feb. 1970.
- [126] S. Morooka, T. Ishizuka, M. Iizuka, and K. Yoshimura, “Experimental study on void fraction in a simulated BWR fuel assembly (evaluation of cross-sectional averaged void fraction)”, *“Nuclear Engineering and Design”*, vol. 114, no. 1, May 1989.
- [127] P. V. Godbole, C. C. Tang, and A. J. Ghajar, “Comparison of Void Fraction Correlations for Different Flow Patterns in Upward Vertical Two-Phase Flow”, *“Heat Transfer Engineering”*, vol. 32, no. 10, Sep. 2011.
- [128] A. Cioncolini and J. R. Thome, “Void fraction prediction in annular two-phase flow”, *“International Journal of Multiphase Flow”*, vol. 43, Jul. 2012.
- [129] S. M. Bhagwat and A. J. Ghajar, “Flow Pattern and Pipe Orientation Independent Semi-Empirical Void Fraction Correlation for a Gas-Liquid Two Phase Flow Based on the Concept of Drift Flux Model”, *Volume 2: Heat Transfer Enhancement for Practical Applications; Fire and Combustion; Multi-Phase Systems; Heat Transfer in Electronic Equipment; Low Temperature Heat Transfer; Computational Heat Transfer*, Rio Grande, Puerto Rico, USA: American Society of Mechanical Engineers, Jul. 2012, pp. 327–336.
- [130] L. Gomez, O. Shoham, Z. Schmidt, R. Chokshi, and T. Northug, “Unified Mechanistic Model for Steady-State Two-Phase Flow: Horizontal to Vertical Upward Flow”, *“SPE Journal”*, vol. 5, no. 03, Sep. 2000.
- [131] T. Hibiki and M. Ishii, “One-dimensional drift–flux model for two-phase flow in a large diameter pipe”, *“International Journal of Heat and Mass Transfer”*, vol. 46, no. 10, May 2003.
- [132] S. M. Bhagwat and A. J. Ghajar, “A flow pattern independent drift flux model based void fraction correlation for a wide range of gas–liquid two phase flow”, *“International Journal of Multiphase Flow”*, vol. 59, Feb. 2014.
- [133] M. Ould Didi, N. Kattan, and J. Thome, “Prediction of two-phase pressure gradients of refrigerants in horizontal tubes”, *“International Journal of Refrigeration”*, vol. 25, no. 7, Nov. 2002.
- [134] D. Schmid, B. Verlaet, P. Petagna, R. Revellin, and J. Schifmann, “Flow pattern observations and flow pattern map for adiabatic two-phase flow of carbon dioxide in vertical upward and downward direction”, *“Experimental Thermal and Fluid Science”*, vol. 131, Feb. 2022.
- [135] L. C. Ruspini, “Experimental and numerical investigation on two-phase flow instabilities”, Ph.D. dissertation, Norwegian University of Science and Technology (NTNU), Trondheim, Norway, Mar. 2013.

BIBLIOGRAPHY

- [136] A. Nayak, P. Vijayan, V. Jain, D. Saha, and R. Sinha, "Study on the flow-pattern-transition instability in a natural circulation heavy water moderated boiling light water cooled reactor", ["Nuclear Engineering and Design"](#), vol. 225, no. 2-3, Nov. 2003.
- [137] A. Bergant, A. Simpson, and A. Tijsseling, "Water hammer with column separation: A historical review", ["Journal of Fluids and Structures"](#), vol. 22, no. 2, Feb. 2006.
- [138] W. Owens, "Two-Phase Pressure Gradient", "ASME International Developments in Heat Transfer", vol. 2, 1961.
- [139] W. McAdams, W. Woods, and L. Heroman, "Vaporization Inside Horizontal Tubes - II Benzene-Oil Mixtures", "Transactions of ASME", vol. 64, 1942.
- [140] A. Cicchitti, C. Lombardi, M. Silvestri, G. Soldaini, and R. Zavattarelli, "Two-phase cooling experiments: pressure drop, heat transfer and burnout measurements", "Energia Nucleare", vol. 7, 1960.
- [141] W. Davidson, P. Hardie, C. Humphreys, A. Markson, A. Mumford, and T. Ravese, "Studies of Heat Transmission Through Boiler Tubing at Pressures From 500 to 3300 Pounds", "Transactions of ASME", vol. 65, 1943.
- [142] F. Garcia, R. Garcia, J. Padrino, C. Mata, J. Trallero, and D. Joseph, "Power law and composite power law friction factor correlations for laminar and turbulent gas-liquid flow in horizontal pipelines", ["International Journal of Multiphase Flow"](#), vol. 29, no. 10, Oct. 2003.
- [143] M. Awad and Y. Muzychka, "Effective property models for homogeneous two-phase flows", ["Experimental Thermal and Fluid Science"](#), vol. 33, no. 1, Oct. 2008.
- [144] S. G. Bankoff, "A Variable Density Single-Fluid Model for Two-Phase Flow With Particular Reference to Steam-Water Flow", ["Journal of Heat Transfer"](#), vol. 82, no. 4, Nov. 1960.
- [145] J. M. Chawla, Wärmeübergang und Druckabfall in waagerechten Rohren bei der Strömung von verdampfenden Kältemitteln, ser. VDI-Forschungsheft 523. Düsseldorf: VDI-Verlag, 1967.
- [146] A. Cioncolini, J. R. Thome, and C. Lombardi, "Unified macro-to-microscale method to predict two-phase frictional pressure drops of annular flows", ["International Journal of Multiphase Flow"](#), vol. 35, no. 12, Dec. 2009.
- [147] B. A. Shannak, "Frictional pressure drop of gas liquid two-phase flow in pipes", ["Nuclear Engineering and Design"](#), vol. 238, no. 12, Dec. 2008.
- [148] C. Lombardi and C. Carsana, "Dimensionless pressure drop correlation for two-phase mixtures flowing upflow in vertical ducts covering wide parameter ranges", "Heat and Technology", vol. 10, no. 1-2, 1992.
- [149] D. A. Yashar, M. J. Wilson, H. R. Kopke, D. M. Graham, J. C. Chato, and T. A. Newell, "An Investigation of Refrigerant Void Fraction in Horizontal, Microfin Tubes", ["HVAC&R Research"](#), vol. 7, no. 1, Jan. 2001.

-
- [150] N. Zuber, F. Staub, G. Bijwaard, and P. Kroeger, "Steady State and Transient Void Fraction in Two-Phase Flow Systems", U.S. Atomic Energy Commission, Schenectady, N.Y., Tech. Rep. GEAP-5417, 1967.
- [151] R. H. Bonnecaze, W. Erskine, and E. J. Greskovich, "Holdup and pressure drop for two-phase slug flow in inclined pipelines", *"AIChE Journal"*, vol. 17, no. 5, Sep. 1971.
- [152] D. Beattie and S. Sugawara, "Steam-water void fraction for vertical upflow in a 73.9 mm pipe", *"International Journal of Multiphase Flow"*, vol. 12, no. 4, Jul. 1986.
- [153] D. Bestion, "The physical closure laws in the CATHARE code", *"Nuclear Engineering and Design"*, vol. 124, no. 3, Dec. 1990.
- [154] T. Hibiki and M. Ishii, "Distribution parameter and drift velocity of drift-flux model in bubbly flow", *"International Journal of Heat and Mass Transfer"*, vol. 45, no. 4, Feb. 2002.
- [155] J. C. Chen, "Correlation for Boiling Heat Transfer to Saturated Fluids in Convective Flow", *"Industrial & Engineering Chemistry Process Design and Development"*, vol. 5, no. 3, Jul. 1966.
- [156] M. Shah, "Chart correlation for saturated boiling heat transfer: Equations and further study", *ASHRAE Transactions*, vol. 88, Jan. 1982.
- [157] —, "A new correlation for heat transfer during boiling flow through pipes", *ASHRAE Transactions*, vol. 82, Jan. 1976.
- [158] K. Gungor and R. Winterton, "A general correlation for flow boiling in tubes and annuli", *"International Journal of Heat and Mass Transfer"*, vol. 29, no. 3, Mar. 1986.
- [159] Z. Liu and R. Winterton, "A general correlation for saturated and subcooled flow boiling in tubes and annuli, based on a nucleate pool boiling equation", *"International Journal of Heat and Mass Transfer"*, vol. 34, no. 11, Nov. 1991.
- [160] K. Gungor and R. Winterton, "Simplified general correlation for saturated flow boiling and comparisons of correlations with data", *"Chemical Engineering Research and Design"*, vol. 65, 1987.
- [161] S. G. Kandlikar, "A General Correlation for Saturated Two-Phase Flow Boiling Heat Transfer Inside Horizontal and Vertical Tubes", *"Journal of Heat Transfer"*, vol. 112, no. 1, Feb. 1990.
- [162] D. Steiner and J. Taborek, "Flow Boiling Heat Transfer in Vertical Tubes Correlated by an Asymptotic Model", *"Heat Transfer Engineering"*, vol. 13, no. 2, Jan. 1992.
- [163] H. J. Hoegaard Knudsen and P. H. Jensen, "Heat transfer coefficient for boiling carbon dioxide", *Workshop Proceedings - CO₂ Technologies in Refrigeration, Heat Pumps and Air Conditioning Systems*, Trondheim, Norway, 1997, pp. 319–328.
- [164] R. Yun, Y. Kim, M. Soo Kim, and Y. Choi, "Boiling heat transfer and dryout phenomenon of CO₂ in a horizontal smooth tube", *"International Journal of Heat and Mass Transfer"*, vol. 46, no. 13, Jun. 2003.

BIBLIOGRAPHY

- [165] S. Koyama, S. Lee, D. Ito, K. Kuwahara, and H. Ogawa, "Experimental study on flow boiling of pure CO₂ and CO₂-oil mixtures inside horizontal smooth and micro-fin copper tubes", *Proceedings of 6th IIR-Gustav Lorentzen Conference*, Glasgow, UK, 2004.
- [166] J. R. Thome and J. El Hajal, "Flow boiling heat transfer to carbon dioxide: general prediction method", *"International Journal of Refrigeration"*, vol. 27, no. 3, May 2004.
- [167] L. Cheng, G. Ribatski, and J. R. Thome, "New prediction methods for CO₂ evaporation inside tubes: Part II—An updated general flow boiling heat transfer model based on flow patterns", *"International Journal of Heat and Mass Transfer"*, vol. 51, no. 1-2, Jan. 2008.
- [168] R. Mastrullo, A. Mauro, A. Rosato, and G. Vanoli, "Carbon dioxide local heat transfer coefficients during flow boiling in a horizontal circular smooth tube", *"International Journal of Heat and Mass Transfer"*, vol. 52, no. 19-20, Sep. 2009.
- [169] —, "Carbon dioxide heat transfer coefficients and pressure drops during flow boiling: Assessment of predictive methods", *"International Journal of Refrigeration"*, vol. 33, no. 6, Sep. 2010.
- [170] R. Mastrullo, A. Mauro, and L. Viscito, "Flow boiling of carbon dioxide: Heat transfer for smooth and enhanced geometries and effect of oil. state of the art review", *"International Journal of Refrigeration"*, vol. 108, Dec. 2019.
- [171] D. Hellenschmidt and P. Petagna, "Effects of saturation temperature on the boiling properties of carbon dioxide in small diameter pipes at low vapour quality: Heat transfer coefficient", *"International Journal of Heat and Mass Transfer"*, vol. 172, Jun. 2021.
- [172] A. D. Keni and J. Taillon, *Cryogenic Material Properties Calculator*, (NIST), 2018.
- [173] R. Charnay, R. Revellin, and J. Bonjour, "Flow boiling heat transfer in minichannels at high saturation temperatures: Part I – Experimental investigation and analysis of the heat transfer mechanisms", *"International Journal of Heat and Mass Transfer"*, vol. 87, Aug. 2015.
- [174] M. Ducoulombier, S. Colasson, J. Bonjour, and P. Haberschill, "Carbon dioxide flow boiling in a single microchannel – Part II: Heat transfer", *"Experimental Thermal and Fluid Science"*, vol. 35, no. 4, May 2011.
- [175] C. Y. Park and P. S. Hrňjak, "Flow Boiling Heat Transfer of CO₂ at Low Temperatures in a Horizontal Smooth Tube", *"Journal of Heat Transfer"*, vol. 127, no. 12, Dec. 2005.
- [176] H.-K. Oh and C.-H. Son, "Flow boiling heat transfer and pressure drop characteristics of CO₂ in horizontal tube of 4.57-mm inner diameter", *"Applied Thermal Engineering"*, vol. 31, no. 2-3, Feb. 2011.
- [177] S. Saisorn, P. Wongpromma, and S. Wongwises, "The difference in flow pattern, heat transfer and pressure drop characteristics of mini-channel flow boiling in horizontal and vertical orientations", *"International Journal of Multiphase Flow"*, vol. 101, Apr. 2018.

-
- [178] D. Jung, M. McLinden, R. Radermacher, and D. Didion, "A study of flow boiling heat transfer with refrigerant mixtures", ["International Journal of Heat and Mass Transfer"](#), vol. 32, no. 9, Sep. 1989.
- [179] J. Wattelet, J. Chato, A. L. Souza, and B. Christoffersen, "Evaporative Characteristics of R-134a, MP-39, and R-12 at Low Mass Fluxes", University of Illinois, Urbana, IL, USA, Tech. Rep. ACRCTR-35, 1993, p. 30.
- [180] R. Yun, Y. Kim, and M. Soo Kim, "Flow boiling heat transfer of carbon dioxide in horizontal mini tubes", ["International Journal of Heat and Fluid Flow"](#), vol. 26, no. 5, Oct. 2005.
- [181] A. Pamitran, K.-I. Choi, J.-T. Oh, and Nasruddin, "Evaporation heat transfer coefficient in single circular small tubes for flow natural refrigerants of C3H8, NH3, and CO2", ["International Journal of Multiphase Flow"](#), vol. 37, no. 7, Sep. 2011.
- [182] M. M. Shah, "Unified correlation for heat transfer during boiling in plain mini/micro and conventional channels", ["International Journal of Refrigeration"](#), vol. 74, Feb. 2017.
- [183] M. Cooper, "Heat Flow Rates in Saturated Nucleate Pool Boiling-A Wide-Ranging Examination Using Reduced Properties", *Advances in Heat Transfer*, vol. 16, Elsevier, 1984, pp. 157–239.
- [184] "DIN 1319 - Basic concepts in metrology", Deutsches Institut für Normung e.V. (DIN), Tech. Rep., 1995.
- [185] N. Weichert and M. Wülker, *Messtechnik und Messdatenerfassung*. Oldenbourg Verlag, 2010.
- [186] J. Erven and D. Schwägerl, *Mathematik für Ingenieure*, 2., überarbeitete und erweiterte Auflage, ser. Oldenbourg-Lehrbücher für Ingenieure. München Wien: Oldenbourg, 2002.
- [187] J. R. Taylor, *An introduction to error analysis: the study of uncertainties in physical measurements*, 2nd ed. Sausalito, Calif: University Science Books, 1997.

David SCHMID

Curriculum Vitae

Im Innerdorf 10
79588 Istein
Germany
✉ david.schmid@cern.ch

Personal Information

Date of birth 31/10/1985
Nationality German

Education

- 07/2017-03/2022 **PhD**, *École Polytechnique Fédérale de Lausanne (EPFL)*, Programme Doctoral en Energie, Lausanne, Switzerland
Thesis director: Prof. Jürg SCHIFFMANN, EPFL
Thesis co-director: Prof. Rémi REVELLIN, INSA Lyon
Investigating flow boiling of carbon dioxide at different channel orientations for the thermal management of future detector technologies at the High-Luminosity Large Hadron Collider.
Defense successfully passed on 28/01/2022
- 10/2013-03/2016 **M.Sc.**, *University of Applied Sciences*, Mechanical Engineering, Offenburg, Germany
Thesis supervisor: Prof. Thomas SEIFERT
Engineering of Complex Mechanical Structures for the ATLAS Muon Detector System at the Large Hadron Collider.
- 10/2006-09/2009 **B.Eng.**, *Baden-Wuerttemberg Cooperative State University*, Lörrach, Germany
Studies on general Mechanical Engineering
- 06/2005 **Abitur (A-levels degree)**, *Technisches Gymnasium*, Müllheim, Germany

Work Experience

- 07/2017 - 03/2022 **CERN: Doctoral Student**, *EP-DT-FS*, Geneva, Switzerland
- Conceptualization, engineering, construction, calibration and commissioning of a test facility for investigating the two-phase flow behaviour of CO₂.
 - Operation of refrigeration plants and data collection with test rigs.
 - High-speed imaging of two-phase flows and contributions to image processing techniques.
 - Compilation of a unique database of >3500 measurements of CO₂ two-phase flow.
 - Data analysis and numerical modelling of two-phase flows.
 - Contribution to the development of cooling concepts and two-phase transfer lines.
- 05/2016 - 06/2017 **CERN: Design Engineer**, *ATLAS & Carleton University*, Geneva, Switzerland & Ottawa, Canada
- In charge of the conceptualization and engineering of large assembly and integration tools.
 - Development and successful qualification of vacuum lifting tools for the production of the sTGC detectors.
 - Development and validation of detector support structures and integration equipment for the manipulation of sTGC detectors.

04/2015 - **CERN: Technical Student**, *ATLAS*, Geneva, Switzerland
04/2016

- Development and successful design verification of the sTGC kinematic mounting system for the ATLAS NSW.

10/2009 - **Development Engineer, Project Management Assistant**, *A.Raymond GmbH & Co.KG*,
09/2013 Lörrach, Germany

- Project coordination and engineering in automotive industry.
- Product development with CAD.
- Coordinate and monitor progress of development projects.
- Continuous documentation of the project status and supervision of quality control.
- Coordinate production of bending and punching tools, as well as prototypes and batch production.

10/2006 - **Cooperative Professional Education**, *A.Raymond GmbH & Co.KG*, Lörrach, Germany

09/2009 Cooperative education in parallel to theoretical studies. Work experiences, trainings and apprenticeships:

- Tool design and construction.
- Manufacturing of injection moulds and bending tools in workshops.
- Commissioning of injection moulds and bending tools.
- Series production.
- Quality management.
- Product development.

Languages / Further Information

German Native
English Proficient
French Beginner